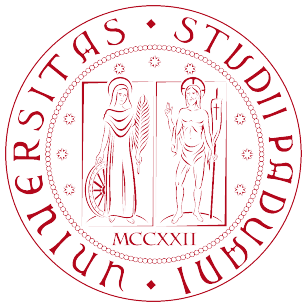

UNIVERSITÀ
DEGLI STUDI
DI PADOVA

UNIVERSITÀ DEGLI STUDI DI PADOVA
Dipartimento di Fisica e Astronomia

CORSO DI DOTTORATO DI RICERCA IN FISICA
XXIX CICLO

Generation of droplets in non-Newtonian liquids with a microfluidic T-junction

Coordinatore: Ch.mo Prof. GIANGUIDO DALL'AGATA
Supervisore: Ch.mo Prof. GIAMPAOLO MISTURA
Co-supervisore: Prof. MATTEO PIERNO

Dottorando: ENRICO CHIARELLO

Abstract

Droplet-based microfluidics is a blossoming research field that presents great potential for many applications, including high-throughput chemical and biological analysis, synthesis of advanced materials, sample pretreatment, protein crystallization, and encapsulation of cells. In most biomedical applications, non-Newtonian fluids are frequently involved. The complete understanding of the role of their rheology on droplets breakup is still far from being achieved, which is crucial for the realization of robust devices which have to be operated with those fluids.

The present work reports a comprehensive and systematic study of the droplet breakup in a microfluidic T-junction, involving Newtonian droplets formed in either Newtonian, purely shear-thinning or purely elastic (Boger) fluids. As shear-thinning fluids, dilute and semidilute solutions of Xanthan, a stiff rod-like polysaccharide, are investigated. At the concentrations considered, they exhibit a well pronounced shear thinning behaviour with finite thinning exponents, while weak elastic effects emerge only at relatively high concentrations. The role of elasticity is instead investigated using solutions of polyacrylamide (PAA). In order to isolate the elasticity from the shear-thinning behaviour, a Boger fluid is employed, which is characterized by a constant viscosity due to a particular choice of the solvent.

From preliminary experiments with PAA results that, while the shape of droplets formed in the Boger fluid is considerably altered with respect to the one in the corresponding Newtonian, there is no strong evidence for the elasticity to affect the droplets size resulting after breakup. Instead, by quantitatively comparing Newtonian and shear-thinning data, robust experimental evidence is provided that the droplet size rescales nicely with an effective Capillary number ($\overline{\mathrm{Ca}}$), which reduces to the usual Capillary number (Ca) when both liquids are Newtonian. Systematic experiments with Xanthan are complemented with numerical simulations of purely thinning fluids based on the lattice Boltzmann models (LBM), which are in good quantitative agreement with the experimental data and confirm the proposed scaling.

Contents

Introduction

The field of microfluidics[1] has blossomed in the last two decades since effective microfabrication techniques, adapted from those used in microelectronics, became readily available[2, 3]. Microfluidics involves the precise manipulation of fluids in extremely small volumes, of the order of nano or pico-liter. At these scales, the high surface-to-volume ratio implies that interfacial phenomena, such as wetting and capillarity, have usually a dominant role. Microfluidics can be divided broadly in two categories, *open microfluidics* and *closed microfluidics*. In the former, the liquids are deposited on a microstructured surface which is exposed to air, as in Fig. 1a, while in the latter the fluids are enclosed in microchannels, as in Fig. 1b.

More specifically, in the field of (closed) droplet microfluidics, the liquids are further confined into droplets, surrounded by another immiscible liquid, as shown in Fig. 2. The fluid forming the droplets is called *dispersed phase*, while the fluid which carries them is called *continuous phase*. Confining the fluids in droplets resolves many problems which are inherent to single-phase microfluidics. In particular, different droplets can act as independent microreactors in which the reagents can rapidly mix, as in Fig. 2, without cross-contamination, as the dispersed phase does not get into contact with the channels walls.

Droplets and bubbles are generated in a variety of microfluidic geometries designed to bring two immiscible fluid streams into contact with one another. The most common geometries can be broadly categorized into three types: *coflow* geometries in which im-

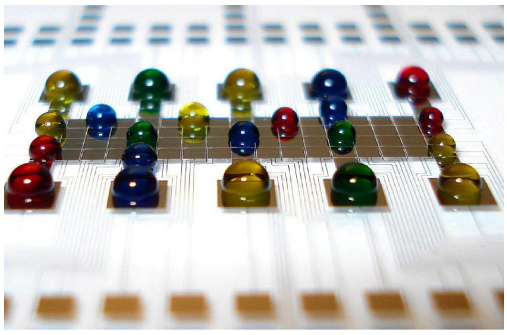

(a)

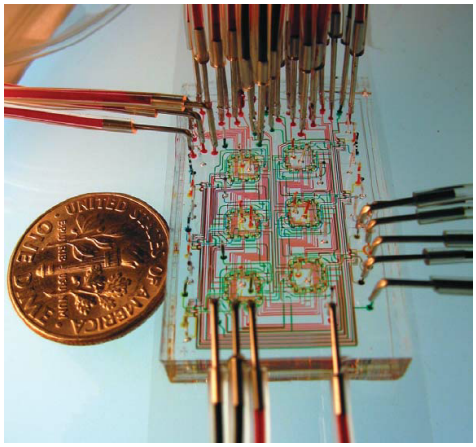

(b)

Figure 1: (a) A picture of an open droplet microfluidic platform controlling more than 20 reaction microvessels (droplets) with no microvalves or other moving parts. Source: [4]. (b) Example of microfluidic chip with six parallel microchemostat reactors, used to study the growth of microbial populations. The coin is 18 mm in diameter. Source: [5]

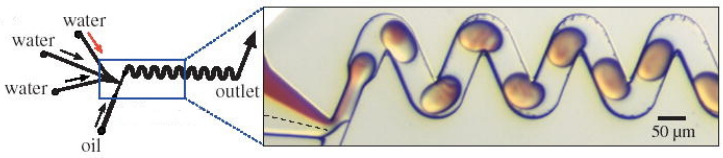

Figure 2: Example of closed droplet microfluidic device. Three aqueous solution (reagents) are simultaneoulsy injected into a stream of oil forming droplets (microreactors), where they can rapidly mix. Source: [6]

miscible fluids meet in parallel streams; *cross-flow* geometries, in which the immiscible fluid streams meet at an angle to one another; and *flow-focusing* geometries in which there is a geometric element that causes the streams to accelerate, narrowing the inner fluid thread. While co-flow and flow-focusing geometries are usually the choice when high-throughput droplet production is required, simpler devices like the T-junction (Fig. 3), which is an example of cross-flow geometry, are still widely used due to their simplicity of fabrication and ease of use, having only two inlets and one outlet.

The materials employed to fabricate these devices affect considerably the range of possible applications. In particular, the wetting properties determine whether the dispersed phase is going to be oil or water. The most widespread materials used in microfabrication are naturally hydrophobic (i.e. water-repellant) thus favoring, without any surface treatment, an oil continuous phase and a water dispersed phase. The opposite situation can occur if hydrophilic materials are employed, like glass. However, microfabrication of glass devices is complex and expensive, requiring dedicated facitities. A viable alternative is to use plastics. Many plastics are weakly hydrophilic, thus allowing the production of oil droplets in water, once suitable surfactants (which affect the wettability) are added to the continuous phase.

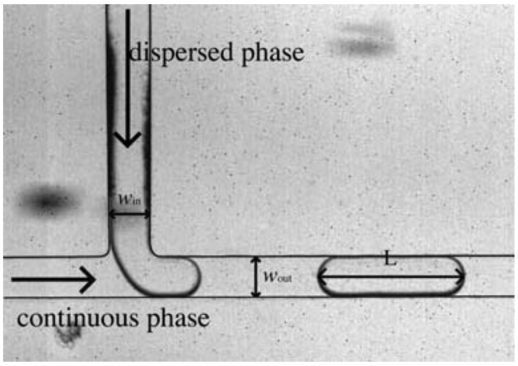

Figure 3: Example of droplet production in a T-junction. The dispersed phase and the continuous phase meet at 90 degrees in a T-shaped junction. Source: [7]

The breakup dynamics of a fluid stream injected into a second, immiscible liquid and the consequent formation of droplets are relatively well understood in the case of two immiscible Newtonian fluids, such as water and oil. More specifically, beside the precise geometry, an important parameter determining the size of the resulting droplets is the *capillary number* Ca, which expresses the balance between viscous stresses and interfacial tension.

Recently, this investigation has been extended to non-Newtonian liquids because of their importance in real applications. Indeed, practically all fluids of interest for biological application (e.g. blood, sinovial fluids) are non-Newtonian, exhibiting flow

dependent viscosity and elastic effects.

Until now, most of the research has focused on the formation of non-Newtonian droplets carried by Newtonian continuous phases. Only a few studies considered the opposite case of droplets carried by a non-Newtonian continuous phase, mostly involving the flow-focusing geometry. An exhaustive description of the breakup mechanism driven by non-Newtonian continuous phases in T-junctions is still effectively lacking.

This thesis reports a comprehensive and systematic study of the droplet breakup in a microfluidic T-junction, involving Newtonian droplets formed in either Newtonian, shear-thinning (i.e. flow-depentent viscosity) or Boger (i.e. purely elastic) fluids. As shear-thinning fluids, dilute and semidilute solutions of Xanthan, a stiff rod-like polysaccharide, are investigated. At the concentrations considered, they exhibit a well pronounced shear-thinning behaviour, i.e. the viscosity decreases with increasing shear rate. Weak elastic effects emerge only at relatively high concentrations. The role of elasticity is instead investigated using solutions of polyacrylamide (PAA), a polymer which has a long and flexible structure. In order to isolate the elasticity from the shear-thinning behaviour, a Boger fluid is employed, which is characterized by a constant viscosity due to a particular choice of the solvent.

By quantitatively comparing Newtonian and shear-thinning data, robust experimental evidence is provided that the droplet size rescales nicely with an effective Capillary number $(\overline{\mathrm{Ca}})$, which reduces to the usual Capillary number (Ca) when both liquids are Newtonian. Systematic experiments with Xanthan are complemented with numerical simulations of purely thinning fluids based on the Lattice-Boltzmann method (LBM), which are in good qualitative and quantitative agreement with the experimental data and confirm the proposed scaling. Preliminary experiments with PAA show that, while the shape of droplets formed in the Boger fluid is considerably altered with respect to the one in the corresponding Newtonian, there is no strong evidence for the elasticity to affect the droplets size resulting after breakup.

This thesis is organized as follows: in Chapter 1 the main concepts of the physics underlying droplet microfluidics are introduced. In Chapter 2 the droplet generators and the breakup mechanisms are covered. In Chapter 3 the experimental methodologies are presented, including the microfabrication techniques which allow the realization of the microfluidic T-junction. In Chapter 4 one of such fabrication techniques, involving low-cost and readily available materials and equipments, is demonstrated to be a valuable alternative to other standard, but more demanding, microfabrication techniques. Chapter 5 contains the main results of the present work, exploring the production of droplets in non-Newtonian fluids, involving both elastic and shear-thinnig properties. In particular, the effective capillary number used to rescale the shear-thinning data is introduced and its validity is tested, complemented by Lattice-Boltzmann numerical simulations. Finally, there are the conclusions and an appendix, which reports an introduction to the Lattice-Boltzmann Method, i.e the numerical scheme adopted for the simulations which complement the experimental results.

Chapter 1

Basic concepts in fluid dynamics

In this chapter the main concepts of the fluid dynamics underlying droplet microfluidics will be briefly introduced. Section 1.1 covers the dynamics of both Newtonian and non-Newtonian fluids. Section 1.5 introduces the concept of interfacial tension.

1.1 Fluid mechanics

In the approximation of continuum mechanics[1], a fluid is described by classical fields, e.g. continuous functions of space and time, which specify its properties in every point. The fluid element in the volume dV in the position $\boldsymbol{x}$ at time t is described by a mass density $\rho(\boldsymbol{x}, t)$ and a velocity field $\boldsymbol{u}(\boldsymbol{x}, t)$. The conservation of mass is given by the *continuity equation*:

$$\partial_t \rho + \nabla \cdot (\rho \boldsymbol{u}) = 0 \tag{1.1}$$

which states that the mass in the (fixed) volume dV, can change in time only via a mass current $\rho \boldsymbol{u}$ through the surface enclosing dV. This equation can be rewritten as:

$$\frac{D\rho}{Dt} + \rho(\nabla \cdot \boldsymbol{u}) = 0 \tag{1.2}$$

where the *material derivative* $DA/Dt = \partial_t A + \boldsymbol{u} \cdot \nabla A$ expresses the time variation of some quantity A in the reference frame of a fluid element which is moving along the flow $\boldsymbol{u}$. For an incompressible fluid, the density of a fluid element must remain constant during time evolution, i.e. $D\rho/Dt = 0$, therefore the contraint of incompressibility is equivalent to:

$$\nabla \cdot \boldsymbol{u} = 0 \tag{1.3}$$

i.e. the flow velocity is solenoidal. The general equation for the conservation of momentum is the analogous of Newton's second law, called *Cauchy equation*:

$$\rho \frac{D\boldsymbol{u}}{Dt} = \nabla \cdot \mathbf{T} + \boldsymbol{F}_{ext} \tag{1.4}$$

where $\mathbf{T}$ is the total stress tensor and $\boldsymbol{F}_{ext}$ is an external bulk force density (e.g. gravity). This equation, together with the continuity equation 1.1, states that the variation of momentum in a volume element dV, enclosed by the surface S, in the time dt, is due to the momentum transported (advected) by the flow through S, the momentum $\boldsymbol{F}_{ext} dt$ due to a bulk force, and the momentum variation due to the stress $\mathbf{T}$ on S. The quantity

[1] that is the lenghtscale of the variation of the properties of the fluids are large compared to the granularity of the material

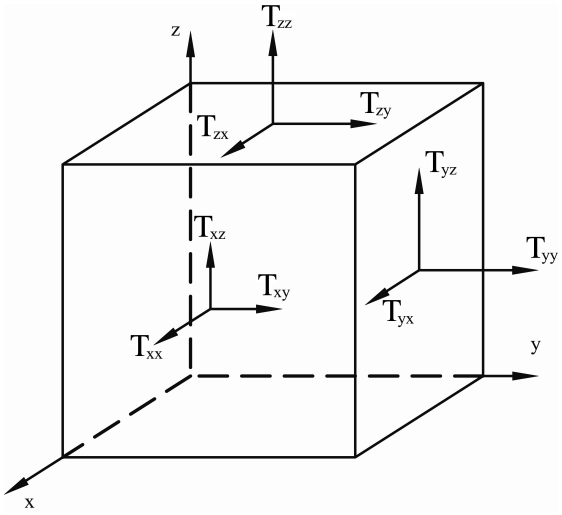

Figure 1.1: Components of the stress tensor

$\mathbf{T}_{xy}$ represents the $\hat{\boldsymbol{y}}$ component of the force (per unit area) exerted on a surface normal to the $\hat{\boldsymbol{x}}$ direction, as in Fig. 1.1. Thus off-diagonal elements of $\mathbf{T}$ like $\mathbf{T}_{xy}$ are shear stresses, while the diagonal elements like $\mathbf{T}_{xx}$ are normal stresses. In the case of an incompressible fluid, the isotropic part of the normal stresses of $\mathbf{T}$ does not constribute to the deformation of the fluid element, and is usually explicited out. The total stress is then written as $\mathbf{T} = -p\mathbf{I} + \boldsymbol{\tau}$, where p is the *pressure*, $\mathbf{I}$ is the identity matrix and $\boldsymbol{\tau}$ is called *deviatoric* or *viscous* stress tensor. The tensor $\boldsymbol{\tau}$ is symmetric[2] and traceless[3], thus only three shear stresses $\boldsymbol{\tau}_{xy}$, $\boldsymbol{\tau}_{xz}$, $\boldsymbol{\tau}_{yz}$ and two normal stress differences $N_1 = \boldsymbol{\tau}_{xx} - \boldsymbol{\tau}_{yy}$ and $N_2 = \boldsymbol{\tau}_{yy} - \boldsymbol{\tau}_{zz}$ must be specified. The quantities N_1 and N_2 are called, respectively, *first normal stress difference* and *second normal stress difference*. A small deformation of a fluid element can be described by the *strain rate tensor*:

$$\dot{\boldsymbol{\epsilon}} = \nabla \boldsymbol{u} + (\nabla \boldsymbol{u})^{\mathrm{T}}$$

whose elements $\dot{\boldsymbol{\epsilon}}_{ij} = (\partial_i u_j + \partial_j u_i)$ are linear in the components of the gradient of the velocity field u. In the limit of small deformations, the viscous stress tensor can then be expressed as a function of the strain rate tensor $\boldsymbol{\tau}(\dot{\boldsymbol{\epsilon}})$. The particular stress-strain rate relation $\boldsymbol{\tau}(\dot{\boldsymbol{\epsilon}})$ is called *costitutive law*, and it is what specifies the properties of a fluid. Once a particular form of the constitutive law is assumed then, at least in principle, the eq. 1.4 can be solved.

1.2 Newtonian fluids

Many common fluids, e.g. water, gases and most liquids composed of small molecules, are accurately described by a linear relationship:

$$\boldsymbol{\tau} = \eta \dot{\boldsymbol{\epsilon}} \tag{1.5}$$

All these fluids are called *Newtonian fluids* and the constant of proportionality η is called *viscosity*. In the case of a simple shear flow, as in Fig. 1.9c, this reduces to:

$$\tau = \eta \frac{du_x}{dy} = \eta \dot{\gamma} \tag{1.6}$$

[2] due to conservation of angular momentum.

[3] because the trace is included in the pressure p.

where the quantity $\dot{\gamma} = du_x/dy$ is called *shear rate*. The relation in eq. 1.6, instead of the more general in eq. 1.5, is commonly used as the definition of a *Newtonian fluid*.

Inserting the stress $\boldsymbol{\tau}$ from eq. 1.5 in the Cauchy momentum equation 1.4, with the additional assumptions of incompressibility $\nabla \cdot \boldsymbol{u} = 0$ and of constant viscosity η (which in general may depend on the local temperature), then the *incompressible Navier-Stokes equation* is obtained:

$$\rho \partial_t \boldsymbol{u} + \rho(\boldsymbol{u} \cdot \nabla)\boldsymbol{u} = -\nabla p + \boldsymbol{F_{ext}} + \eta \nabla^2 \boldsymbol{u} \tag{1.7}$$

with the constraint $\nabla \cdot \boldsymbol{u} = 0$. Boundary conditions have to specified for the pressure p and the velocity $\boldsymbol{u}$. In particular, in the case of a solid (impermeable) wall, if the fluid is viscous ($\eta > 0$) the *no-slip* boundary condition is imposed, i.e. the $\boldsymbol{u} = 0$ at the wall.

The non-linear term $(\boldsymbol{u} \cdot \nabla)\boldsymbol{u}$ is commonly called *inertial* term, while $\eta \nabla^2 \boldsymbol{u}$ is called *viscous term*. The non-linear term makes the equation difficult to solve and can lead to very complex dynamics, however, in practice, in the context of microfluidics it can usually be neglected. If L denotes the typical lenghtscale and U the typical velocity, by dimensional analysis the ratio between the inertial term and the viscous term can be written as:

$$Re = \frac{\rho U L}{\eta} \tag{1.8}$$

called *Reynolds* number. In microfluidics in most cases $Re << 1$, thus the dynamics is dominated by viscous dissipation and the flow is laminar.

1.3 Non-Newtonian fluids

While there are many materials that can be adequately described as Newtonian fluids, most real-world fluids exhibit at least some deviation from eq. 1.5, and they are thus generally called non-Newtonian fluids.

In order to exhibit non-Newtonian behaviour, the flow must be able to alter the local microstructure of the fluid, and that is why simple fluids composed of small molecules are Newtonian at the velocity gradients available in nature or in the laboratory. This, however, is not true for most complex fluids like solutions of colloidal particles, long flexible polymers, wormlike micelles, and polymer melts. If λ denotes the stress relaxation time of the fluid element, then $Wi = \lambda \dot{\gamma}$, called *Weissenberg number*, is the ratio between the stress relaxation time and the timescale of the flow. For instance, λ may be the time it takes to a polymer chain to return to its equilibrium configuration after being stretched by the stress exerted by the flow. Typical value of λ for a dilute polymer solution are in the range $10^{-3} - 10^{0} s$.

The number Wi determines whether the flow is able to depart the fluid microstructure from its equilibrium configuration. If the velocity gradients are small enough, then $Wi << 1$ and even a complex fluid will behave as Newtonian. In order to trigger non-Newtonian effects, Wi must be in the order of unity or larger.

There are many kinds of non-Newtonian fluids, and different ways to categorize them based on their behaviour. The rest of this section will focus on the so-called generalized Newtonian fluids, which comprise both shear-thinning and shear-thickening, and viscoelastic fluids.

1.3.1 Generalized Newtonian fluids

In *time-independent fluids*, the stress in some point is a function only of the strain rate in that point $\boldsymbol{\tau} = \boldsymbol{\tau}(\dot{\boldsymbol{\epsilon}})$, and thus such fluids have no memory of their past history. More

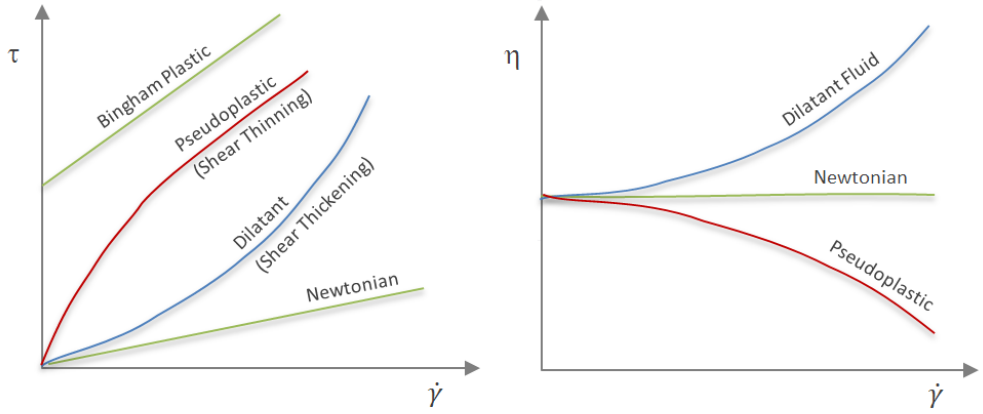

Figure 1.2: Dependence of the shear stress τ and of the viscosity η on the shear rate $\dot{\gamma}$ for different kinds of generalized Netonian fluids.

specifically, in a *generalized Newtonian fluid*, the flow can instantaneously affect only the local viscosity, but not the structure of the stress tensor:

$$\boldsymbol{\tau} = \eta(\dot{\gamma})\dot{\boldsymbol{\epsilon}} \tag{1.9}$$

This is the simplest generalization of eq. 1.5. The flow-dependent viscosity η is a function only of shear rate $\dot{\gamma} = \sqrt{\dot{\boldsymbol{\epsilon}}_{ij}\dot{\boldsymbol{\epsilon}}_{ij}/2}$, which is an invariant quantity. It is common for the viscosity to increase or decrease monotonically with the shear rate.

If the viscosity η increases with the shear rate $\dot{\gamma}$, then the fluid is called *shear-thickening*, or dilatant, fluid. An example is a suspension of cornstarch in water.

On the contrary, if η decreases with increasing $\dot{\gamma}$, then the fluid is called *shear-thinning*, or pseudoplastic. Shear-thinning fluids are quite common. Examples are ketchup, paint, nail polish, whipped cream, many polymer solutions and polymer melts.

Another kind of behaviour is that of *Bingham* plastics. At low shear stress, they exhibit a solid-like behaviour and, in order for them to flow, the stress must exceed some threshold value above which they can behave either as Newtonian or shear-thinning fluids. An example is toothpaste. Fig. 1.2 summarizes the behaviours of the various time-independent fluids described so far.

1.3.2 Power-law fluids

An important class of fluids is that of the so-called *power-law fluids* which exhibit, at least in some range of shear-rate, a power law dependence on the shear-rate:

$$\begin{aligned} \tau &= k\dot{\gamma}^n \\ \eta &= k\dot{\gamma}^{n-1} \end{aligned} \tag{1.10}$$

The exponent n is called *flow behaviour index* and k is called *flow consistency index*. For a shear-thinning fluid $n < 1$, while $n = 1$ corresponds to a Newtonian behaviour. Shear-thickening fluids are described with $n > 1$, although these fluids are less common.

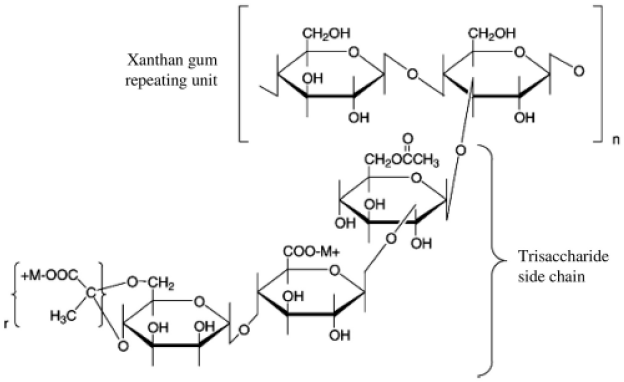

Figure 1.3: Molecular structure of xanthan gum. Source: [8]

Xanthan gum

An example of shear-thinning fluid, which will be used in the experiments of this thesis as the prototypical power-law fluid, is an acqueous solution of *xanthan gum*. Xanthan gum is a semi-rigid rod-like polysaccharide (Fig. 1.3) secreted by the bacterium Xanthomonas campestris. It is vastly used in the industry as a rheology modifier. For instance, it is used in the food industry as a thickening agent and stabilizer, and for the drilling fluids in the oil industry. Indeed, even an amount of xanthan as small as 1% can increase the viscosity of a solution by orders of magnitude. Although the molecule of xanthan is quite stiff, elastic effects are reported in concentrated solutions[8], which are due to network interactions. However, in dilute and semidilute solutions the dominant behaviour is that of shear-thinning. Fig. 1.4 reports the viscosity dependence on the shear-rate, for solutions of xanthan in water[4] at different concentrations. The viscosity has a power-law behaviour for a large range of shear rates, whereas at very low and at very high shear rates a Newtonian behaviour is recovered, with viscosities η_o and η_∞ respectively. In particular, the value of η_∞ is slightly above the solvent viscosity. Both the magnitude of the slope and η_o increase with concentration. A phenomenological model which capture this behaviour is given by the *Carreau-Yasuda model*:

$$\eta(\dot{\gamma}) = \eta_\infty + (\eta_0 - \eta_\infty)\,(1 + (\lambda\dot{\gamma})^a)^{\frac{n-1}{a}} \tag{1.11}$$

where η_o and η_∞ are the low shear-rate and high shear-rate limit viscosities, respectively, λ is a relaxation time, and a is a parameter affecting the shape of the curve. For high shear-rates $\dot{\gamma}$ this model is practically equivalent (neglecting η_∞) to that of eq. 1.10. The behaviour of xanthan solutions depends not only on the polymer concentration, but also on the polymer molecular weight M_W, as shown in Fig. 1.5. At small M_W the non-Newtonian behaviour is practically absent, while the shear-thinning becomes important at molecular weights of the order of $M_W \sim 10^6 g/mol$.

1.3.3 Viscoelastic fluids

Viscoelastic fluids exhibit, with shearing, some partial elastic recovery, behaving halfway between an elastic Hookean solid and a purely viscous fluid. In a purely elastic situation the stress τ is a function of the strain ϵ (i.e. the displacement):

$$\tau = G\epsilon$$

[4] to which salt is added in order to stabilize the suspension

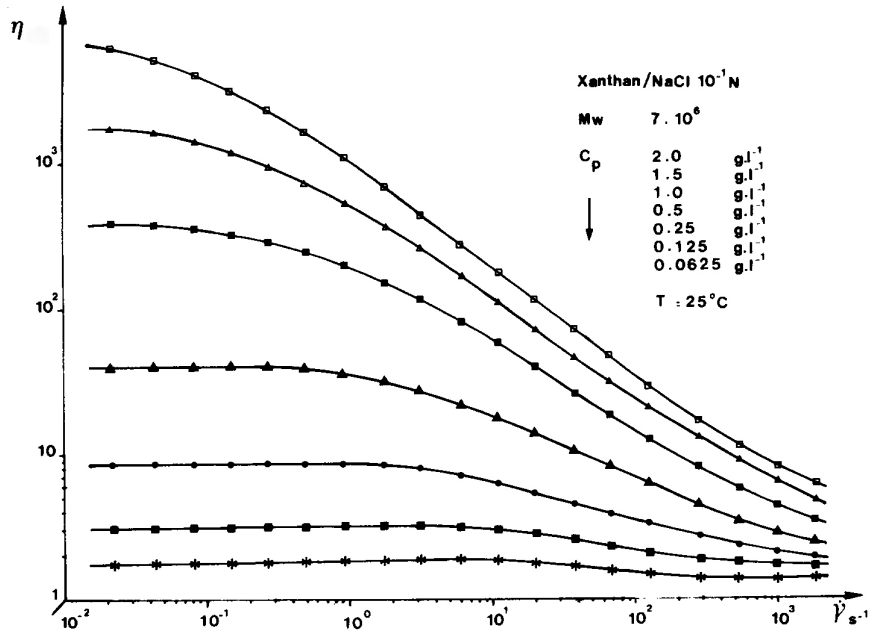

Figure 1.4: Viscosity-shear rate curves for Xanthan solutions at different concentrations c_p. Source: [9]

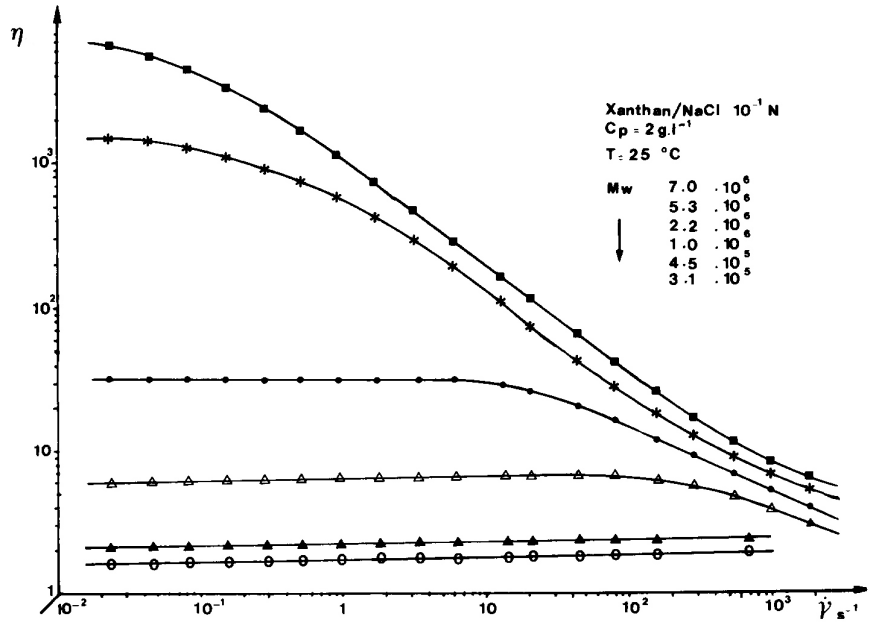

Figure 1.5: Viscosity-shear rate curves for Xanthan solutions at different molecular weights M_W. Source: [9]

while in a purely viscous fluid τ is a function of the strain rate $\dot{\epsilon}$:

$$\tau = \eta\dot{\epsilon}$$

A viscoelastic behaviour would thus be described by a mixture of the two. The simplest model is the *Maxwell fluid*, which is equivalent to a spring connected in series with a dashpot. Its constitutive law has the form:

$$\tau + \frac{G}{\eta}\dot{\tau} = \eta\dot{\epsilon}$$

This fluid behaves like a solid at short times scales with respect to the relaxation time $\lambda = \eta/G$, while it behaves as a viscous fluid at longer time scales. This simple model however does not predict normal stress differences.

The minimal constitutive law which can adequately describe normal stress differences is that of a *second-order fluid*:

$$\tau = \eta\dot{\boldsymbol{\epsilon}} - \frac{\Psi_1}{2}\overset{\nabla}{\dot{\boldsymbol{\epsilon}}} + \Psi_2\dot{\boldsymbol{\epsilon}}\dot{\boldsymbol{\epsilon}} \tag{1.12}$$

where the quatities Ψ_1 and Ψ_2 are parameters that depend on the material. This equation contains non-linear terms up to the second order. Analogously to the material derivative, here the symbol $\overset{\nabla}{A}$ represents the *upper convected time derivative*, i.e. the time derivative of some quantity A with respect to a reference frame which is moving, rotating and stretching along with the flow[5]. In the case of a simple shear flow, this constitutive law predicts normal stress differences N_1 and N_2 which are quadratic in the shear rate $\dot{\gamma}$:

$$\begin{aligned} N_1 &= \Psi_1\dot{\gamma}^2 \\ N_2 &= \Psi_2\dot{\gamma}^2 \end{aligned} \tag{1.13}$$

The quantities Ψ_1 and Ψ_2 are parameters of the material, called *viscometric functions*, and generally approach a constant value in the limit of small $\dot{\gamma}$.

The existence of such normal stress differences in a shear flow implies that curved streamlines exert a force in the (radial) direction normal to the flow. This gives raise to phenomena like the Weissenberg effect, as shown in Fig. 1.6, in which a viscoelastic fluid raises a vertical spinning rod because the centrifugal force is overcome by the normal stress difference of the fluid.

Boger fluids

The fluid modeled by eq. 1.12 has a constant viscosity η. Although most viscoelastic polymer solutions also exhibit shear-thinning (for which a third-order approximation would be required), it is suitable to model the so-called *Boger fluids*, which are defined as viscoelastic fluids with a constant viscosity. While a real Boger fluid does not exist, good approximations can be obtained with polymer solution with a particular choice of the solvent. Examples of Boger fluids are polyisobutylene solutions in polybutene, and polyacrylamide in a viscous solvent like wheat syrup or glycerine. Molecules of these polymers, like polyacrylamide (Fig. 1.7), are long flexible chains that tend to occupy the available space in such a way as to have maximum entropy, to which correspond the largest number of possible microscopic configurations. When they are streched, the

[5]the upper convecter time derivative of a tensor $\mathbf{A}$ is defined as $\overset{\nabla}{\mathbf{A}} = D\mathbf{A}/Dt - (\nabla\boldsymbol{u})^T\mathbf{A} - \mathbf{A}(\nabla\boldsymbol{u})$.

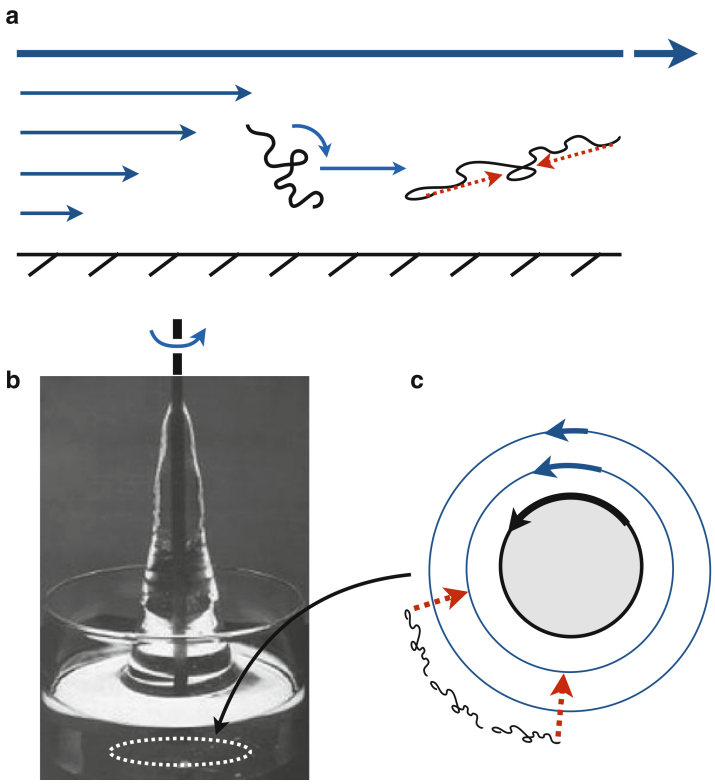

Figure 1.6: (a) An illustration of the mechanism of normal stress differences in viscoelastic fluids. A shear flow rotates and stretches polymers along streamlines creating anisotropic elastic stresses. (b) The Weissenberg effect (rod climbing): a rotating rod inside of a viscoelastic fluid excites an upward climb of fluid, unlike in a Newtonian flow. (c) The Weissenberg effect is explained by normal stress differences which develop along curved streamlines, leading to "strangulation" and an upward ascent. Source: [10]

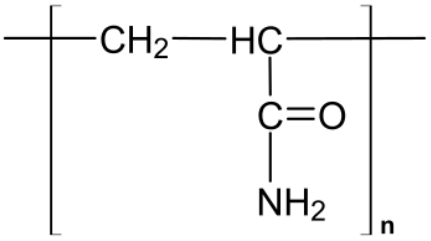

Figure 1.7: Molecular structure of polyacrylamide.

number of available configurations is reduced, and thus there is effectively an entropic restoring force which acts as a spring. Table 1.1 reports examples of Boger fluids compositions, made of solutions of polyacrylamide in different solvents. Fig. 1.8 reports viscosity and first normal stress difference data for these Boger fluids. Indeed, the viscosity is practically constant and the first normal stress difference is well described by 1.13.

1.4 Flows in microfluidics

In Fig. 1.9 are depicted some examples of confined flows, which are of particular interest for droplet microfludics.

	Polymer		Viscous solvent		Water	Salt (NaCl)
Label	Type	Wt%	Type	Wt%	Wt%	Wt%
A	PAA AP30	0.015	Glycerol	82	15.24	2.73
B	PAA AP30	0.015	Glycerol	90	8.31	1.66
C	PAA AP30	0.015	Wheat syrup	85	14.97	—
D	PAA AP30	0.025	Wheat syrup	88	11.96	—
E	PAA AP30	0.0396	Wheat syrup	93	6.94	—

Table 1.1: Composition of various polyacrylamide (PAA AP30) Boger fluids, in different solvents. Source: [11]

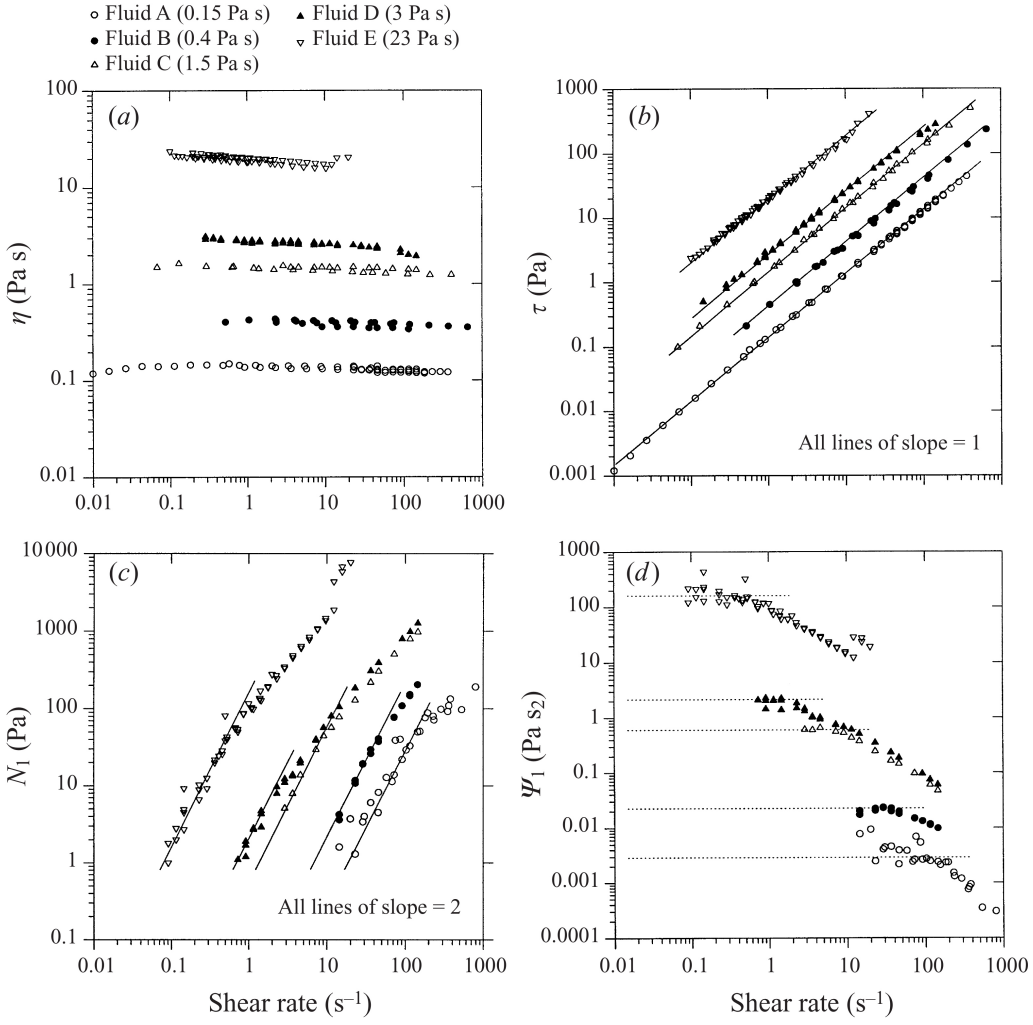

Figure 1.8: Steady shear properties for the polyacrylamide Boger fluids reported in Table 1.1, indicating the dependence on the shear rate of the viscosity and first normal stress coefficient. Source: [11]

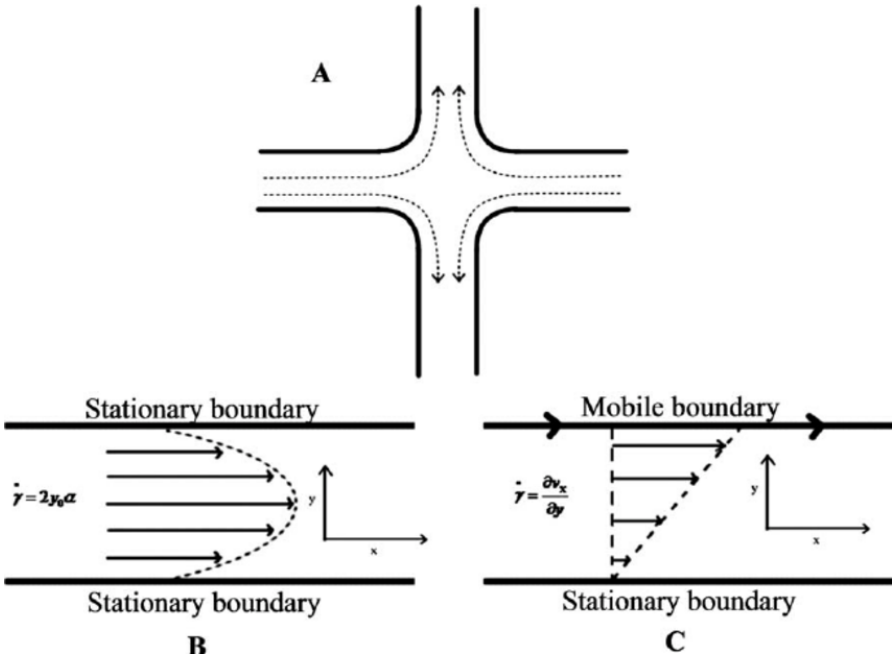

Figure 1.9: Examples of flows in microfludics. (a) extensional flow in a cross-junction; (b) Poiseuille flow; (c) simple shear flow, or Couette flow. Source: [12]

The central region of a cross-junction, as in Fig. 1.9a, is a particular case of *elongational* flow (sometimes called extensional flow). In this flow, due to incompressibility, the strain rate in one direction (e.g. the vertical one) is compensated by an opposite strain rate in the other (lateral) direction. In other words, the fluid is elongated, or stretched, in one direction and compressed in the other. The normal stresses in this situation are not isotropic and, even in the case of a Newtonian fluid, the normal stress differences N_1 and N_2 are generally non zero.

Fig. 1.9b shows the *Poiseuille flow*, which is confined between two fixed parallel walls. The flow is obtained by applying a constant pressure difference Δp between the two lateral sides of the channel. The velocity profile is parabolic, and the average velocity is proportional to the applied pressure difference. The shear rate is maximum at the walls and zero at the center.

Fig. 1.9c reports the case of a *simple shear* flow. This flow, called also *Couette flow*, is confined between two parallel walls with a distance L, one moving with a constant velocity U withe respect to the other. Thus the shear rate is constant and equal to $\dot{\gamma} = U/L$ In this kind of flow the diagonal components of the strain rate $\boldsymbol{\epsilon}$ are zero. Therefore, the corresponding components of $\boldsymbol{\tau}$ are also zero in Newtonian fluids, and thus in a simple shear flow they do not exhibit normal stress differences. This is not true in general for non-Newtonian fluids, which can exhibit finite normal stress differences even in a simple shear flow, as shown in the previous section.

1.5 Interfacial tension

The previous sections dealed with the bulk description of fluids with a homogeneous composition, whose fluid elements interact through local stresses. The particles of a real fluid, or a mixture of real fluids, however exhibit also long range interactions (van der Waals), as well as short range cohesive forces (between like particles) and adhesive

forces (between unlike particles). Macroscopically, this can lead to the formation of an interface, that is a surface separating two phases, e.g. the interface between a liquid and its vapor or the interface between two immiscible fluids.

1.5.1 Interfacial energy

The formation of such an interface can be described with thermodynamics. Considering the case of a mixture of two fluids A and B, the local composition of the system can be described in terms of some quantity ϕ. For example, ϕ may be the fraction of particles (per unit volume) of the A component of the fluid, i.e. $\phi = n_A/N$, where $N = N_A + N_B$ is the total number of particles. The total free energy F of the system in the volume V can then be approximated as the sum of two contributions in the following form[13]:

$$F = \int_V dV\, f_0(\phi) + \kappa(\nabla\phi)^2 + \dots$$

where $f_0(\phi)$ is the free energy per unit volume that there would be if the system was homogeneous in composition, i.e. the energy required to have a composition ϕ, and the other term is a function of the gradient of the local composition, i.e. an energy term due to spatial variations of the composition. Only small variations of the composition are assumed and higher order terms are neglected.

Assuming that there is a flat interface of area A (with coordinate z normal to it) separating the system in two phases of bulk composition ϕ_1 and ϕ_2[6], as in Fig. 1.10, then F can be rewritten as:

$$F = A \int_{-\infty}^{+\infty} dz\, f_0(\phi) + \kappa \left(\frac{d\phi}{dz}\right)^2$$

The *interfacial free energy* per unit area σ is defined as the difference of the total free energy (per unit area) with respect to the one that there would be if the same particles were in one of the two phases:

$$\begin{aligned}\sigma &= \int_{-\infty}^{+\infty} dz\, f_0(\phi) + \kappa \left(\frac{d\phi}{dz}\right)^2 - N\phi\eta_A^{eq} - N(1-\phi)\eta_B^{eq} \\ &= \int_{-\infty}^{+\infty} dz\, \Delta f(\phi) + \kappa \left(\frac{d\phi}{dz}\right)^2\end{aligned}$$

where η_A^{eq} and η_B^{eq} are the equilibrium chemical potentials of the component A and B, respectively, in one of the two phases (which are equal at equilibrium). The term $\Delta f(\phi) = f_0(\phi) - N\phi\eta_A^{eq} - N(1-\phi)\eta_B^{eq}$ can be interpreted as the free energy (or "chemical work") required to transfer the particles in the volume Adz from an infinite reservoir with composition ϕ_1 or ϕ_2 to a composition ϕ, while the other term is again due to the spatial gradient in composition.

The system, in general, is not at equilibrium and σ is not at its minimum value. For example, starting from a situation with an interface diffused over a large distance (or even a uniform composition), the gradient term $\kappa\,(d\phi/dz)^2$ would be very small, at the expense however of a large intergrated value of Δf due to the system being distant from the composition ϕ_1 or ϕ_2. At equilibrium the composition will have a sigmoidal shape as depicted in Fig. 1.10, with the interface being practically localized

[6] that is, in this context, ϕ_1 is the fraction of particles of the A component in one phase, while ϕ_2 is the fraction of particles of the same A component in the other phase.

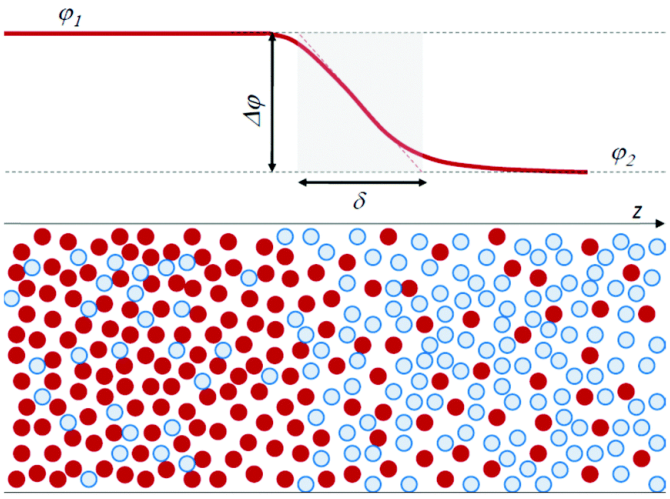

Figure 1.10: Interface forming in a mixture of two fluids, separating two regions of uniform composition ϕ_1 and ϕ_2.

in a region of thickness δ which separates the two phases. The thickness δ increases with the temperature T, and can become infinite at some critical temperature T_c, at which the two phases reach the same composition ϕ_c.

However, for all practical purposes in droplet microfluidics where two immiscible fluids are involved, the interface has a thickness of the order of the molecular size and is usually approximated with a geometrical surface. The effective interfacial energy, or *interfacial tension*, is then defined as the free energy dF required to increase the area of the interface by an amount dA:

$$\sigma = \left[\frac{\partial F}{\partial A}\right]_{T,V,N} \tag{1.14}$$

Since σ is positive, in order to minimize free energy, the system will naturally evolve towards a configuration of minimum surface area A. If two parallel lines of lenght L lying on the surface are considered, the product σL is the work required to pull apart these two lines (in the perpendicular direction) by a small amount dx, thus increasing the area A by an amount Ldx. Interfacial tension can therefore be interpreted as a force per unit lenght required to pull apart two regions of the interface. An interface acts, in some sense, as an elastic membrane and, e.g., a gas bubble or a liquid drop surrounded by another immiscible liquid tend to assume a spherical shape, which has the smallest surface area.

Young-Laplace equation

In order to minimize its area, the interface assumes in general a curved shape, as in the example of the bubble above. At equilibrium, the tangential stresses exerted on the fluid by the interface must obviously be zero since, by definition, a static fluid cannot sustain a tangential stress. A curved interface, however, can still exert normal stresses, which are opposed by the fluid with a pressure discontinuity across the interface. This pressure difference Δp, called *Laplace pressure*, is balanced by surface tension according to the *Young-Laplace equation*:

$$\Delta p = \sigma H = \sigma \left(\frac{1}{R_1} + \frac{1}{R_2}\right) \tag{1.15}$$

where R_1 and R_2 are the *principal radii of curvature* and H is the *total curvature*. In the simple case of a spherical drop, the two radii are equal $R_1 = R_2 = R$ and the equation simplifies to $\Delta p = 2\sigma/R$.

1.6 Two-phase flows

The existence of an interface separating two different fluids A and B introduces new boundary conditions for the Navier-Stokes equation. If $\hat{\boldsymbol{n}}$ denotes the normal to the interface, then the normal component of the velocity $\boldsymbol{u} \cdot \hat{\boldsymbol{n}}$ must be continuous across the interface and equal to the velocity of the interface. The tangential velocity must also be continuous and be the same in the two fluids at the interface. Similary, the tangential stress must be continuous. Assuming, for simplicity, two Newtonian fluids of viscosities η_A and η_B, the surface normal in the $\hat{\boldsymbol{y}}$ direction and the tangential velocity in the $\hat{\boldsymbol{x}}$ direction, then:

$$\eta_A \left(\frac{du_x}{dy}\right)_A = \eta_B \left(\frac{du_x}{dy}\right)_B \tag{1.16}$$

This shows than an important parameter affecting the flow is the *viscosity ratio*:

$$\lambda = \frac{\eta_A}{\eta_B} \tag{1.17}$$

As already mentioned in Sec. 1.2, in microfluidics the inertial effects are usually negligible when compared to viscous stresses, since the Reynolds number $Re << 1$. Similarly, the ratio between the inertia and interfacial tension is given by the *Weber number*

$$\mathrm{We} = \frac{\rho U^2 L}{\sigma} \tag{1.18}$$

The Weber number in microfluidics is also usually small, although in particular cases it can become important, for instance in microfluidic devices operated at very high speed. When this is not the case, since also the effect of gravity is usually negligible, then the forces that dominate the flow are viscous stresses and interfacial tension.

Capillary number

The ratio between the viscous stresses and interfacial tension defines the *capillary number* Ca, and can be found by dimentional analysis. If L is the typical lenght scale, then the force due to viscous stress τ on the surface L^2 is $\eta\dot{\gamma}L^2$, while the force due to interfacial tension is σL. The shear rate $\dot{\gamma}$ is the velocity gradient U/L, where U is the typical velocity. Thus the ratio between the viscous force and the interfacial tension is:

$$\mathrm{Ca} = \frac{\eta U}{\sigma} \tag{1.19}$$

Typical values for Ca in droplet microfluidics are in the range $10^{-4} - 10^{1}$.

Chapter 2

Droplet formation mechanisms

Droplets and bubbles are generated in a variety of microfluidic geometries designed to bring two immiscible fluid streams into contact with one another. The most common geometries can be broadly categorized into three types: *coflow* geometries in which immiscible fluids meet in parallel streams; *cross-flow* geometries, in which the immiscible fluid streams meet at an angle to one another; and *flow-focusing* geometries in which there is a geometric element that causes the streams to accelerate, narrowing the inner fluid thread. These geometries are illustrated in Fig. 2.1.

Droplet formation in a T-junction device was first reported by Thorsen et al.[14], who used pressure controlled flows in microchannels to generate droplets of water in a variety of different oils. A typical example of a T-junction is depicted in Fig. 2.2, which shows the two phases flowing through two orthogonal channels and forming droplets when they meet. The T-junction is widely adopted due to the simplicity of microfabrication and ease of operation, having only two inlets and one outlet. The only geometrical parameters are channel height h, the main channel width w_{out} and the lateral channel width w_{in}, as shown in Fig. 2.2. The effects of varying the geometrical parameters are relatively well understood[15].

The first flow-focusing device was reported by Anna *et al.*[16]. This geometry is more complex, involving more geometrical parameters, as shown in Fig. 2.3. The large number of geometrical aspect ratios characterizing flow-focusing devices has prevented the determination of simple scaling laws to predict the droplet size, distribution and rate of emission as a function of the key parameters. Nevertheless, these devices are widely used, as well as coflow devices, expecially when high throuhput production of monodisperse droplets is required. The frequency of prodution can go over 10kHz and the size of the droplets can go down to $\sim 1\mu m$ [17].

In all these systems, droplet breakup is observed to occur in different regimes, depending on the parameters of the systems. In all geometries, two regimes, called *dripping* and *jetting*, are observed. In these regimes droplet formation is due to a complex interplay between viscous drag, interfacial tension and, in some cases, inertia, which determine the size of the resulting droplets.

In addition, when the size of droplets becomes comparable with the size of the channels, the geometrical confinement becomes important, and in some cases it becomes the dominant effect in determining the droplet size. This results in a third regime of breakup, called *squeezing*, which is not always observed, depending on the particular geometry.

The role of geometrical confinement can be better understood by first considering the opposite, simpler situation of an unconfined coflow. In section 2.1 the dynamics of

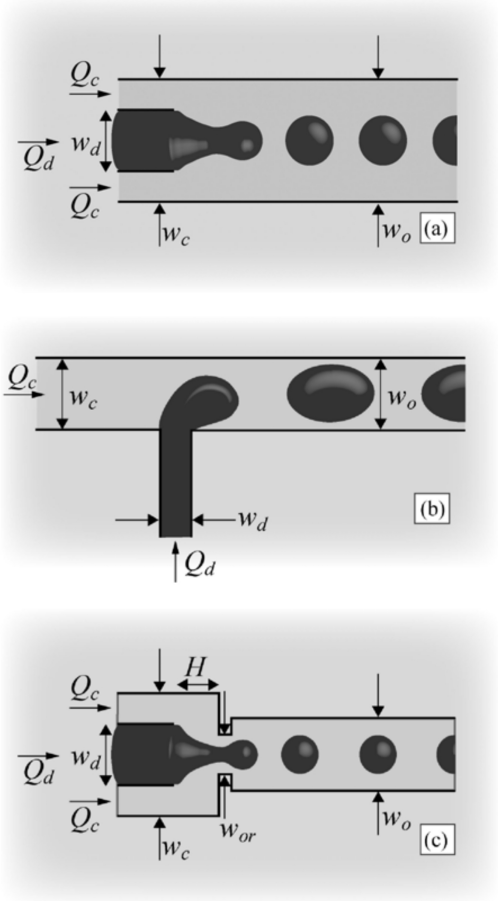

Figure 2.1: Illustrations of the three main microfluidic geometries used for droplet formation. (a) Co-flowing streams, (b) cross- flowing streams in a T-shaped junction, and (c) elongational flow in a flow focusing geometry. In each case the widths of the inlet and outlet streams are indicated. It is assumed that the device is planar with a uniform depth h. Source: [18]

droplet breakup is described in the coflow geometry without confinemet. In this situation the breakup can happen either in dripping or in jetting, and is due to interfacial instabilities. Section 2.2 gives some insight on the role of confinement, and how it can suppress the interfacial instabilities. In this situation, the squeezing regime of breakup can arise, in which the breakup is driven by geometrical confinement and is caused by the pressure build-up due to the channel obstruction. In the same section, given its simplicity, a full derivation of the scaling law of the droplet size in squeezing is given in the case of the T-junction geometry.

2.1 Breakup in unconfined coflow

In this geometry a liquid stream is injected co-axially in another viscous liquid. An implementation of such a system, shown in Fig 2.4a, is realized by inserting a tapered capillary tube, with a tip diameter $d_{tip} = 30\mu m$, inside another tube which has a square cross section with lateral size $D = 1mm$. Since $d_{tip}/D \sim 10^{-2}$, the geometrical confinement on the local flow close to the tip due to the outer tube walls can be negleted. In this system droplet breakup is observed to happen in two distinct regimes, called *dripping* and *jetting*.

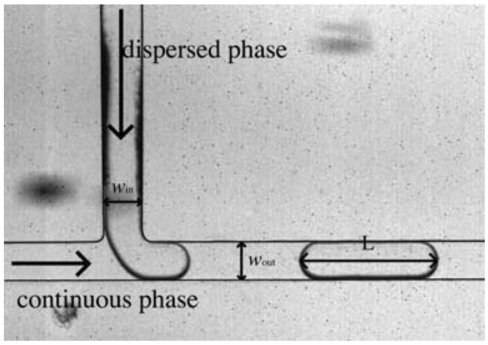

Figure 2.2: Example of droplet production in a T-junction. The dispersed phase and the continuous phase meet at 90 degrees in a T-shaped junction. Source: [7]

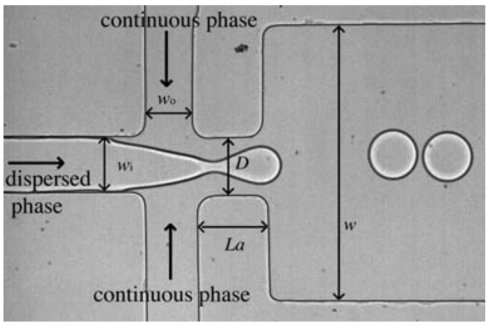

Figure 2.3: Example of droplet production in a flow-focusing device. The dispersed phase is squeezed by two counter-streaming flows of the continuous phase, forcing droplets to detach. Source: [7]

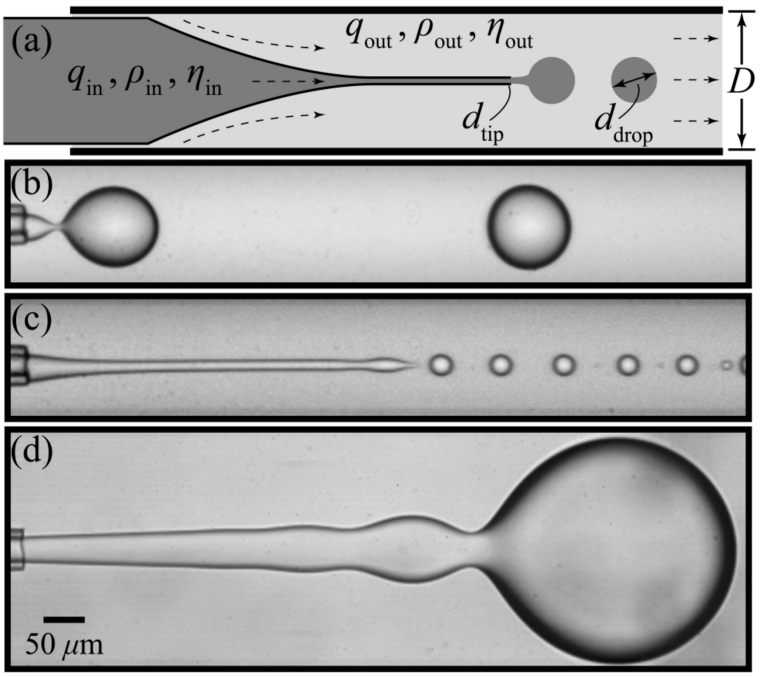

Figure 2.4: Example of droplet production in a co-flowing device. (a) Device geometry showing the tapered inner capillary in the outer square capillary. (b) Image of the dripping regime. (c) Image of a narrowing jet generated by increasing Q_{out} above a threshold while keeping Q_{in} constant, with $\eta_{in}/\eta_{out} = 0.1$. (d) Image of a widening jet generated by increasing Q_{in} above a threshold while keeping Q_{out} constant, with $\eta_{in}/\eta_{out} = 0.1$. Scale bar applies to (b)-(d), the walls are not shown. Source: [19]

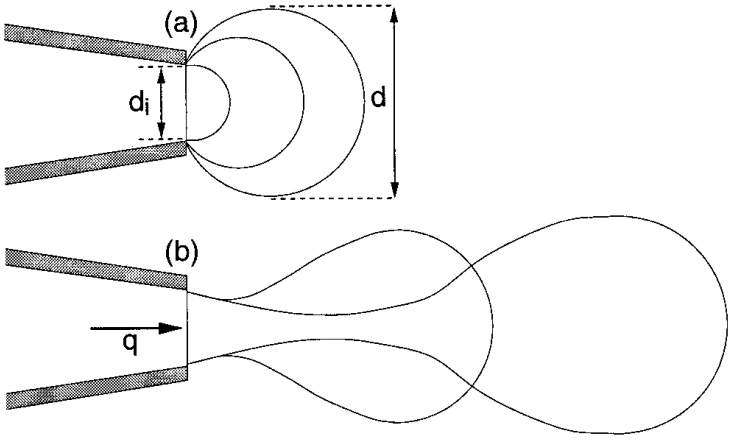

Figure 2.5: Droplet formation in the dripping regime: (a) growth; (b) necking and separation. Source: [20]

2.1.1 Dripping

At small flow rates of both the inner and the outer fluid, the droplets are emitted periodically close to the tip, as shown in Fig. 2.4b. In this dripping regime, the growing droplet experiences two competing forces: viscous drag pulling it downstream and forces due to interfacial tension holding it to the tip. Initially, interfacial tension dominates and the droplet has a spherical shape. As the droplet grows, the drag forces eventually become comparable with the interfacial tension, and the droplet is pulled downstream leaving behind a neck, as shown in Fig. 2.5. The neck then rapidly collapses due to interfacial instability, i.e. a perturbation of the interface that leads to a decrease in interfacial area is amplified by interfacial tension. Such instability grows faster than it is advected by the flow, and leads to a self-sustained, well-tuned oscillation, that has a fixed position in space and is called *absolute instability* The diameter of the resulting droplet is found to decrease with the capillary number Ca_{out} of the outer fluid as $d_{drop} \sim \mathrm{Ca}_{out}^{-1}$ [20]

2.1.2 Jetting

When the capillary number Ca_{out} is increased above a value of the order of unity, the absolute instability is suppressed since it does not have time to grow, and a steady, narrowing jet is formed as shown in Fig. 2.4c. The jet then breaks into droplets further downstream due to the Rayleigh-Plateau instability: a perturbation, due to noise in the system, can be decomposed in different wavelenghts, and the fastest growing component has a wavelenght which is proportional to the cylinder diameter; the cylinder then decomposes into spherical droplets whose diameter is roughly twice the one of the original cylinder.

As shown in Fig. 2.6, the diameter of the jet, and consequently that of the droplets, is found to scale with the flow rate ratio as $d_{jet} \sim (Q_{in}/Q_{out})^{1/2}$. This instability is different from the absolute instability as it does not have a specific position in space and is independent on the geometry of the tip. The position of breakup depends on how far the perturbation can travel during the growth time, therefore this kind of instability is called *convective instability*.

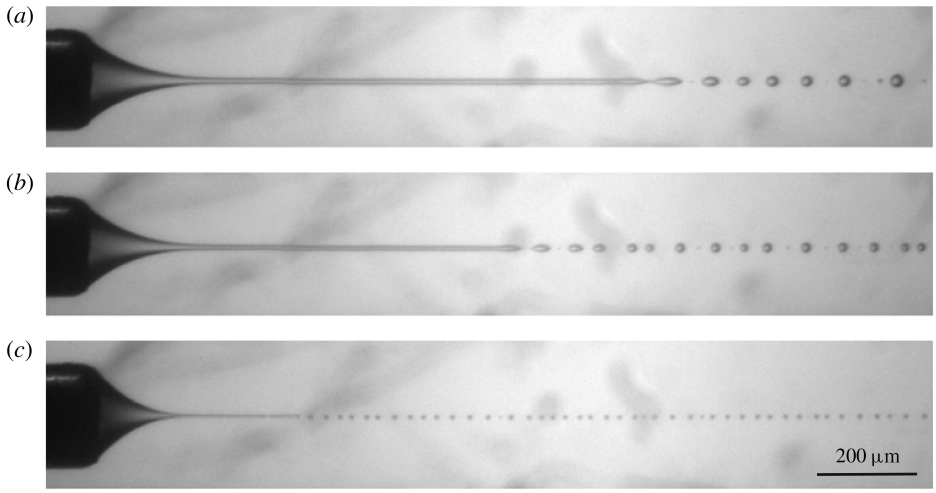

Figure 2.6: Example of droplet production in a co-flowing device in the jetting regime, at varying the flow rate ratio $\varphi = Q_{in}/Q_{out}$. The viscosity ratio and the capillary number of the outer phase are fixed and are, respectively, $\lambda = \eta_{in}/\eta_{out} = 10^{-2}$ and $\mathrm{Ca}_{out} = 5$. (a) $\varphi = 10^{-2}$; (b) $\varphi = 6 \cdot 10^{-3}$; (c) $\varphi = 5 \cdot 10^{-4}$ Source: [21]

2.1.3 Dripping to jetting transition

The transition from dripping to jetting by increasing the capillary value Ca_{out} can be interpreted as a transition from an absolute to a convective instability[22], and is found to happen at a critical value of Ca_{out} which is a function of the viscosity ratio between the two phases[23].

In the coflowing system, another kind of transition from dripping to jetting is observed when the velocity u_{in} of the inner phase is increased, while keeping fixed Ca_{out}. At small u_{in}, the Weber number $\mathrm{We} = \rho_{in} d_{tip} u_{in}^2/\sigma$ is very small, and inertia is neglible with respect to interfacial tension. However, when $\mathrm{We} \sim 1$ a widening jet is observed, as shown in Fig. 2.4d. The reason that it widens is that the inner flow velocity is higher that the velocity of the outer fluid, thus because of viscous drag it is slowed down in the axial direction. Again, the formation of droplets due to an absolute instability is observed[22], until Ca_{out} is increased above ~ 1, where a stable jet is obtained which later breaks down into droplets due to the Rayleigh-Plateau convective instability. A phase diagram of dripping and jetting at varying Ca_{out} and We is shown in Fig. 2.7.

2.2 Breakup in confined geometry

The situation can be dramatically different when the flows are confined along one dimension, like between two parallel walls, or along two dimensions, like in a microchannel. Fig. 2.8a shows an example of planar geometry in which the channels have a rectangular cross-section, all with the same height h. This situation is typical in microfluidics, and is a result of most of the microfabrication techniques. The particular case in Fig. 2.8 is a coflow in which, similarly to the one described in the previous section, the dispersed phase exiting the nozzle, with flow rate Q_i, meets in parallel with the continuous phase that comes from two lateral channels, with flow rate Q_o. The outlet channel has a lateral size W which is large compared to the height h, thus the confinement is mainly due to the height h.

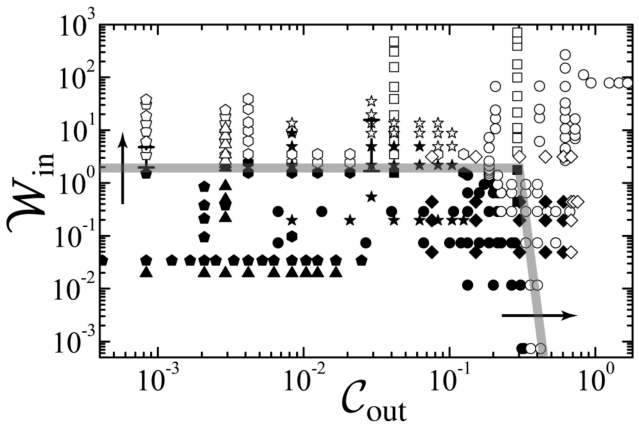

Figure 2.7: State diagram of the dripping-to-jetting transition in a coflowing stream as a function of the capillary number continuous (outer) phase Ca_{out} and the Weber number of the dispersed (inner) phase W_{in}. Filled symbols represent dripping while open symbols represent jetting. Each symbol shape is a different viscosity ratio, interfacial tension, or geometry. Source: [19]

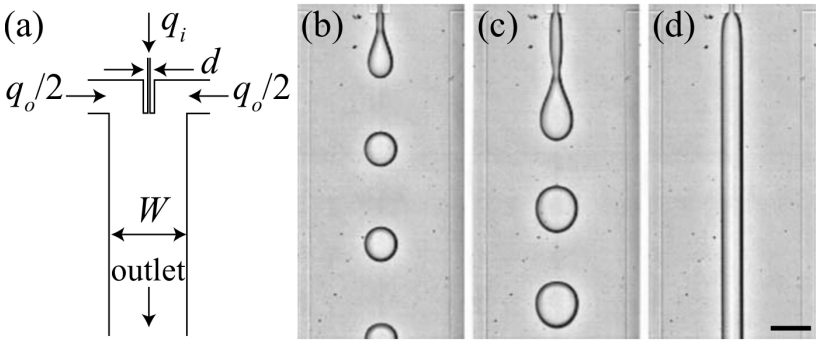

Figure 2.8: (a) Schematic of a coflowing device with confinement. The devices have an outlet channel of width $W = 700\mu m$ and a height $h = 34\mu m$. The inner fluid enters through a nozzle of width $d = 20\mu m$. The scale bar is $200\mu m$. The inner and outer fluids have flow rates Q_i and Q_o, respectively. (b) Drop formation in a dripping regime, (c) drop formation in a jetting regime, and (d) jetting without breaking. Source: [24]

The droplet breakup is observed in dripping (Fig. 2.8b), close to the nozzle, or in jetting, i.e. after the formation of a jet which then breaks downstream into droplets due to the Rayleigh-Plateau instability (Fig. 2.8c). However, when the lateral size of the jet, which grows with the ratio Q_i/Q_o, becomes comparable with or greater than the height h of the channel, the jet becomes stable and no droplet is formed, as shown in Fig. 2.8d. Due to confinement, the jet doesn't have a cylindrical shape anymore and, in this situation, any perturbation of the interface results in a increase of its surface area. The interfacial instability is thus suppressed by the confinement.

2.2.1 Squeezing regime

When the flows of the dispersed and continuous phases are further confined, by both being forced through a microchannel, like in Fig. 2.2, a third regime of breakup may arise. In this regime, called *squeezing*, the otherwise stable stream of the dispersed phase is broken down into segments, not by shear stresses like in dripping, but by the build-up of the upstream pressure due to the increased resistance to flow of the

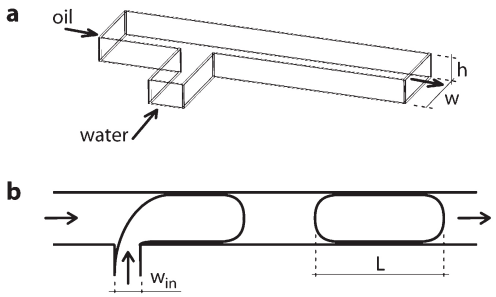

Figure 2.9: (a) A schematic illustration of the microfluidic T-junction composed of rectangular channels. The channels are planar and have uniform height h. (b) A top view of the same schematic in a two-dimensional representation. Flow along the main channel proceeds from left to right. Oil is used as the continuous phase, which is injected in the main channel, of width w. Water, which is used as the dispersed phase, is injected in the orthogonal inlet. The dispersed phase inlet has a width w_{in} which is smalled than the main channel width w, in particular $1 < w/w_{in} < 4$. The length L of the droplet is the distance between the furthest downstream and upstream points along the interface of a fully detached immiscible plug. Source: [25]

continuous phase, which results from the obstruction of the channel caused by the dispersed phase.

This regime is observed both in cross-flow, e.g. T-junctions and cross-junction, and in flow-focusing geometries when they are operated at very low capillary numbers Ca $< 10^{-2}$ and only if the confinemet is important enough for the dispersed phase to obstruct the main channel.

2.2.2 T-junction

The squeezing mechanism of breakup was first proposed by Garstecki *et al.*[25] considering the T-junction geometry, as shown in Fig. 2.9. The T-junction is made by two microchannel joining at a right angle. The main channel has a width w, the lateral one has a width w_{in}, and both have the same height h. In their experiment, Garstecki *et al.* used oil as continuous phase, injected with a flow rate Q_{oil} in the main channel, while water is used as dispersed phase, injected in the lateral channel with flow rate Q_{water}.

When the lateral channel width w_{in} is very small compared to the main channel, e.g. $w_{in} \lesssim 1/4$, then the dispersed phase stream is distorted due to the viscous stress exerted by continuous phase, and breakup happens before the emerging dispersed phase can reach the opposing channel wall. This situation is analogous to that in Fig. 2.8, and breakup happens either in dripping, at small Ca, or in jetting, at higher Ca.

When w_{in} is comparable with the main channel width w, e.g. $1/2 \lesssim w_{in}/w \lesssim 1$, then the dispersed phase entering the main channel can completely obstruct the it before breaking up, as depicted in Fig. 2.9b. Actually, the continuous phase can still flow around the dispersed phase, either by the thin lubricating film or leaking through the four corners (*gutter flow*), as shown in Fig. 2.10.

The breakup dynamics was originally thought to be driven by the shear stress[14] on the interface exerted by the continuous phase in the gap between the interface and the wall. However, experiments with continuous phases of different viscosity μ, reported in Fig. 2.11, show that the size L of the droplets is practically independend on the viscosity, but is determined mainly on the flow rate ratio Q_{water}/Q_{oil}, being $L \sim w$ for $Q_{water}/Q_{oil} \lesssim 1$ and $L \sim Q_{water}/Q_{oil}$ for greater ratios. This, in addition to the

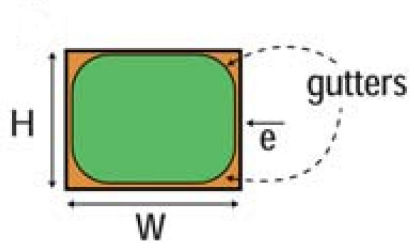

Figure 2.10: Cross section view of a large moving droplet (green) in a rectangular capillary filled with the continuous phase (orange), featuring thin lubrication films, with thickness e, and corners gutters. Source: [7]

fact that the capillary numbers in these experiment are very small, being in the range $10^{-5}-10^{-3}$, suggests that viscous stress is not the driving force in the squeezing regime.

In the mechanisms proposed by Garstecki *et al.*[25], described in Fig. 2.12, the forces which act on the dispersed phase are the interfacial tension, the viscous force exerted by the continuous phase flowing in the gap, and the force due to the increased pressure upstream of the emerging dispersed phase, which results from the continuous phase being forced to flow in a narrow gap.

The surface tension force is associated with the Laplace pressure jump Δp_L across the (quasi-)static interface, $\Delta p_L = \sigma(r_a^{-1}+r_r^{-1})$, where r_a is the radius of axial curvature, in the plane of the device, and r_r is the radius of the radial curvature, in the cross-section of the neck joining the inlet for the dispersed phase with the tip.

In the intermediate stage of the process of formation of a droplet (Fig. 2.12a) the radial curvature is bounded by the height of the channels ($h < w$) and $r_r \sim h/2$ (or less) everywhere. The axial curvature is greater at the downstream tip of the dispersed phase ($r_a^{tip} \sim w/2$) than at the upstream side of it ($r_a^{up} \sim w$). The interface on the downstream side of the thread acts on the liquid inside the thread with a stress $p_L \sim -\sigma(2/w + 2/h)$, oriented upstream. The interface located upstream acts on the dispersed phase with a stress $p_L \sim \sigma(1/w + 2/h)$, oriented downstream. The sum of the two, multiplied by the cross-section wh of the channel gives the estimate of the interfacial tension force $F_c \sim -\sigma h$, which is oriented upstream.

If $u_{gap} = Q_{oil}/h\epsilon$ denotes the velocity of the continuous phase in the gap ϵ, the viscous stress can be estimated as $\tau \sim \mu u_{gap}/\epsilon$. The force exerted on the area of the gap $A_{gap} \sim hw$ by the continuous phase is then $F_\tau = A_{gap}\tau \sim \mu Q_{oil} w/\epsilon^2$.

The pressure drop of a fluid flowing in a rectangular channel of length $\sim w$ and with lateral dimension h and $\epsilon << w$ is given by the Hagen-Poiseuille law as $\Delta P \sim \mu Q_{oil} w/h\epsilon^3$. The resulting force on the surface on the upstream side of the dispersed phase, which has area $\sim hw$, is $F_R \sim \Delta p hw \sim \mu Q_{oil} w^2/\epsilon^3$. If $\epsilon << w$, then it is now evident why the viscous force F_τ is negligible with respect to F_R.

Four stages are identified during droplet breakup, as shown in Fig. 2.12c-e: (I) the dispersed phase enters the main channel, (II) the dispersed phase obstructs the channel, (III) the droplet grows and the neck thins until (IV) detachment.

The length L of the droplet can then be found by estimating the volume V_{fill} of fluid that is injected in the droplet during the growth stage (III), in addition to the initial volume V_0 at the stage (II).

When the dispersed phase has obstructed the main channel (II), the neck has a characteristic size d, as shown in Fig. 2.12a. The pressure upstream increases due to the increased resistance to flow and the continuous phase starts to "squeeze" the upstream

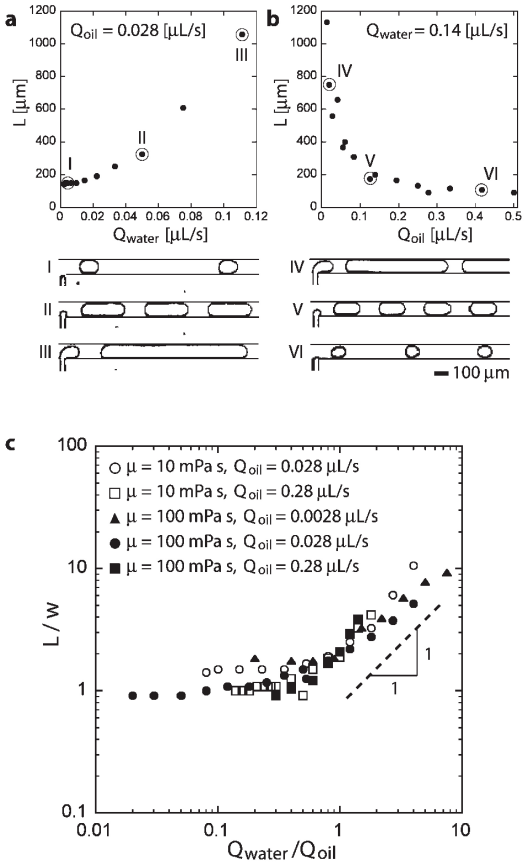

Figure 2.11: Dependence of the length L of the aqueous droplets produced in the T-junction ($h = 33\mu m$, $w = 100\mu m$, $w_{in} = 50\mu m$), on the flow rates of the dispersed (Q_{water}) and continuous (Q_{oil}) phases. (a) Dependence of L on Q_{water} for constant value of Q_{oil}, (b) dependence of L on Q_{oil} for constant value of Q_{water}. The Roman numerals correspond to the optical micrographs shown below the figures. (c) Dimensionless length of the droplets (L/w) plotted as a function of the ratio of the flow rates of the dispersed and continuous phases. There are five different series of data plotted on this graph, each corresponding to a different combination of the viscosity (μ) of the continuous fluid and its flow rate (Q_{oil}). The legend is given in the figure. There is a hundred-fold difference in the shear stress $\tau \propto \mu Q_{oil}$ between the first (open circle) and last curve (filled square). Source: [25]

side of the interface. The neck size decreases at a rate $u_{squeeze}$ which is of the order of the velocity of the continuous phase, i.e. $u_{squeeze} \sim Q_{oil}/hw$. The neck thins until it reaches the corner of the junction (Fig. 2.12b), at which it rapidly collapse and the droplet detaches. The total time in which the droplet it connected through the neck to the dispersed phase thread is thus $t_{neck} = d/u_{squeeze}$. During the time t_{neck} the droplet is filled by the dispersed phase at a rate Q_{water}, and the injected volume is $V_{fill} = Q_{water}t_{neck}$. The initial volume in the channel is of the order of $\sim w^2h$, which is the cross section multiplied by the initial length ehich is of the order of $\sim w$ (Fig. 2.12a).

The total volume of the droplet is thus $V_{droplet} = V_0 + V_{fill}$ and the length is obtained by dividing this by the cross-section hw, i.e. $L \sim w + (d/u_{squeeze})Q_{water}/hw$. The length of the droplet is thus $L \sim w + d\,Q_{water}/Q_{oil}$. It is common to normalize the length L by the channel width w:

$$\frac{L}{w} = 1 + \alpha\frac{Q_{water}}{Q_{oil}} \tag{2.1}$$

where $\alpha = d/w \sim w_{in}/w$. The scaling in eq. 2.2 shows that in the squeezing regime,

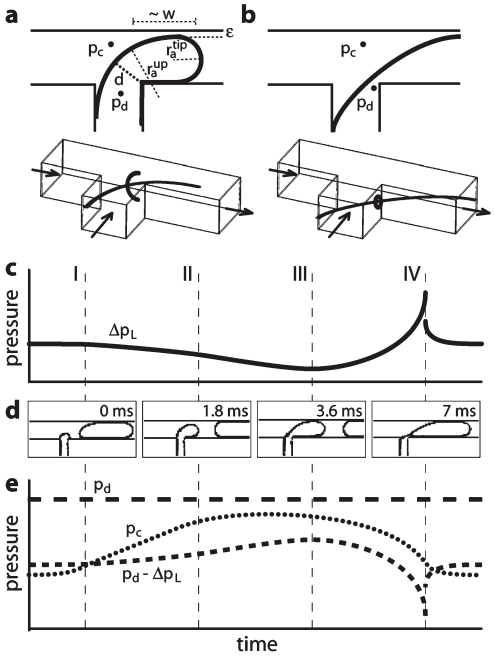

Figure 2.12: (a) A schematic illustration (top view) of the shape of the tip of the immiscible thread at an intermediate stage of break-up. The separation between the interface and the wall of the main channel is denoted as ϵ. The length of the tip is on the order of the width w of the main channel. The radii r_a of axial curvature (in the plane of the device) are $r_a^{tip} \sim w/2$ (at the downstream side of the tip) and $r_a^{up} \sim w$ (at the upstream side). The positions at which are defined the hydrostatic pressures in the dispersed and continuous phases are indicated with p_d and p_c, respectively. At this stage of breakup, the neck has a characteristic size d of the order of $\sim w$. In (b) is depicted the moment right before breakup, when the neck is collapsing. Insets (a) and (b) (bottom view) illustrate the axial and radial curvature. (c) - (e) Four stages of formation of a droplet are idientified: the stream of the dispersed phase enters into the main channel (I), the stream blocks the main channel (II), the droplet elongates and grows downstream (III), the droplet separates from the inlet (IV). (c) Evolution of the Laplace pressure jump across the interface (Δp_L), (d) micrographs of at the respective stages. (e) Schematic illustration of the evolution of the hydrostatic pressure p_d in the dispersed phase at the end of the inlet, pressure p_c in the continuous phase in the junction, and the difference $p_d - \Delta p_L$. Source: [25]

which holds at very small capillary number Ca $\lesssim 10^{-2}$, the droplet size depends only on the flow rate ratio and the geometry of the T-junction. The parameter α has been derived here as a constant of the order of the ratio between the lateral and the main channel widths. It is common express the scaling law of the droplet length as:

$$\frac{L}{w} = \alpha_1 + \alpha_2 \frac{Q_d}{Q_c} \tag{2.2}$$

where Q_d and Q_c are, respectively, the flow rate of the dispersed phase and of the continuous phase, while α_1 and α_2 are fitting parameter which depend on the geometry of the T-junction, which are both of order ~ 1.

Chapter 3

Materials and Methods

This chapter gathers the various experimental methodologies which are used to realize the experiments presented in subsequent chapters.

The T-junction and the overall microfluidic system are described in Sec. 3.1. The pendant drop technique, used to measure the interfacial tension between different liquids, is presented in Sec. 3.2. The microfabrication techniques used to realize the microfluidic devices are presented in Sec. 3.3. Finally, the experimental setup which allows the measurement of the droplets is described in Sec. 3.4.

3.1 Microfluidic system

The microfluidic system used in this work consists of both a microscopic fluidic device, which has inputs and outputs, as well as some external macroscopic actuators which control the fluids injected in the system. The microfluidic device is composed of two microchannels that meet at a right angle, forming the so called *T-junction*, as shown inf Fig.3.1. The two microchannels have the same rectangular cross section, with a lateral width W and a height H. In general, the T-junction is used by injecting two different fluids independently in the two inlets of the microchannels, controlling either the input pressure or the flow-rate by some external device.

In the case of droplet microfluidics, the two injected fluids are immiscible, e.g. water and oil (or a liquid and a gas), and when they meet at the junction droplets of one fluid are formed and carried out by the other fluid. The fluid of which the droplet are made of is called *dispersed phase*, while the outer fluid, which carries them, is called *continuous phase*. The overall resulting fluid exiting the outlet, consisting of both the dispersed and the continuous phases, is called *microemulsion*.

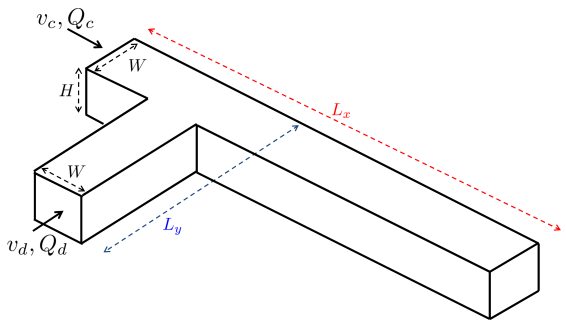

Figure 3.1: Schematic representation of the geometry of the T-junction microfluidic device.

The two inlets of the main and the side microchannels of the T-junction are coupled by Teflon tubing to two glass syringes ($500\mu l$), while the outlet tubing goes to a reservoir at atmospheric pressure. Two identical syringe-pumps (PHD 2000, Harvard Apparatus) are used to actuate the syringes, therefore the flow rate Q_d of the dispersed phase and the flow rate Q_c of the continuous phase at the inlets of the T-junction (Fig.3.1) are forced to be the same as the ones at the outlets of the respective syringes, which are determined by the speed of the syringe-pumps. This is true only if the tubing are rigid, as in the case of Teflon tubing. If they are elastic, as in the case of silicone tubing, the flow rate at one inlet of the T-juntion are not istantaneously equal to the syringe one, but it will become so if the system is given enough time, in order for the tubing to deform and for the fluid to reach a stationary flow. The two syringe pumps are controlled independently, it is thus possible to obtain any value of the flow-rate ratio φ, defined as the ratio between Q_d and Q_c:

$$\varphi = \frac{Q_d}{Q_c}. \tag{3.1}$$

Although the dispersed phase is usually injected from the side channel and the continuous phase is injected from the main channel, the choice of whether one fluid is going to become the dispersed or the continuous phase is definitely determined by the wetting properties of the microchannels. If both the fluids wet the walls of the microchannel there can be a moving contact line with some dynamic contact angle θ. This situation is indesirable since the dispersed phase touches the wall and this can lead to contamination of subsequent droplets. In order to avoid this the walls must be preferentially wetted by one of the two fluids, therefore it is possible to obtain a situation in which one fluid completely wets the walls and the other is confined in droplets that never go into contact with them, due to the presence of a lubricating film of continuous phase. The ideal case is when the walls are completely wetted by the continuous phase, with $\theta = 0°$, and they are not wetted at all by the dispersed phase, with $\theta \gtrsim 120°$. This situation can be realized for example when the walls are superhydrophobic, and the continuous and dispersed phases are oil and water, respectively.

The opposite configuation of a water continuous phase and an oil dispersed phase is much more challenging. While it is relatively simple to have hydrophilic materials, i.e. wetted by water, the same material is likely to be wetted by oil as well. This is due to the fact that oils have a very low interfacial energy, thus the wetting of a material by oil is hardly discouraged. If the walls are hydrophilic enough (e.g. glass or plastics), one possibility is to first fill the microchannels by water, and only then the oil is injected in the inlet of the side channel. Hopefully, the oil will not ever get in contact with the walls, which are always surrounded by a film of water. This way the oil dispersed phase therefore effectively has a contact angle $\theta = 180$ with the water-covered walls.

Although this works, it is not stable over a long period of time. Eventually, the oil in the side channel will get in contact with the walls, and a contact line will form. This contact line will move over time downstream of the side channel up to the corner of the T-junction, and depending on the flow rates, it will overstep it. When the oil starts to wet the main channel walls the droplet break up process is strongly altered, degenerating to coflow. However, by carefully controlling the flow rates, it is possible to deal with this problem, at least for the time of the experiment. Then the microchannel can be washed in order to start again from a condition with clean, water-wetted walls.

A robust solution to this problem is to add a surfactant to the continuous phase. This will both improve the wetting of the walls by the continuous phase and help to stabilize the interface. Adding a surfactant, however, can sometimes be undesirable,

since it may be incompatible with the experiment, depending on the application. Moreover, the interfacial tension will be lowered to some value which is difficult to estimate analitically, and therefore it must be measured experimentally.

3.2 Pendant Drop

The interfacial tension between two fluids can be measured in many different ways. One simple and effective technique is based on the fact that the shape of a drop pending from a solid, e.g. a needle (Fig.3.2d), is due to a balance between gravity, which pulls the drop downward, and the interfacial tension which holds the drop attached to the solid. Locally, the interface geometry is described by the Young-Laplace equation:

$$\sigma\left(\frac{1}{R_1}+\frac{1}{R_2}\right)=\Delta P_0+\Delta\rho g z \tag{3.2}$$

where z is the vertical coordinate, in the same direction as gravity, and $\Delta\rho$ is the difference between the density of the drop and the density of the surrounding fluid. In principle, if the geometry of the drop is measured experimentally, it can be fitted by this equation in order to extract the interfacial tension σ as a fitting parameter[26].

The experiment is carried out by fixing a syringe with a simmetrical needle in the vertical position, and by taking pictures of pending drops with a camera equipped with either a telecentric or a common objective. In case a common (non-telecentric) objective is employed, the picture can be calibrated using the diameter of the needle (if it is known), which is visible in the picture itself (Fig. 3.2d). For the surface tension of a liquid with air, this is just enough. Instead, if the interfacial tension between two different liquids is of interest, the drop has to be immersed in the other liquid, which can be contained in a glass couvette.

It is important, of course, for the pending liquid to be denser than the surrounding liquid in the couvette. In the case of water and oil, the syringe is thus filled with water, and the couvette with oil, since most oils have a density in the range $0.7-0.9g/cm^3$. However, care has to be taken with other liquids, for example ethanol has a density of $\sim 0.79g/cm^3$.

Even more care has to be taken with the wetting properties of the needle, which supports the pending drop. If the needle is wetted too well by the pending liquid, then the liquid exiting from the needle will go upward wetting the outer walls of the needle itself. If this is the case, then Teflon can sometimes be used instead of metal. In all cases, however, it is important for the needle to have a precise and axial-symmetric shape. In axial symmetric coordinates, shown in Fig.3.2a, the Young-Laplace equation becomes:

$$\begin{aligned}\frac{dx}{ds}&=cos\theta\\ \frac{dz}{ds}&=sin\theta\\ \frac{d\theta}{ds}&=2b+cz-\frac{sin\theta}{x}\end{aligned} \tag{3.3}$$

with the initial conditions $x(0)=z(0)=\theta(0)=0$. The parameter $b=\pm 1/R_0$ is the curvature at the apex of the drop and $c=\Delta\rho g/\sigma=\lambda_c^{-2}$ is a constant related to the capillary lenght λ_c. The equations 3.3 can be made dimensionless with the definitions $x=R_0\bar{x}, z=R_0\bar{z}, s=R_0\bar{s}$. The last equation in 3.3 then becomes:

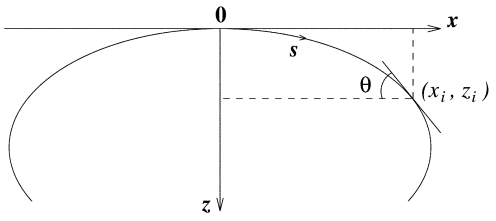

(a) Coordinates system for the droplet profile. The origin is positioned in the apex of the droplet

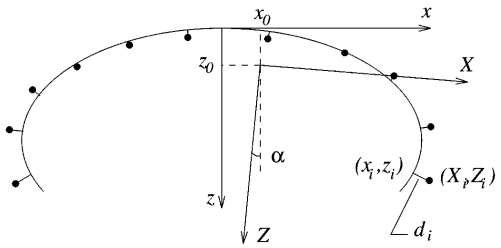

(b) Fitting procedure of the drop profile (dots) with a curve generated by solving the Young-Laplace equation (solid line). The sum $\sum d_i^2$, where d_i is the distance of the curve from the i-th experimental point, is used to estimate the distance of the curve from the experimental profile.

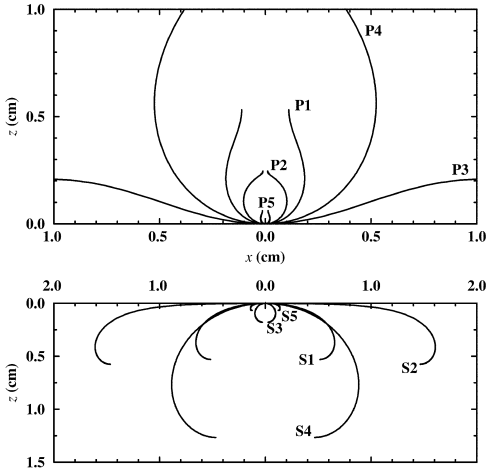

(c) Examples of curves generated by numerically integrating the Young-Laplace equation, at varying parameters. Both *pendant* (P) and *sessile* (S) drops can be obtained.

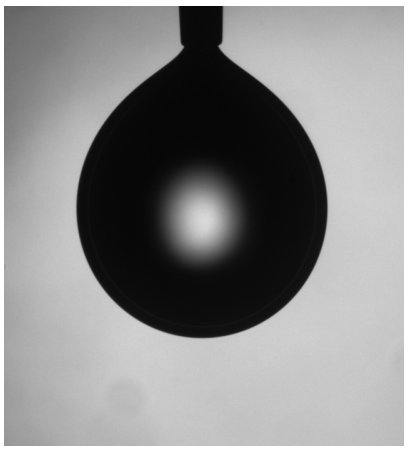

(d) Example of experimental image taken through a telecentric objective

Figure 3.2

$$\frac{d\theta}{d\bar{s}} = 2 + Bo\bar{z} - \frac{sin\theta}{\bar{x}} \tag{3.4}$$

where $Bo = \Delta\rho g R_0^2/\sigma$, called *Bond number*, is the only free parameter. The shape of the drop is thus determined only by the value of Bo, while the size of the drop also depends on the value of R_0. Depending on the sign of b and c (or the orientation of the z axis), the solution of 3.3 can represent both sessile of pendant drops (Fig.3.2c).

The ordinary differential equations 3.3 cannot be solved analitically, however they can be easily integrated numerically, e.g with a Runge-Kutta algorithm, once the parameters are fixed. The pendant drop technique consists of fitting the solutions of the equations 3.3 with the experimental drop profile (Fig.3.2b), which can be extracted from the images (Fig.3.2d) after some simple image processing. The fitting is an iterative process, called *non linear regression*, which attempts to minimize a sum squared of errors, or SSE. The error is defined as the minimum distance of an experimental profile point

from the numerically integrated curve (Fig.3.2b). The fitting procedure can be implemented with the following algorithm:

1. the parameters (b, c) are initialized with some value which, in order for the algorithm to converge to the global minimum of the SSE, should be as close as possible to the real values. The starting value of the curvature b can be estimated from the curvature of the experimental profile, while the value of c can be initialized by estimating the value of σ from the literature. Alternatively, if the software is interactive, the starting values can be adjusted by trial and error until the numerical curve look close enough to the experimental profile, which is by itself a fitting procedure.

2. with the parameters (b, c) the equations 3.3 are integrated numerically and the SSE is computed.

3. A new value of the parameters $(b^*, c^*) = (b + \Delta b, c + \Delta c)$ is estimated with an algorithm like Gauss-Newton, Levenberg-Marquardt or Gradient Descent. The increment in the parameters space $(\Delta b, \Delta c)$ is in a direction that, hopefully, leads closer to the minimum of the SSE.

4. the above two steps are iterated until convergence, i.e. until the SSE reaches a chosen lower limit value, called *tolerance*, or a maximum number of iterations is reached (in the case the algorithm fails to converge).

If the above procedure is successfull, the numerical solution of the Young-Laplace equation will closely match the experimental drop profile. From the value $c = \Delta\rho g/\sigma$ the interfacial tension σ can be extracted, assuming that the densities of the fluids are known. It is possible to statistically associate an uncertainty to the value of σ by repeating the pendant drop experiment several times with different drops.

One limitation of the pendant drop technique is that it relies on gravity. If the effect of gravity is small with respect to the interfacial tension, i.e. if the the Bond number is very small, then the drop will assume an almost spherical shape. In that case the same drop profile can be fitted well by the solutions of eq.3.3 for a large number of values of the fitting parameter c, corresponding to a range of values for σ which gives an almost spherical drop. Therefore in this situation the measured value of the interfacial tension is not reliable. The drop must be deformed by gravity, as in Fig.3.2d, thus the value of σ is uniquely determined.

3.3 Microfabrication

There are many possible ways to realize the microfluidic device descibed in section 3.1. During the course of this thesis a number of different microfabrication techniques have been employed, using the facilities available in the laboratory. The different techniques present advantages and disadvantages, in terms of flexibility, complexity, time, and the quality and specs of the final product.

3.3.1 Polyester-Toner

The Polyester-Toner (PeT) microfluidic devices are fabricated by direct-printing combined with xurography. Polyester sheets (A4 size, $100\mu m$ thick) are first printed twice

on both sides using a laser printer (Hewlett-Packard model 4250) with 600-DPI resolution and equipped with a black toner cartridge (model Q5942A). This process yields two layers of toner printing on each side of the polyester film.

The T-junction layout for the devices is drawn using the AutoCAD 2011 software and the microchannels are created in small pieces (55 mm x 35 mm) of printed polyester using a knife plotter (Craft Robo CC200-20, Graphtec). The main steps of the fabrication process are outlined in Fig. 3.3A-E. The cut-through printed polyester film is placed between two unprinted polyester layers; with the upper one provided with access holes made with a paper punch. The three polyester sheets are then laminated using an office laminator at $150°C$. Finally, reservoirs are constructed by gluing small pieces of rubber tubes (4 mm of i.d. and 10-mm-long) with epoxy resin (Fig.3.3F).

This procedure allows to produce channels having a minimum width of $60\mu m$ and heights of $120\mu m$. The width is set by the resolution of the knife plotter, while the height is set by the thickness of the middle polyester sheet ($\sim 100\mu m$) and the toner layers. The thickness of one layer of toner is about $7\mu m$ as determined with a micrometer. Thus, the four toner layers result in a total height of about $28\mu m$, which decreases to about $20\mu m$ after the lamination process. Photos of channels cross-sections of different width are shown in the bottom part of Fig.3.3. For the smallest channels, the observed irregularities are also due to the cutting of the chip with a razor blade to open up the cross-section. More generally, the surface finish depends on the quality of the cutting plotter.

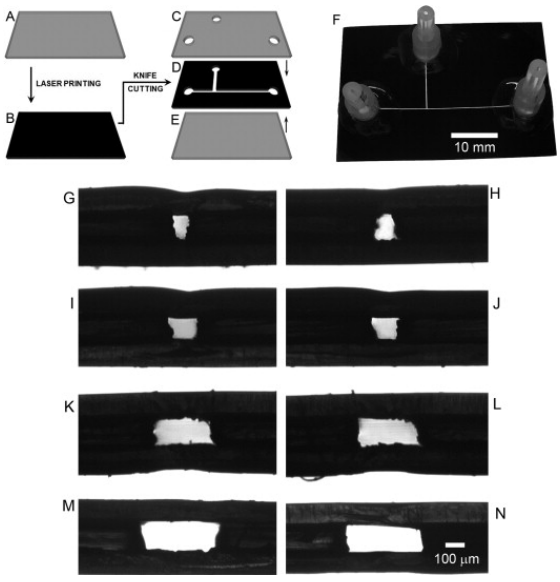

Figure 3.3: Schematic diagram showing the main steps of the fabrication process: (A) polyester film, (B) polyester film toner-printed on both sides, (C) polyester film with perforated access holes, (D) microchannels cut on the printed polyester, (E) polyester film used for sealing. (F) Full view photograph of the T-junction microfluidic device constructed in PeT. (G-N) Photographs of the cross-section of microchannels of different sizes. Each image refers to a different PeT chip. Characteristic widths: (G and H) $60\mu m$; (I and J) $90\mu m$; (K and L) $250\mu m$; (M and N) $350\mu m$.

3.3.2 Photo and Soft Lithography

The T-Junction device is made using standard photo-lithography and replica-molding techniques[27, 28]: a master is first made in SU-8 on a silicon substrate using UV photolitography, through a mask with the desired geometry. The master is then casted in

PDMS to obtain a negative replica of the geometry of the master. The replica-molding process from the same master can be repeated as many times as needed, providing multiple identical copies of the T-junction geometry.

The master can be either a positive or a negative representation of the final geometry of the microchannels. A PDMS replica of a negative master can be used straight away to make a chip, by closing it with a microscope glass, while a PDMS replica of a positive master can be used instead as a master itself. The latter can be useful in particular for replica molding with other kinds of polymers, like the epoxy based resin NOA, which is described later.

Master

The T-junction pattern is designed with AutoCAD (Autodesk, Mill Valley, CA, USA) and transferred to a transparency-based photomask using a high-resolution printer (4000 DPI). In a Class-V Clean Room a silicon wafer is spin-coated with the negative photoresist SU-8 (2050, MicroChem Corp.) and exposed to UV light through the photomask, then it is cured. Finally, the master is silanized in order to ease the peeling off of the subsequent replicas.

PDMS replica

The PDMS pre-polymer (Polydimethylsiloxane, Sylgard 184, Dow Corning) and its cross-linker are mixed in a ratio of 10:1 (w/w), stirred thoroughly and degassed under vacuum. The SU-8 master is then prepared, by fencing it with alluminium foil or putty, in order to avoid PDMS spilling. The PDMS is then carefully poured onto the master up to a height of about $5mm$ and, if any, air bubbles are removed with a needle. The master with PDMS is then cured in an oven at $80°C$ for about 1 hour, after which the PDMS replica is carefully peeled off from the master and wrapped in aluminium foil in order to keep it clean. In order to make access holes for the external tubing, the PDMS is perforated with a steel needle in the three points corresponding to the two inlets and the outlet.

Plasma Bonding

The PDMS replica and a microscope glass (precedently cleaned with distilled water, acetone and ethanol) are put under an oxygen plasma treatment using a FEMTO Plasma System (Type B, 0-1000 W, Diener Electronic, Ebhausen, Germany) at a power of 300 W for $0.8min$ (48 s). The two pieces are then put in contact, carefully removing any entrapped air by pushing it out from the inlet and outlet holes. After a few seconds, the PDMS replica is irreversibly bonded to the glass. The internal walls of the microchannels remain chemically reactive, due to the plasma treatment, for as long as roughly $1/2 - 1$ hour, after which the PDMS exposed to air returns to it natural state. It is possible to exploit this temporary surface chemistry of both the PDMS and the glass to functionalize the walls.

Functionalization

After a few minutes ($\sim 10min$) from the bonding, the chip is sealed and can be already used. Teflon tubing are temporarily inserted in the holes and a solution of 5% PVP/Water (Polyvinylpyrrolidone K90, AppliChem) is slowly flowed (at $\sim 1\mu$L / min) through the microchannels with a syringe-pump for about 30-45 minutes, after which

they are flushed with distilled water and dried out with compressed air. As a result, both the PDMS and the glass walls are coated with a thin, permanent hydrophilic layer of PVP, allowing then to use an aqueous continuous phase with no wettability issues. As a last step, the tubing are then permanently glued with a drop of PDMS, which is then cured again in then oven.

The PVP solution must be flowed in the microchannel while the internal walls are still chemically activated by the plasma treatment, otherwise the inert PVP molecules will not react with the surfaces.

It is possible to functionalize the walls in a later moment, i.e. without exploiting the plasma treatment, by exposing the microchannels to a silane, which is composed of chemically reactive molecules. In particular, hydrophobic microchannels are made by flowing a solution 1mM OTS/Hexadecane (Octadecyltrichlorosilane, Sigma Aldrich) which will coat both the PDMS and the glass walls, allowing to use an oil continuous phase with no wettability issues.

3.3.3 NOA

Another polymer that can be used in microfabrication is NOA, or Norlad Optical Adhesive. It is slightly hydrophilic, having a contact angle of $\sim 70^{\circ}$, and thus it is an interesting material to make a T-Junction when a acqueous solution is going to be employed as the continuous phase. NOA81 (Norland Products) is a thiolenic resin that cross-links when exposed to UV light, and can be used as a photoresist in a similar way as the SU-8 photoresist.

NOA can be used also for replica molding. When it is cross linked, NOA is hard and not elastomeric as the PDMS, therefore it is not suitable to use with a SU-8 master on a silicon substrate. However, a positive SU-8 master can be casted with PDMS, and the (negative) PDMS replica can be used as the master for NOA. The PDMS master is in fact elastomeric and can be detached easily from the NOA replica. Moreover, NOA does not stick to PDMS, thus the master does not need to be silanized first.

The PDMS master is prepared by inserting pieces of metal wire in the inlets and the outlet. This way, after cross-linking, the NOA replica will have already the access holes where the tubing will be inserted. These otherwise need to be drilled in a later step. After fencing the master with putty (to avoid spilling of the liquid NOA), NOA is poured and put under UV light (365 nm) for about 1 h (depending on the thickness).

If the thickness of the NOA is large, e.g. 3-4mm, the cross linking will not be homogeneous and the NOA will cure on the UV exposed side first, and less effectively close to the master.This can results in a slightly curved replica, which cannot easily be closed on a microscope glass. One possible solution is to close the NOA replica with piece of transparency foil (Polyester) which is both transparent and flexible, and thus can adapt to the rounded shape of the replica. The piece of transparency foil is first spin coated with a small layer of NOA, and is then partially cured with UV light (for roughly 1 min), in order to avoid obstruction of the microchannels. The NOA replica is then closed with the sticky transparency foil and put under the UV light for about 30 min in order to complete the curing. Finally, tubing are inserted in the access holes and glued with a drop of NOA, with subsequent exposure to UV light.

3.4 Experimental setup

A custom made software controls the pumps and a high speed Camera-Link CMOS camera (EoSens CL MC1362, Mikrotron) coupled to an inverted microscope (Eclipse Ti-E, Nikon), which acquires images of the droplets. The same software analyzes the images in a region of interest far downstream of the T-Junction where the droplets are fully formed. All the droplets crossing this region are tracked, measuring quantities such as the droplets lenght L, velocity u and the time interval T between consecutive droplets in real-time (up to ~ 1000 fps). It thus allows to acquire quantitative information for a large amount of droplets in limited time and storage space, reducing the number of saved images to be just enough to cover a few full droplet breakups, for offline qualitative analysis. More importantly, it allows to monitor whether the droplets production has reached stability (i.e. the average droplet size has become constant in time) before starting to collect data.

3.4.1 Droplet size estimation

Volume

The volume of the droplets in a ideal thread of equally spaced identical droplets can be computed from the frequency of droplets f by the relation $V = Q_d 1/f$. This can be estimated using the measured time interval between consecutive droplets T, by the relation $V = Q_d \langle T \rangle$. While this usually works reasonably well, however at very high flow rates it becomes difficult to measure T due to the overall speed limitation of the acquisition system (camera and software), and at very low flow rates the same T has a large error, even if the volume has not, due to limitations of the syringe-pumps and the overall microfluidic system. Further, estimating the droplet polydispersity is not a simple task[15].

Lenght

Another approach is to use the average normalized droplet length L/W (and corresponding error) to estimate the droplet size, as it is directly measured from the images and makes a direct estimation of the droplet polydispersity possible. More precisely, the average lenght is estimated by the median of the lenghts, which is not affected by the outliers (due to image processing and tracking failure) that are sometimes present when the acquisition system is pushed to the highest speeds. Correpondingly, for the same reason, the error is computed by the Inter Quartile Range (IQR). The lenght, with respect to volume, however introduces other drawbacks. It depends on the droplet shape, scaling linearly with the volume when the droplets completely fill the microchannel, while scaling as $L \sim V^{1/3}$ when the droplet is small compared to the channel width and has a spherical shape. Therefore the measurements need to be carefully interpreted. A limitation in measurement of the droplets arises when they are either too long to stay in the field of view, or when the inter-droplet distance is small and has large fluctuations (at very low flow rates), because the fixed region of interest can not be suitable for all droplets. In these cases the measurement is not possible by the current setup.

Chapter 4

Generation of droplets with disposable polyester-toner microfluidic devices

In this chapter disposable polyester-toner microfluidic devices are used to produce either water-in-oil (W/O) or oil-in-water (O/W) droplets without using any surface treatment of the microchannels walls. Highly monodisperse W/O and O/W emulsions are generated with the T-junction geometry by simply adding appropriate surfactants to the continuous phase. The dispersion in size of droplets generated at frequencies up to 500 Hz is always less than about 2% over time intervals of a couple of hours. The polyester-toner microfabrication technique, when applied to droplet-based microfluidics, is demonstrated to be a flexible and valuable low-cost alternative to the more expensive and demanding standard microfabrication techniques, when the applications do not require high resolutions in the channels geometry.

4.1 Introduction

The generation of stable droplets depends, among other things, on the wettability of the channel walls. The continuous phase should completely wet the channel walls, while the degree of wetting by the dispersed phase should be very low. Oils preferentially wet hydrophobic surfaces, whereas aqueous solutions preferentially wet hydrophilic surfaces. Thus, W/O droplets are usually produced in hydrophobic microchannels and O/W droplets are commonly generated in hydrophilic devices. Most published studies involve the production of W/O droplets because the majority of biological and chemical reactions occur in an aqueous solution [29], [30], [31] and [32]. This significantly simplifies the fabrication of microfluidic devices because it requires hydrophobic walls, a feature guaranteed by the use of common polymers. These include polydimethylsiloxane (PDMS) [33] and [34] and poly(methylmethacrylate) (PMMA) [35] and [36]. However, when O/W droplets are needed, the polymeric channel walls must be turned hydrophilic. Over the past few years various methodologies [30], [31], [37], [38] and [39] have been devised to accomplish this task, which are usually technically demanding and time consuming. An alternative way consists in the addition of suitable surfactants to the continuous phase [29] and [40].

The direct-printing technology for fabricating toner-based microfluidic devices was first proposed by do Lago et al. [41]. In this technique, the device layout is laser-printed

on two sheets of polyester film that are then sealed together by thermal lamination in order to create the channels. The toner printing acts as a glue in the lamination process. The depth of the channels ($\sim 12\mu m$) is determined by the height of the two toner layers that are laminated together. More recently, this fabrication process was modified in order to produce multilayered polyester-toner devices with larger channel depths [42]. In this latest methodology, the microchannels are made by cutting a polyester sheet containing uniform layers of toner. This cut-through sheet is sandwiched between uncoated polyester sheets containing precut access holes. Thus, the depth of the channels is determined by the number and the thickness of the middle cut-through sheets and the toner layers. When compared to other rapid prototyping techniques, the toner-based technology presents some advantages owing to its very short fabrication time, independence of clean room facilities and low cost ($\sim \$0.15$ per device) [43]. Polyester-toner (PeT) devices have found widespread applications in many areas including clinical bioassays [43], microchip electrophoresis [44], DNA extraction and PCR amplification [42], and DNA analysis [45]. However, all of these applications were developed for conventional continuous flow systems and, considering the increasing demand for droplets based devices [46] and [47], it would be important to merge these two technologies.

In the following sections it will be shown that PeT (Polyester-Toner) technology is capable of supporting droplet microfluidics, by demonstrating that T-junctions made in PeT can be used to generate droplets that are highly monodisperse and are separated by an equal spacing [46], [47], [48] and [49]. These disposable PeT devices can be used to make either W/O or O/W droplets without any surface modification of the microchannels.

Stable W/O droplets are obtained using hexadecane or mineral oil as continuous phases with the addition of Span 80, while O/W droplets are obtained using aqueous solution with Triton X-100 as continuous phases and hexadecane or mineral oil as dispersed phases. Surfactants are added to the continuous phase in order to lower the interfacial energy, that is to facilitate the formation of new interfaces and to stabilize the formed emulsion droplets from coalescence during their motion [49] and [40].

4.2 Materials and Methods

All chemicals used are of analytical reagent grade quality and are employed as received. Hexadecane (CAS number: 544-76-3, viscosity $\sim 3cP$, density $\sim 0.77g/cc$), mineral oil (light) (CAS number: 8042-47-5, viscosity $\sim 16cP$, density $\sim 0.84g/cc$), Span 80, and Triton X-100 were purchased from Sigma-Aldrich. Polyester sheets (transparency films, model CG3300) were acquired from 3 M. Distilled water was used in all experiments.

The microfluidic devices used for droplets generation are made in PeT with a T-junction layout [14], with an overall size of 40 by 20 mm. The fabrication procedure of these devices is described in the previous chapter in section 3.3.1. All experiments are conducted in microfluidic channels with widths of $\sim 250\mu m$ and height of $\sim 120\mu m$. These devices have been used repeatedly up to a couple of weeks without noticing any variation in their performance.

The liquids are introduced into the microfluidic devices through flexible polyethylene tubing ($0.5mm$ i.d.) and plastic syringes ($5ml$), using two independent syringe pumps (PHD 2000, Harvard Apparatus) working at constant flow rates between 0.5 and $20\mu L/min$. The images of on-chip droplet formation are obtained using a monochrome

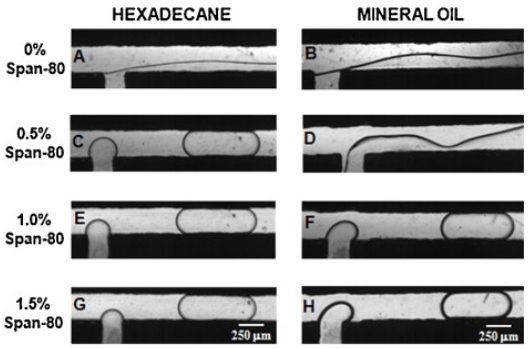

Figure 4.1: Optical microscope images showing the generation of W/O droplets in the PeT devices. Hexadecane and mineral oil are used as continuous phases in the absence (A and B) and with increasing concentrations of Span 80 (C-H). The flow rates of the continuous and dispersed phases are 5 and $3\mu L/min$, respectively.

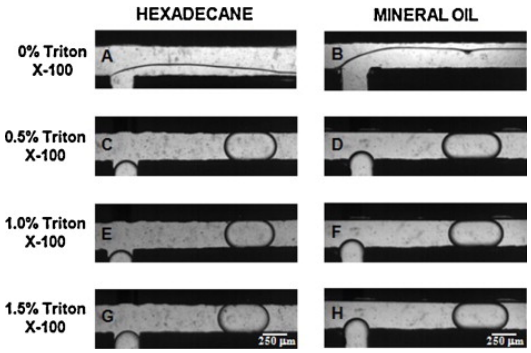

Figure 4.2: Optical microscope images showing the generation of O/W droplets in the PeT microfluidic devices. Hexadecane and mineral oil are tested as dispersed phases, while pure water (A and B) and aqueous solutions containing increasing amounts of Triton X-100 (C-H) are used as continuous phases. The flow rates of the continuous and dispersed phases are 5 and $1\mu L/min$, respectively.

camera (MV D1024 CMOS, Photonfocus) coupled to an inverted microscope (Eclipse Ti-E, Nikon). All data presented in the next section refer to as made chips. The chips have never been reused flowing different liquids in the channels.

4.3 Results and discussion

4.3.1 Wetting properties of PeT

The static contact angle (CA) of water on the transparency (polyester) surface is measured to be $49 \pm 2°$, and this value compares well with recently reported data [50]. The partial hydrophilicity of the polyester surface together with the addition of suitable surfactants to the corresponding continuous phase are the key ingredients for the effective production of stable W/O and O/W droplets in the same PeT device. Since the wettability of thiolenic resins is similar to that of polyester, W/O and O/W droplets generators are also expected to be successfully fabricated in thiolene by rapid prototyping techniques [51].

Water in oil droplets

The first studies aim at producing W/O droplets. Hexadecane and mineral oil (viscosity $\sim 3cP$, density $\sim 0.77g/cc$) are evaluated as continuous phases in the absence and with different concentrations of the lipophilic nonionic surfactant Span 80. A series of pictures showing the formation of water-in-hexadecane and water-in-mineral oil droplets in the PeT T-junction is displayed in Fig. 4.1 for different surfactants concentrations. In the absence of the surfactant, no droplets are obtained and a continuous water stream is formed parallel to the oil continuous phase (see Fig. 4.1A and B). Stable water-in-hexadecane droplets are obtained after adding $0.5\%(w/w)$ of Span 80 to the continuous phase (Fig. 4.1C). However, 0.5% of Span 80 is not enough to generate water-in-mineral oil droplets (Fig. 4.1D). Stable water-in-mineral oil droplets are obtained only when the concentration of Span 80 is $1.0\%(w/w)$ (Fig. 4.1F).

Hexadecane completely wets the polyester surface while pure mineral oil forms a $CA = 10 \pm 2°$, which remained practically constant ($9 \pm 2°$) after the addition of $1.0\%(w/w)$ of Span 80, suggesting that the wettability of the channel walls by the oil phase was not affected by the presence of Span 80. Thus, the surfactant is facilitating the on-chip droplets generation by reducing the interface tension between the continuous and discrete phases and by preventing the coalescence of the resulting droplets [39]. The droplet length is found to be independent of surfactant concentration for both water-in-hexadecane (Fig. 4.1C, E, and G) and water-in-mineral oil (Fig. 4.1F and H) droplets. This behavior is expected once the minimum interfacial tension between the two liquids is achieved and this condition occurs whenever the surfactant concentration is over the critical micelle concentration ($0.03\%(w/w)$ and $0.025\%(w/v)$ for hexadecane and mineral oil [29, 52]).

Oil in water droplets

The production of O/W droplets in the polyester-toner devices are carried out using hexadecane and mineral oil as dispersed phases. Pure water and aqueous solutions containing different amounts of the surfactant Triton X-100 are tested as continuous phase. Fig. 4.2 displays optical microscope images about the formation of oil-in-water droplets.

Again, without the surfactant, no droplets are formed and the two liquids form two parallel streams (see Fig. 4.2A and B). The addition of 0.5% of Triton X-100 to water leads to the formation of reproducible and well defined hexadecane-in-water and mineral oil-in-water droplets (Fig. 4.2C and D). The reason is likely the enhanced wettability of the channel walls by the continuous aqueous solution. Actually, after the addition of 0.5% of Triton X-100, the CA of water is found to decrease from $49 \pm 2°$ to $13 \pm 2°$. As observed in the production of W/O droplets, the length of the O/W droplets also remains constant upon increasing the surfactant concentration to 1.0% and $1.5\%(w/w)$ (Fig. 4.2E-H). As the critical micelle concentration of Triton X-100 in water is $0.015\%(w/v)$[1], the interfacial tension between the two phases is at its minimum value for all the considered surfactant concentrations.

Fluorocarbon oil compatibility

For biological applications, it is attractive to use a fluorocarbon oil as the continuous phase, as these oils are both hydrophobic and lipophobic, hence they have low solubility for the biological reagents of the aqueous phase and are well suited for inhibiting molecular diffusion between drops [33]. The compatibility of two common fluorocarbon oils, FC40 and HFE 7500, is tested with Pe foils. They both completely wet the Pe surface and no indication of swelling is found after the oils have been kept in contact with Pe for one day. Since their viscosities (FC40 $\sim 4.1cP$, HFE 7500 $\sim 1.2cP$) are quite similar to that of hexadecane, it is expected that they can also be successfully used in PeT droplet generators.

4.3.2 Performance

For a more complete evaluation of the performance of these PeT chips, the production of droplets is studied over a time scale of about 2 h. Sequences of more than 50 droplets are acquired in time intervals of 60 s separated by 20 or 30 min, and the length

[1]Sigma-Aldrich Co. (1999) TX100, T9284 product information sheet (Sigma-Aldrich, St. Louis).

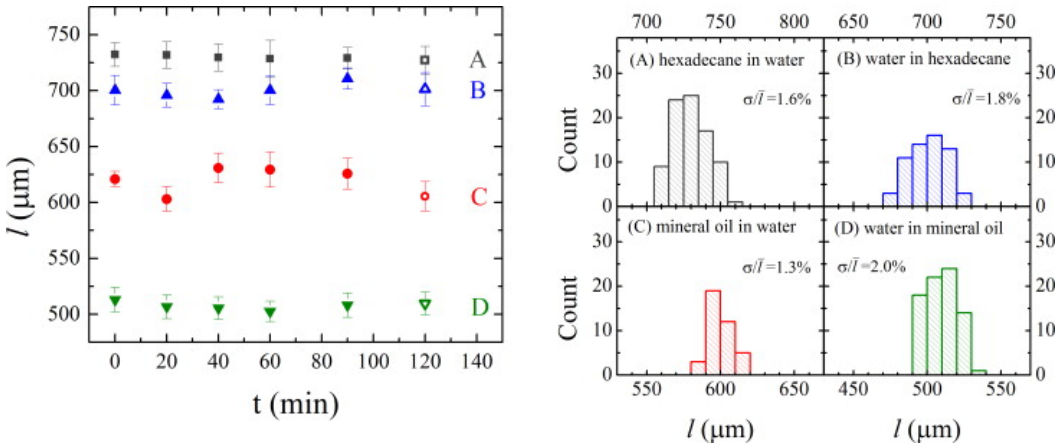

Figure 4.3: *Left*: stability over time of the length of droplets of different types produced with PeT devices. A data point corresponds to an average of at least 50 measurements. Each type of droplet has been produced in a different chip. (A) Hexadecane-in-water, (B) water-in-hexadecane, (C) mineral oil-in-water, and (D) water-in-mineral oil. *Right*: histograms showing the size distribution for the four types of droplets.

Dispersed Phase	**Continuous Phase**	$\mathbf{Q_d}$ $(\mu l/min)$	$\mathbf{Q_c}$ $(\mu l/min)$	$\mathbf{Q_d/Q_c}$
Water	Mineral oil + 1.5% (w/w) Span 80	2	5	0.4
Water	Hexadecane + 0.5% (w/w) Span 80	2	7	0.3
Hexadecane	Water + 1.0% (w/w) Triton X-100	5	8	0.6
Mineral oil	Water + 1.5% (w/w) Triton X-100	2	10	0.2

Table 4.1: Fluidic conditions of the trains of droplets presented in Fig. 4.3.

l of the droplets is then analyzed. The graph in the left part of Fig. 4.3 displays the mean values $\bar{l}$ of each sequence together with the accompanying dispersion σ for the four different combinations tested in this work. It clearly appears that the stability in time of the droplet generators is quite good and this implies that the mechanical stability of the device, as well as that of the channels walls wettability, is quite good. For instance, after storing some used chips in a cabinet for a couple of months, the measurements have been repeated with the same combination of liquids without finding any difference with respect to their initial performance. In the case of PDMS channels which have been functionalized to become hydrophilic after an oxygen plasma treatment, this effect usually disappears after they have been exposed to air for a couple of hours [30].

The four accompanying histograms in the right part of Fig. 4.3 report the droplet size distributions corresponding to the empty symbols in the graph taken after 2 h. The resulting polydispersity, i.e. the ratio $\sigma/\bar{l}$, is always less than 2%. The variations in $\bar{l}$ for the four combinations are due to the different flow rates employed in the measurements. The data on the stability over time of the PeT droplet generators presented in Fig. 4.3 are acquired under the conditions summarized in Table 4.1.

The production of droplets has then been systematically analyzed varying the two flow rates Q_d and Q_c of the dispersed and continuous phases. Fig. 4.4 shows the summary of these measurements. The graph displays the variation of the droplet length l, normalized to the channel width w, as a function of the ratio between the two flow rates Q_d and Q_c. Each data point refers to a different chip and different combinations of the two liquids plus surfactants. The chips have the same nominal width $w = 250\mu m$ and height $h = 120\mu m$. The vertical error bars are mainly due to the cross-section

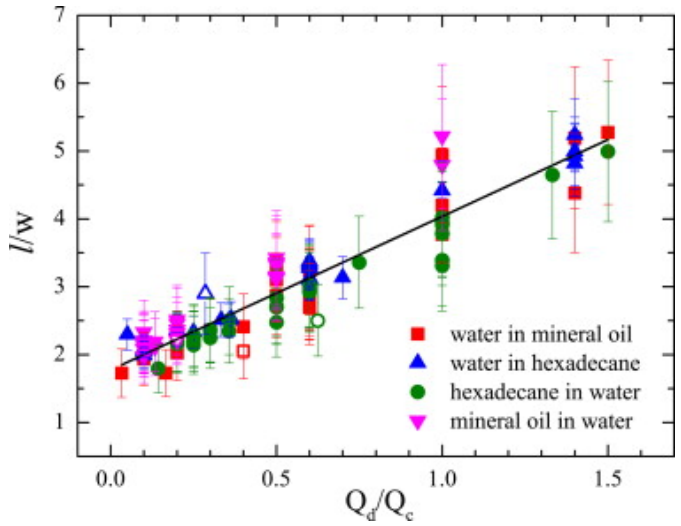

Figure 4.4: Normalized droplets length as a function of the ratio between the flow rates of the dispersed and continuous phases. Each point corresponds to a different chip. The empty symbols refer to the data presented in Fig. 4.3. The error bars are mainly due to the uncertainty in the determination of the channels width w. The straight line is a linear fit to all the data.

irregularities, as shown in Fig. 3.3 in the previous chapter. According to this optical investigation, the estimated deviation of the channel size w is about $50\mu m$. Despite the ample variations of all system variables, the data are found to collapse in a narrow region of the graph and the points are statistically consistent within one standard deviation. The observed scatter is likely to be significantly reduced if a better cutting plotter is employed.

In the squeezing regime, the dynamics of break-up is dominated by the pressure drop across the droplet as it forms [25]. The length of the droplets can be conveniently expressed with the following scaling equation:

$$\frac{l}{w} = \alpha + \beta \frac{Q_d}{Q_c} \tag{4.1}$$

where α and β are two fitting parameters, whose value is mainly affected by the geometry of the T-junction [53]. The straight line appearing in the graph is the linear fit to all the data with $\alpha = 1.8$ and $\beta = 2.3$. These values compare well with those in the literature [53] and confirm the robustness of PeT droplet generators.

The chip-to-chip reproducibility is checked by comparing the lengths of water-in-hexadecane and hexadecane-in-water droplets produced in three different devices working at the same flow conditions. The results are summarized in Table 4.2. The flow rate of the continuous phases (hexadecane with $1\%(w/w)$ Span 80 and distilled water with $1\%(w/w)$ Triton X-100, respectively) is $7\mu L/min$, while the one of the dispersed phases (distilled water and hexadecane, respectively) is $3\mu L/min$. The mean droplet size deduced from analysing more than 50 drops is found to change by less than 10% among the chips. Again, these variations are likely due to the cheap cutting plotter employed in this work. A better one will significantly improve the chip-to-chip reproducibility.

High-frequency generation of small volume droplets is useful for biological assays as the individual, picoliter-scale microvessels can contain small numbers of molecules or cells which can nevertheless be at biologically relevant concentrations [33]. In a T-junction generator, the droplet frequency depends also on the flow rates of the two

Water-in-hexadecane		Hexadecane-in-water	
Microchip	Drop length (mm)	Microchip	Drop length (mm)
1	1.41 ± 0.02	1′	0.49 ± 0.02
2	1.55 ± 0.03	2′	0.62 ± 0.02
3	1.34 ± 0.03	3′	0.56 ± 0.02
Mean	1.43 ± 0.11	Mean	0.56 ± 0.07

Table 4.2: Mean lengths of water-in-hexadecane and hexadecane-in-water droplets measured in six different chips.

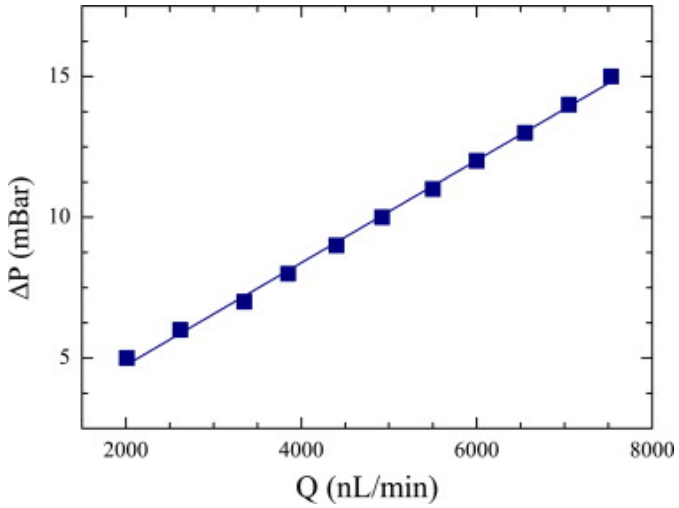

Figure 4.5: Flow rate Q induced by an increasing pressure gradient ΔP applied across a PeT microchannel.

injected (immiscible) liquids: higher frequencies are achieved with higher flow rates. The channels therefore must be able to sustain considerable pressures, up to a few bars. The maximum sustainable pressure is the one above which the PeT channels start to delaminate and leak. This can be evalueated exploiting the fact that the flow rate Q in a microfluidic channel depends linearly on the pressure gradient ΔP along it, i.e. $\Delta P = R \cdot Q$, where R is the hydrodynamic resistance of the channel. In particular, straight microchannels have been fabricated for this purpose, with cross sections of about $60\mu m$ by $120\mu m$ and length of $2.5cm$. A flow controller (MFCS-Flowell, Fluigent) is used to inject distilled water with small, known pressure gradients ΔP across the channels and the resulting flow rate Q is measured. The graph in Fig. 4.5 shows a representative set of data. The straight line is the linear fit to the data. The channel flow resistance R is the slope of this curve, which is equal to $1.87 \pm 0.02 mBar\ min/\mu L$. This value compares reasonably well with $2.5 \pm 1 mBar\ min/\mu L$ calculated for a straight channel having a rectangular cross section with width $w = 60\mu m$ and height $h = 120\mu m$, a length $l = 2.5cm$ and a water viscosity of $0.9cP$ corresponding to $25°C$ [54]. The large error mainly reflects the uncertainty in the width w of $\sim 10\mu m$ due to irregularities in the cross-section as shown in Fig. 3.3 in the previous chapter. Afterwards, the channel is connected to a syringe pump (PHD 2000, Harvard Apparatus) and an increasing flow rate is applied in steps of $100\mu L/min$. The channels are found to leak at a flow rate of about $1200\mu L/min$, corresponding to a $\Delta P \sim 2.3bar$. In conventional PDMS channels used for the production of droplets at high frequency, the typical pressures used to produce droplet are normally below $1.5bar$ [55]. Therefore, the PeT chips can be successfully employed in similar conditions. Finally, droplet generation in PeT devices is measured at the maximum flow rates reachable with the setup. Droplets of water in

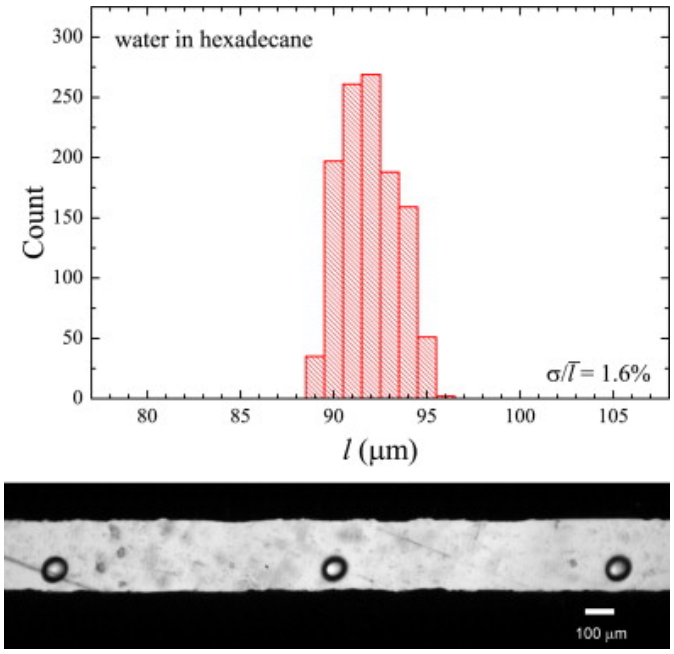

Figure 4.6: *Top*: histogram showing the size distribution of water-in-hexadecane droplets produced at a frequency of 550 Hz. *Bottom*: optical image of the droplets flowing in the main channel.

hexadecane with $2\%(w/w)$ Span 80 are produced at a frequency close to $550Hz$ with $Q_d = 10\mu L/min$ and $Q_c = 800\mu L/min$. The analysis of the droplets images taken with a fast camera (Phantom VRI v7.3) yield the histogram shown in Fig. 4.6 which presents a polidispersity of 1.6%, compatible with those measured at much lower frequencies (a few Hz) of Fig. 4.3. The droplet volume is of about $0.4nL$ and, as evident by the snapshot of Fig. 4.6, the PeT device is working in the dripping regime [25] and [53].

4.4 Conclusion

In conclusion, T-junction microfluidic devices constructed in polyester-toner have been demostrated to be suitable for generating highly monodisperse W/O and O/W droplets in the same device without any specific surface treatment of the channels walls. This is mainly due to the partial hydrophilicity of the polyester surface together with the addition of suitable surfactants. The fabrication procedure is characterized by being very simple, fast and inexpensive. We estimate that it is possible to complete the whole fabrication in less than 10 min, with a cost of $\sim \$0.10$ per device. This makes the lamination of PeT foils the fastest and cheapest rapid-prototyping technique. Actually, the standard chips in PDMS require the fabrication of a master, typically done by lithography, and a process in oxygen plasma for the sealing of the chip. Furthermore, PDMS is hydrophobic so that the formation of O/W drops needs prior functionalization of the surface walls. On the other hand, very uniform channels of any size can be made by replica molding of PDMS. The poor resistance of PeT and PDMS chips to organic solvents can be overcome using glass chips. The production of W/O drops in these chips requires a functionalization of the surface walls. However, the main limitation of glass chips is the difficulty in fabrication. There are commercial companies selling them with standard and custom designs at a starting cost of tens of $ per piece. Table 4.3 reports a synthetic comparision between the PeT chips for droplet productions with

respect to those made in PDMS and glass. The features of the PeT chips and the possibility of large-scale production make the polyester-toner technology very attractive for widespread utilization also in droplet-based microfluidics.

	PeT	**PDMS**	**Glass**
Rapid prototyping	Yes	Yes	No
Channel size	Minimum height set by PE thickness. Minimum width set by plotter blade.	Any	Any
Channel uniformity	Good (depends on cutting plotter)	Very good	Very good
Chip sealing	Lamination	Oxygen plasma	Thermal bonding
Equipment required	Very cheap and simple	Standard equipment for microfabrication	Specialized equipment for microfabrication
Chemical resistance	No organic solvents	No organic solvents	Very good
Water contact angle	$50°$	$110°$	$< 20°$
Droplets combination without surface treatment	W/O and O/W	W/O	O/W

Table 4.3: Main specs of microfluidic droplets generators made in different materials.

Chapter 5

Droplet production in Non-Newtonian Continuous phases

The breakup dynamics of a fluid stream injected into a second, immiscible liquid and the consequent formation of droplets are relatively well understood in the case of two immiscible Newtonian fluids, such as water and oil [14, 16, 25, 56]. Recently, this investigation has been extended to non-Newtonian liquids because of their importance in real applications. Actually, non-Newtonian liquids involve physiological fluids [57] such as blood (including fibrinogen to fibrin formation [58]) synovial or salivary fluids [59], as well as fluid jets in printing and spraying technology [60, 61], and food emulsions [62, 63]. Most of the attention has been so far focused on the formation of non-Newtonian droplets carried by Newtonian continuous phases [64, 65]. For elastic polymers, the effect of the molecular weight on filament thinning has been clarified in flow-focusing devices [66, 67]. Only a few studies considered droplets carried by a non-Newtonian medium, using either flow focusing geometries [68, 69], or air bubbles formation [70]. Accordingly, an exhaustive description of the breakup mechanism driven by non-Newtonian continuous phases in T-junctions is still effectively lacking.

This chapter reports a comprehensive and systematic study of the droplet breakup in a microfluidic T-junction, involving Newtonian droplets formed in either Newtonian, purely shear-thinning or purely elastic (Boger) fluids. As shear-thinning fluids, dilute and semidilute solutions of Xanthan, a stiff rod-like polysaccharide, are investigated. At the concentrations considered, they exhibit a well pronounced shear thinning behaviour with finite thinning exponents, while weak elastic effects emerge only at relatively high concentrations [71, 72]. The role of elasticity is instead investigated using solutions of polyacrylamide. In order to isolate the elasticity from the shear-thinning behaviour, a Boger fluid is employed, which is characterized by a constant viscosity due to a particular choice of the solvent.

Preliminary experiments are first carried out with both polyacrylamide (PAA) and Xanthan solutions. From the experiments with PAA results that, while the shape of droplets formed in the Boger fluid is considerably altered with respect to the one in the corresponding Newtonian, there is no strong evidence for the elasticity to affect the droplets size resulting after breakup.

Instead, by quantitatively comparing Newtonian and shear-thinning data, robust experimental evidence is provided that the droplet size rescales nicely with an effective Capillary number ($\overline{\mathrm{Ca}}$), which reduces to the usual Capillary number (Ca) when both liquids are Newtonian. Systematic experiments with Xanthan are complemented with numerical simulations of purely thinning fluids based on the lattice Boltzmann

models (LBM), which are in good quantitative agreement with the experimental data and confirm the proposed scaling.

This chapter is organized as follows: in Section 5.1 the materials and the experimental and numerical methodologies are presented. In particular, the effective Capillary number is introduced in Sec. 5.1.3. Experimental preliminary results involving both shear-thinning and elastic fluids are reported in Sec. 5.2. Sec. 5.3 reports the results of the systematic experiments with the shear-thinning Xanthan solutions, complemented in Sec. 5.4 with the results of the numerical simulation with pure thinning fluids. Conclusions and final remarks are discussed in Sec. 5.5.

5.1 Materials and Methods

5.1.1 Liquids

Table 5.1 reports the main physical parameters of the Newtonian liquids used in this study, as deduced from the literature [73, 74] or measured directly. For the non-Newtonian

Liquid	$\boldsymbol{\rho}(g/cm^3)$	$\boldsymbol{\sigma}(mN/m)$	$\boldsymbol{\eta}(mPas)$
Hexadecane	0.77	-	3
Linseed oil	0.93	-	22.3
Soybean Oil	0.917	-	49.1
Water	0.997	72	0.89
Glycerol/Water 40% (w/w)	1.09	69	3.22
Glycerol/Water 60% (w/w)	1.15	67	9
Glycerol/Water 67% (w/w)	1.17	66	14.5
Glycerol/Water 80% (w/w)	1.21	65	43
Glycerol/Water 85% (w/w)	1.22	64	79

Table 5.1: Main physical properties of the Newtonian liquids used in this study: density ρ, surface tension σ, dynamic viscosity η.All data refer to a temperature of $25^{\circ}C$.

liquids, aqueous solutions of xanthan (molecular weight, $Mw \sim 10^6 g/mol$, Sigma Aldrich) are prepared at different concentrations. The rheology of the xanthan solution is characterized with a parallel plate rheometer (Ares TA Instruments, New Castle, DE, USA). Figure 5.1 shows the dependence of the viscosity on the shear rate for the xanthan solutions at different concentrations. The viscosity η_{Xan} of the xanthan is expected to vary with the shear rate $\dot{\gamma}$ according to the power law fluid model:

$$\eta_{Xan} = K\dot{\gamma}^{(n-1)} \tag{5.1}$$

where K is the flow consistency and n is the flow behavior index, both dependent on the polymer concentration [75]. Table 5.2 shows the fitting parameters for the three solutions. The data are in good agreement with the ones reported in [76] that explore a range of concentration and shear rate larger than the one accessible by rheometer employed in this work.

The Boger fluid used in Sec. 5.2.3 is prepared as a solution 300ppm of polyacrylamide in a solvent composed of glycerol/water 80% . The viscosity of such a solution is shown in Fig. 5.1 as a function of the shear rate . The viscosity results practically constant with a value $\eta \sim 50mPas$ in a large range of shear rates. This value is very close to the viscosity of the solvent alone (see Table 5.1). It is reported in the literature that polyacrylamide solutions degrade over time[77], on a timescale of the order of weeks. The solution used in this work has been prepared the day right before the experiments, after which it was not reused again.

Liquid	$\boldsymbol{K}(mPas^n)$	$\boldsymbol{n}$
Xanthan/Water 400 ppm (w/w)	32.6	0.589
Xanthan/Water 800 ppm (w/w)	75.5	0.491
Xanthan/Water 1500 ppm (w/w)	312.5	0.389
Xanthan/Water 2500 ppm (w/w)	985	0.302

Table 5.2: Fitting parameters of the power-law fit of the xanthan solutions.

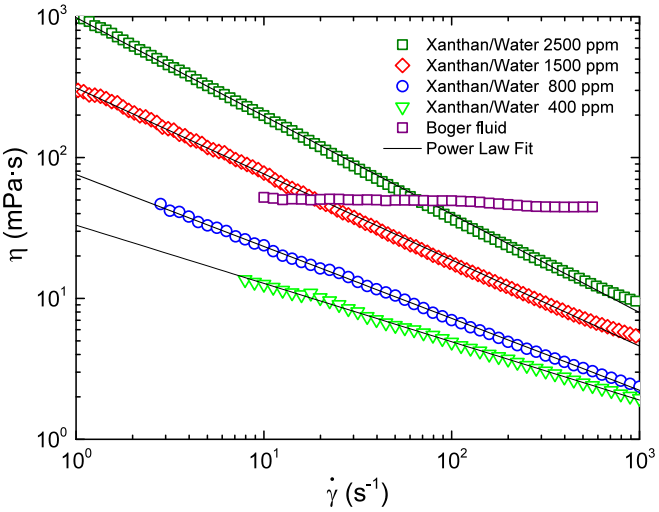

Figure 5.1: Shear viscosity as a function of the shear rate $\dot{\gamma}$ of the Xanthan solutions at different concentration (in p.p.m. w/w) and of the Boger fluid. For the Xanthan solutions, the experimental data are fitted according to the power fluid model (Eq. 5.1). The fitting parameters are reported in Table 5.2.

5.1.2 Experiments

Droplets are produced by merging two immiscible liquids in a microfluidic T-junction (Fig.5.2-A), which is composed of a main microchannel encountering perpendicularly a side channel, with the same cross section. The chips, with an overall size of 2 cm $\times 5$ cm and microchannels of width $W \sim 150\ \mu m$ and height $H \sim 100\ \mu m$, are made in PDMS using standard photo-softlithography. The fabrication process is described in detail in Sec. 3.3.2.

The dispersed phase forming the droplets is injected by the side channel with a flow-rate Q_d, while the continuous phase carrying away the droplets is injected in the main channel with a flow-rate Q_c, the flow-rates being controlled by a couple of syringe pumps. It is thus possible to obtain any value of the flow-rate ratio φ, defined as the ratio between Q_d and Q_c:

$$\varphi = \frac{Q_d}{Q_c}. \tag{5.2}$$

Images of the droplets are acquired and analyzed in real-time with a software, which also controls the syringe pumps. The length L of the droplets is measured, after breakup, in a region of interest downstream the T-junction (Fig.5.2-A), and is averaged over at least a hundred droplets. The experimental setup is described in more detail in Sec. 3.4.

5.1.3 Effective capillary number

The breakup process occurring in a microfluidic T-Junction is driven by the concurrent action of the shear stress exerted by the continuous phase on the dispersed phase and the interfacial tension. The ratio between these two forces defines the Capillary number [78, 25]:

$$\mathrm{Ca} = \frac{\eta_c U_{av}}{\sigma} \tag{5.3}$$

where the quantities U_{av} and η_c are the average velocity and the viscosity of the continuous phase, respectively, while σ is the interfacial tension. In the context of a shear thinning continuous phase, the viscosity is not a constant and thus the definition 5.3 cannot be used. The preliminary results of the droplet breakup experiments presented next (Sec. 5.2.2) suggest that, as a first approximation, a shear-thinning continuous phase behaves like a Newtonian one. Therefore, an effective Capillary number may be defined in terms of the actual viscosity $\eta_{eff}(Q_c)$ of the shear-thinning solution:

$$\mathrm{Ca}_{eff} = \frac{\eta_{eff}(Q_c) U_{av}}{\sigma} \tag{5.4}$$

The most obvious way of defining η_{eff} is by using the power law model of the fluid expressed in equation 5.1. Since η_{eff} depends only on Q_c, a particular value of the shear rate $\dot{\gamma}^*(Q_c)$ must be assumed to be the typical shear rate at that particular Q_c. One simple way of estimating such a shear rate is by considering a Newtonian fluid in a Poiseuille flow between two parallel walls, positioned in $y = 0$ and $y = W$:

$$u_x(y) = (\Delta P / 2\eta_c) y(W - y)$$

where $u_x(y)$ is the fluid velocity in the x direction, and ΔP is the applied pressure difference. In this flow, the fluid velocity is maximum in the middle of the walls, at $u_x(y = W/2) = u_{max}$. The typical shear rate may thus be simply estimated by:

$$\dot{\gamma}^* = \frac{u_{max}}{W/2} \tag{5.5}$$

which can be computed directly from the known flow rate $Q_c = U_{av}/WH$, since $U_{av} = 2\int_0^{W/2} u_x(y)\, dy/W = 2/3 u_{max}$, thus $\dot{\gamma}^* = 3U_{av}/W$. Another way of estimating the typical shear rate is by averaging $\dot{\gamma}$ over y:

$$\dot{\gamma}_{av} = \frac{2}{W}\int_0^{W/2} \dot{\gamma}\, dy = \frac{2}{W}\int_0^{W/2} \frac{\partial}{\partial y} u_x(y)\, dy = 3U_{av}/W \tag{5.6}$$

which, in the case of a Poiseuille flow, gives exactly the same expression as above, i.e. $\dot{\gamma}_{av} = \dot{\gamma}^*$. Once the shear rate is estimated, the corresponding effective viscosity can be computed by the power law model:

$$\eta_{eff} = K\, \dot{\gamma}^{\,(n-1)} \tag{5.7}$$

The definition of the effective Capillary number (5.4) takes into account the thinning behaviour of the continuous fluids, in that the viscosity is computed for a shear rate which is dependent on the driving velocity itself. However, the following simple dimensional argument suggests that further refinements, dependent on the thinning exponent, are required. Indeed, the motion of a viscous fluid results in the balance of the viscous forces with the pressure driven forces as $\boldsymbol{\nabla} \cdot (\eta_c(\dot{\gamma}) \boldsymbol{\nabla} \boldsymbol{u}) = \boldsymbol{\nabla} P$ or, equivalently,

$(\boldsymbol{\nabla}\eta_c(\dot{\gamma}))\cdot\boldsymbol{\nabla}\boldsymbol{u}+\eta_c(\dot{\gamma})\nabla^2\boldsymbol{u}=\boldsymbol{\nabla}P$. For a Newtonian fluid, $\boldsymbol{\nabla}\eta_c(\dot{\gamma})=0$, and the definition of Capillary number (5.3) is recovered from the usual balancing of $\eta_c\nabla^2\boldsymbol{u}$ and $\boldsymbol{\nabla}P$. In presence of thinning contributions, the term $(\boldsymbol{\nabla}\eta_c(\dot{\gamma}))\cdot\boldsymbol{\nabla}\boldsymbol{u}$ must be account for. A simple dimensional estimate gives $\boldsymbol{\nabla}\eta_c(\dot{\gamma})\approx\partial\eta_c/\partial\dot{\gamma}\,\nabla^2\boldsymbol{u}=(n-1)\frac{\eta_c(\dot{\gamma})}{\dot{\gamma}}\nabla^2\boldsymbol{u}$, hence $(\boldsymbol{\nabla}\eta_c(\dot{\gamma}))\cdot\boldsymbol{\nabla}\boldsymbol{u}\approx(n-1)\eta_c(\dot{\gamma})\boldsymbol{\nabla}^2\boldsymbol{u}$. Thus, by considering a small gradient expansion around $\dot{\gamma}\approx\dot{\gamma}_{av}$, the viscous contributions can be approximated as $\boldsymbol{\nabla}\cdot(\eta_c(\dot{\gamma})\boldsymbol{\nabla}\boldsymbol{u})\approx n\eta_c(\dot{\gamma}_{av})\nabla^2\boldsymbol{u}$. This argument suggests that a better description of the thinning effects is provided by the definition:

$$\overline{\mathrm{Ca}}=n\,\mathrm{Ca}_{eff}=n\left[\frac{\eta_{eff}(\dot{\gamma}_{av})U_{av}}{\sigma}\right] \tag{5.8}$$

n being the flow behaviour of the power-law fluid. This definition is used to rescale the data in section 5.3.

5.1.4 Numerical Simulations

The numerical simulations used to complement the experiments, which rely on lattice Boltzmann models (LBM), are carried out by Prof. Mauro Sbragaglia and Dr. Anupam Gupta. The numerical work falls in the continuity of their papers [79, 80, 81, 82, 83], where a Navier-Stokes description of the solvent based on LBM is coupled to constitutive equations for polymer dynamics. In two recent papers [79, 80], 3D simulations have been conducted to study the characteristic mechanisms of breakup in confined T-junctions [79] and cross-junctions [80], showing that elastic effects can sensibly perturb the flow driving the breakup process and influence the droplet dynamics and the resulting size after breakup.

The LBM code used in the following work is essentially the very same employed in [79, 80, 81], hence the interested reader is redirected to those papers where all the relevant technical details are discussed. At difference with respect to those previous studies, elastic effects are not included here, hence no explicit polymer dynamics is consider. Thinning effects are included by making the relaxation times in LBM dependent on the local shear properties, as explained in [84, 71]. The equations that are solved with the

Ca	φ	n
$0.001-0.1$	0.5	$1.0, 0.9, 0.8, 0.75, 0.7$
$0.001-0.1$	1.0	$1.0, 0.9, 0.8, 0.75, 0.7$

Table 5.3: Parameters for the numerical simulations with the T-junction geometry for thinning fluid.

LBM in the outer continuous (c) and dispersed (d) phases are the Navier-Stokes (NS) equations:

$$\rho_{c,d}\left[\partial_t\boldsymbol{u}_{c,d}+(\boldsymbol{u}_{c,d}\cdot\boldsymbol{\nabla})\boldsymbol{u}_{c,d}\right]=-\boldsymbol{\nabla}P_{c,d}+\boldsymbol{\nabla}\left(\eta_{c,d}(\boldsymbol{\nabla}\boldsymbol{u}_{c,d}+(\boldsymbol{\nabla}\boldsymbol{u}_{c,d})^T)\right). \tag{5.9}$$

In the above equations, $\boldsymbol{u}_{c,d}$ and $\eta_{c,d}$ are the velocity and the dynamic viscosity of the continuous and dispersed phase, respectively. The quantity $(\boldsymbol{\nabla}\boldsymbol{u}_{c,d})^T$ indicates the transpose of the velocity gradient tensor $(\boldsymbol{\nabla}\boldsymbol{u}_{c,d})=\partial_i u_{c,d;j}$. The (total) densities and bulk pressure are indicated with $\rho_{c,d}$ and $P_{c,d}$, respectively. In the continuous phase, the viscosity is chosen to be

$$\eta_c(\dot{\gamma})=\begin{cases}\eta_0+a\dot{\gamma}_0^{n-1} & \dot{\gamma}\le\dot{\gamma}_0\\ \eta_0+a\dot{\gamma}^{n-1} & \dot{\gamma}>\dot{\gamma}_0\end{cases} \tag{5.10}$$

where $a = 0.05$ (lbu, lattice Boltzmann units hereafter) and where the cut-off shear rate $\dot{\gamma}_0 = 10^{-5}$ lbu is introduced to prevent a divergence of the viscosity at small shear rates. The background viscosity $\eta_0 = 0.3$ lbu is chosen to avoid a zero viscosity in the high shear rate limit, which would cause numerical instabilities. For all practical purposes, in the range of shear rates relevant for the problem involved, the simulated fluid is a power-law fluid. In the dispersed phase, the viscosity is kept constant to $\eta_d = \eta_0 \approx 0.3$ lbu so that the viscosity ratio between the dispersed and the continuous phase ranges in the interval $[0.1 - 1]$ for the thinning exponents considered ($n \in [0.7 : 1.0]$). Larger thinning exponents are not easily handled in numerical simulations, due to the larger viscosity ratio associated with them. Table 5.3 summarizes all the parameters used in the numerical investigations for both Newtonian and non Newtonian phases.

5.2 Newtonian droplets in non-Newtonian continuous phases: preliminary results

5.2.1 Breakup regimes

The breakup regimes commonly reported with Newtonian liquids [85, 86, 78] are represented in the snapshots of Fig. 5.2a. In panel (A), droplets form at the junction and fill the channel. The dispersed phase completely obstructs the channel leading to an increase in the upstream pressure, which eventually breaks up the interface into a droplet. This regime is commonly called *squeezing* and the droplet size does not strongly depend on Ca, but only on the flow rate ratio [25, 78, 15, 87]. In panel (C) the droplets are emitted before they can block the channel and their formation is due to the action of the viscous shear stress. In this regime, called *dripping*, the droplet size decreases with Ca [14, 78, 15]. Finally, panel (E) shows that, at high Ca, the detachment point moves gradually downstream and the breakup process signals the emergence of the so-called *jetting* regime[78]. The snapshots (B) and (D) show the intermediate cases right before the transition to dripping and jetting, respectively.

The snapshots of Fig. 5.2b refer instead to oil droplets in a shear-thinning solution. They clearly show that, with suitable values of the flow rates, it is possible to reproduce the same regimes reported for the Newtonian systems. The same is true in the case of oil droplets produced in a Boger fluid, shown in Fig. 5.2c.

In particular, in the squeezing regime (panels A), there is no observable difference in the morphology of breakup and in the shape of the resulting droplet, with respect to the Newtonian. At higher flow rates, in the dripping (C) and jetting (E) regimes, while there is still no evident difference in the breakup morphology, the droplets shape results considerably deformed. With respect to the Newtonian, the droplets are elongated alogn the direction of the channel, the elongation being barely visible in the shear-thinning continuous phase and remarkable in the Boger fluid. This is a sign that, at higher flow rates, non-Newtonian effects in the flows are triggered. Whether these effects have an impact on the resulting droplets size can be evaluated only by a quantitative analysis.

5.2.2 Shear-thinning continuous phases

In the following experiments, Newtonian oil droplets are produced in both Newtonian and shear-thinning continuous phases, in the squeezing regime. Three acqueous solutions of xanthan are employed as shear-thinning continuous phases, at the concen-

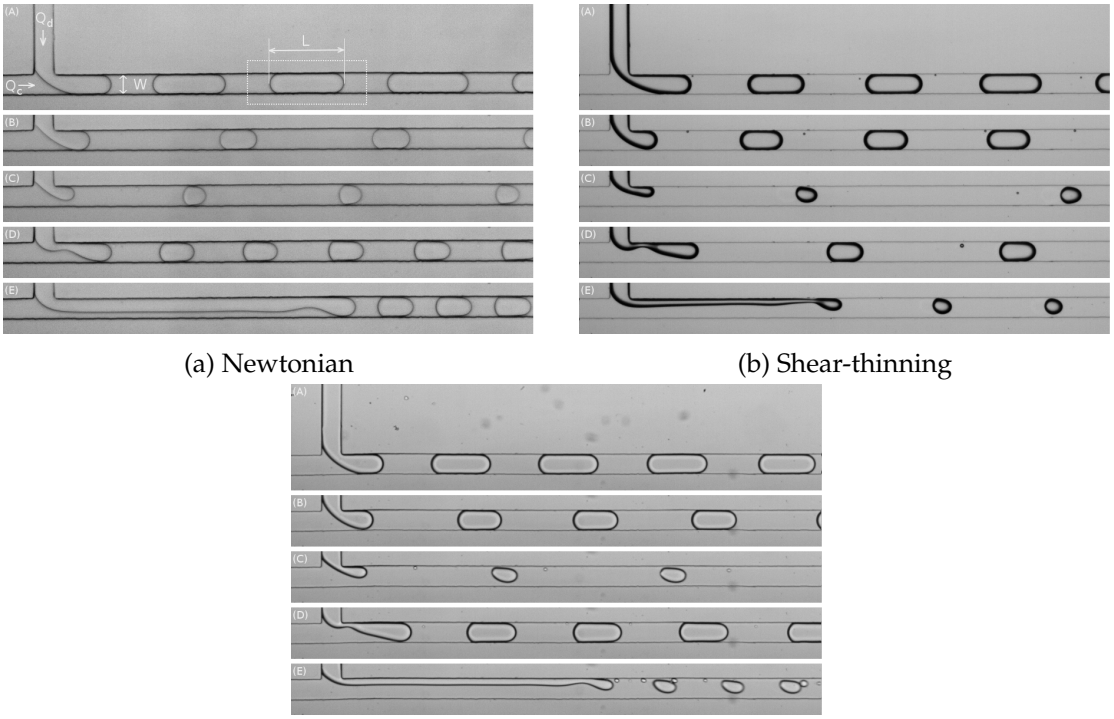

(a) Newtonian

(b) Shear-thinning

(c) Boger

Figure 5.2: Snapshots of droplets generation in the microfluidic T-Junction. Top left snapshot (A): the two inlets of the T-junction have the same width W and the same height H (not shown); the dispersed phase enters in the junction from the top with flow-rate Q_d, the continuous phase enters from the left side with flow-rate Q_c. The length L of the droplets is measured while they cross a rectangular region of interest (the dashed contour) positioned downstream of the T-Junction. Top left snapshots (A-E) report a breakup occurring in a Newtonian continuous phase (the system N3 is shown, see Table 5.5 for details) , top right snapshots report breakup occurring in a shear thinning continuous phase (the system XA400 is shown, see Table 5.6 for details). , bottom snapshots report breakup occurring in a Boger fluid continuous phase (see Table 5.4 for details). Droplets are formed in squeezing (A), dripping (C) or jetting (E) regimes. Snapshots (B) and (D) outline the emergent dripping and jetting regime, respectively.

tration of 800, 1500 and 2500 ppm (w/w). The rheologycal parameters are reported in Table 5.2. For the Newtonian continuous phases, pure water and aqueous solution of glycerol at 60% and 85% are employed. Linseed oil is used in all cases as the Newtonian dispersed phase. No surfactant is added to the liquids.

The glycerine concentrations are chosen in order to have comparable viscosities with respect to the xanthan solutions. In particular, the viscosity of 85% glycerol/water is similar to the viscosity exhibited by xanthan 800ppm at a shear rate of $1s^{-1}$, which is numerically equivalent to its consistency index K (compare Tables 5.2 and 5.1). The viscosities of 60% and 85% glycerol/water are then comparable to the viscosities of xanthan 800ppm and 2500ppm, respectively, in the middle of the range of shear rates shown in Fig.5.1. Linseed oil is used as dispersed phase because, as a vegetable oil, it has a large molecular size and therefore swelling of the PDMS is minimized.

The interfacial tensions between the liquids are measured with the pendant drop technique (see Sec.3.2). The interfacial tension σ between water and linseed oil is $10.1 \pm 0.6mN/m$ while $\sigma = 9.8 \pm 0.4mN/m$ between $85\%(w/w)$ glycerol/water and linseed oil, therefore σ between $60\%(w/w)$ glycerol/water and linseed oil is expected to be $\sim 10mN/m$. The surface tensions between the xanthan aqueous solutions and linseed oil are assumed to be the same as that between pure water and linseed oil due to the

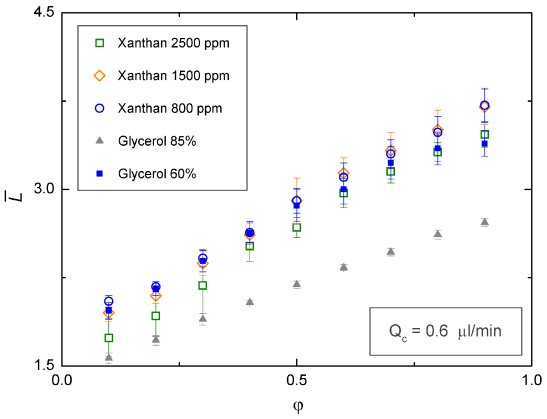

Figure 5.3: Dimensionless droplet length $\overline{L}$ as a function of the flow rate ratio φ for three xanthan solutions characterized by different rheologycal parameters (empty symbols). As a comparison, the data of the Newtonian solutions 60% (w/w) glycerol/water and 85% (w/w) glycerol/water are also plotted (full symbols). The data refer to a constant flow rate of the continuous phase $Q_c = 0.6\mu L/min$.

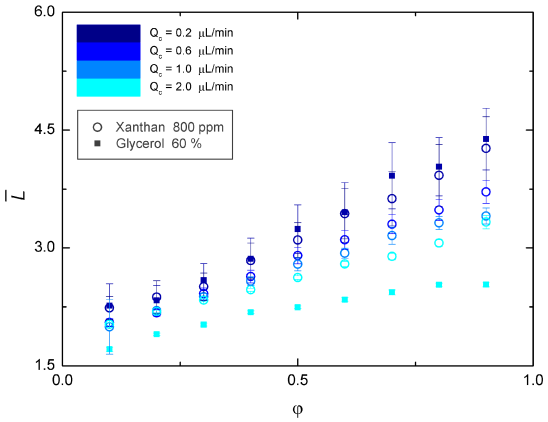

Figure 5.4: Dimensionless droplet length $\overline{L}$ as a function of the flow rate ratio for the xanthan 800 ppm solution (empty circles) for different values of Q_c (different colors). As a comparison, the data of the Newtonian solution 60% (w/w) glycerol/water is also plotted (full squares) for the lowest and the highest Q_c.

very low xanthan concentrations.

Accordingly, in the following experiments the only parameter that sensibly varies is the viscosity of the continuous phase, as the interfacial tension is practically the same for all combination of liquids. Figure 5.3 shows the variation of the average droplet lenght $\overline{L}$ as a function of the flow rate ratio φ at a fixed value of $Q_c = 0.6\mu L/min$, for all the solutions employed[88].

The droplet length in glycerol solutions increases linearly with the flow rate of the dispersed phase $Q_d = Q_c\varphi$ as expected [25, 53, 15]. Instead, increasing the viscosity of the continuous phase produces shorter droplets [89, 53, 15]. The lengths of oil droplets corresponding to $800ppm(w/w)$ xanthan/water are significantly longer, about 30%, than those obtained with the 85% glycerol solution. However, they are very similar to the oil droplet lengths formed in the 60% glycerol solution. Increasing the xanthan concentration to $1500ppm$ does not markedly affect the droplet length. A small decrease in $\overline{L}$, about 10%, is found at the highest xanthan concentration investigated, $2500ppm$. The data of Figure 5.3 suggest that the effective viscosity of the xanthan solutions when the T-junction is operating is much lower than the static one (i.e. the one at low shear rate $\dot{\gamma} = 1s^{-1}$). Given the good agreement with the data corresponding to the solution $60\%(w/w)$ glycerol/water, it is possible to estimate that, at $Q_c = 0.6\mu L/min$, the effective viscosity of the $800ppm$ xanthan solution amounts to about $10mPa \cdot s$, i.e. it has decreased by a factor of approximately eight, with respect to its consistency value (i.e. the viscosity measured at $\dot{\gamma} = 1s^{-1}$). This implies that the shear rates of this continuous phase during droplet breakup are on the order of $50s^{-1}$, as derived from the rheological data of Figure 5.1. Similar considerations hold for the other xanthan concentrations at different flow rates. For instance, if a much higher continuous flow rate is considered, $Q_c = 4\mu L/min$, the length of oil droplets in presence of the $800ppm$ xanthan solution is similar to that of oil in water. Therefore, the effective viscosity of the xanthan solution is now decreased by a factor ~ 80 and the corresponding shear rate increases to about $1000s^{-1}$. To complete the characterization of the droplet formation in a shear-thinning medium, Figure 5.4 shows the average length of oil droplets

as a function of the flow rate ratio of the $800ppm(w/w)$ xanthan/water solution for different values of flow rate Q_c[88]. As in Figure 5.3, the droplet length increases almost linearly with the dispersed flow rate $Q_d = Q_c\varphi$. Furthermore, $\overline{L}$ decreases with the increasing of the continuous flow rate, again in agreement with the general trend found in Newtonian fluids [25, 53, 15]. The data corresponding to $Q_c = 0.2\mu L/min$ practically coincide with those obtained with the $60\%(w/w)$ glycerol/water solution, confirming that also at this continuous flow rate the dynamic behavior of the $800ppm$ xanthan solution in the T-junction is very similar to that of the 60% glycerol solution. However, if the flow rate of the xanthan solution is increased to $Q_c = 2\mu L/min$, the droplets are $\sim 15\%$ longer than those obtained with the 60% glycerol solution at the same Q_c. Again, this difference can be explained in terms of a variation of the viscosity of the xanthan solution with the continuous flow rate.

5.2.3 Elastic continuous phases

The effects of elasticity on droplet breakup are investigated with a Boger fluid as continuous phase, composed of a solution of 300ppm polyacrylamide in 80% glycerol/water. This non-Newtonian fluid is characterized by non negligible normal stress differences, as well as a constant viscosity (see Sec. 5.1 for details). Thus, in principle, the comparison of the droplets breakup with respect to Newtonian fluids is straightforward, by employing a Newtonian fluid with the same viscosity. In particular, in the following experiment the solvent of the Boger fluid, i.e. glycerol/water 80%, is used as the Newtonian reference. Soybean oil is used as the dispersed phase in both cases. Table 5.4 reports the details of the Newtonian and the non-Newtonian systems.

Since the shape of the droplets is considerably affected by the flow, the droplet volume is measured instead of the length (see Sec. 3.4). Figure 5.5 shows the dependence of the droplet volume V as a function of the Capillary number Ca for both the Newtonian and the non-Newtonian systems, for different values of the flow rate ratio $\varphi = Q_d/Q_c$ in the squeezing (lower Ca) and dripping regimes (higher Ca). For each φ, the volume is reported only up to the emerging of the jetting regime. The data clearly show that, in the limits of the resolution of this experiment, the size of droplets produced in the Boger fluid practically coincides with the size of droplets produced in the Newtonian one.

System	**Dispersed Phase**	**Continuous Phase**	η_c	$\sigma(\mathbf{mN/m})$
Newtonian	Soybean Oil	Glycerol/Water 80% + 0.26% Tween 20	43	6.5 ± 0.5
Boger	Soybean Oil	PAA 300ppm + Glycerol/Water 80% + 0.2% Tween 20	~ 50	8.2 ± 0.9

Table 5.4: Experimental parameters of the Newtonian system (top) and the non-Newtonian system (bottom). All quantities refer to a temperature $T = 25^{\circ}C$. Concentrations are expressed in terms of weight/weight ratio.

5.2.4 Summary

From this preliminary study results that the droplets breakup process both in a Boger fluid and in a shear thinning continuous phase is very similar to the one in Newtonian continuous phase. In the limits of the range of flow rates investigated, the size of droplets produced in the Boger fluid considered in this study is the same as the one

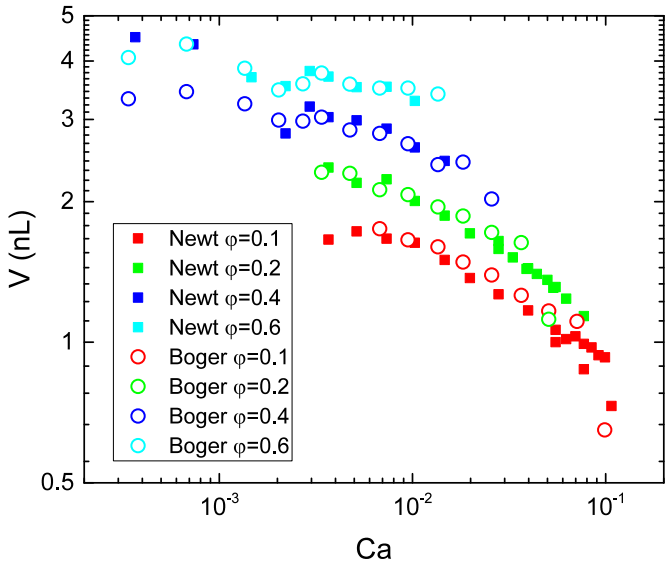

Figure 5.5: Volume of oil droplets produced in a Newtonian (full squares) and in a Boger fluid (empty circles) continuous phases, as a function of the capillary number Ca for different values of the flow rate ratio φ (different colors)

of droplets produced in the corresponding Newtonian liquid, at the same Capillary number Ca and flow rate ratio φ.

From the experiments with shear-thinning fluids results that, for a fixed value of Q_c, the droplets size in shear-thinning solution can be closely matched to the one in a particular Newtonian solution of some viscosity η_1, independently of the flow rate ratio φ. For a higher (fixed) value of Q_c, again the shear-thinning solution can be matched to another Newtonian solution, which has a different, lower viscosity η_2. It follows that, as a first order approximation, during the operation of the T-junction a shear-thinning solution can be well approximated as a Newtonian liquid, with an effective viscosity which is a function only of the continuous flow rate $\eta_{eff} = \eta(Q_c)$.

This fact suggests that it is possible to define an effective Capillary number which can be used to compare the droplets production in shear-thinning and Newtonian continuous phases. A definition of such an effective Capillary number is proposed in Sec. 5.1.3, and its validity is explored in a more systematic study with shear-thinning solutions in Sec. 5.3.

5.3 Newtonian droplets in shear-thinning continuous phases: systematic experiments

The experiments in this section address the generation of droplets both in Newtonian continuous phases (Newtonian system) and in shear thinning continuous phases made of polymer solutions (non-Newtonian system), keeping a Newtonian dispersed phase. Table 5.5 summarizes the parameters of the Newtonian systems, reporting the liquids composition, dynamic viscosity η_d of the dispersed phase, dynamic viscosity η_c of the continuous phase, viscosity ratio λ and interfacial tension σ. The viscosity ratio is defined as the ratio between the dynamic viscosity of the dispersed phase and the one of the continuous phase:

$$\lambda = \frac{\eta_d}{\eta_c} \tag{5.11}$$

ID	Dispersed Phase	Newtonian Continuous Phase	$\lambda = \eta_d/\eta_c$	$\sigma(\mathbf{mN/m})$
N1	Soybean Oil	Water + 0.50% Triton X-100	~ 50	2.55 ± 0.03
N2	Soybean Oil	Glycerol/Water 60% + 0.56% Triton X-100	~ 5	3.59 ± 0.27
N3	Glycerol/Water 67%	Hexadecane + 1% Span 80	~ 5	3.99 ± 0.11
N4	Glycerol/Water 40%	Hexadecane + 1% Span 80	~ 1	4.17 ± 0.03
N5	Water	Hexadecane + 1% Span 80	0.3	5.01 ± 0.15

Table 5.5: Experimental parameters of the liquids of the Newtonian systems. All quantities refer to a temperature $T = 25°C$. Surfactants and Glycerol concentration are expressed in terms of weight/weight ratio.

The Newtonian experiments span two decades of λ using various combinations of either Soybean oil (Alfa Aesar) or Hexadecane (Sigma Aldrich), and water solutions of Glycerol ($\geq$ 99.5% anhydrous, Sigma Aldrich) at different concentrations. A surfactant is added to the continuous phase in order to improve the wetting of the channel walls. Triton X-100 (Sigma Aldrich) is used in the water solutions while Span 80 (Sigma Aldrich) is added to Hexadecane. The values of the interfacial tension σ are measured with the pendant drop technique (see Sec.3.2). The non-Newtonian systems

ID	Dispersed Phase	Shear Thinning Continuous Phase	$\sigma(\mathbf{mN/m})$
X400	Soybean Oil	Xanthan 400 ppm + 0.2% Triton X-100	3.42 ± 0.01
X800	Soybean Oil	Xanthan 800 ppm + 0.2% Triton X-100	3.00 ± 0.04
X1500	Soybean Oil	Xanthan 1500 ppm + 0.7% Triton X-100	2.28 ± 0.02

Table 5.6: Experimental parameters of the liquids of the non-Newtonian systems. All quantities refer to a temperature $T = 25°C$. The concentrations are expressed in terms of weight/weight ratio.

are summarized in Table 5.6. Soybean oil is used as the dispersed phase while, as continuous phase, water solutions of Xanthan (molecular weight $M_w \simeq 10^6$ g/mol, Sigma Aldrich) at different concentrations are employed. The concentration of polymers is chosen to ensure that the rheological response of the continuous phase is dominated by shear thinning rather than viscoelasticity. At the highest concentration, the appearance of elastic effects due to the presence of first normal stress differences has been reported [71, 72].

Droplets generation in non-Newtonian systems will be compared to that in Newtonian systems in terms of the droplet size as a function of the flow rates. The comparison is made in similar conditions, such that the forces involved in the breakup process are the same. Therefore, a systematic investigation of the breakup is initially required, in order to characterize the Newtonian and non-Newtonian systems and to find a suitable range of flow rates where they can be safely compared.

5.3.1 Breakup Maps

The preliminary study in section 5.2 showed that the droplets breakup in a shear-thinning continuous phase is completely analogous to the one in Newtonian continuous phases, occurring in one of the regimes described in section 5.2.1, i.e. squeezing, dripping or jetting.

In Fig. 5.6, for each of the Newtonian and non-Newtonian systems investigated, a corresponding "phase diagram" is shown, reporting whether the breakup occurs in squeezing (S), dripping (D) or jetting (J) as a function of the flow-rate Q_c of the continuous phase and the flow rate ratio $\varphi = Q_d/Q_c$, . Panels (A-E) refer to the Newtonian liq-

uids whose details are listed in Table 5.5, while panels (G-I) correspond to the droplets formed in shear thinning continuous phases described in Table 5.6.

The data refer only to values of φ and Q_c for which droplet formation is stable and occurs at the T-junction. For each φ, the data stops at a certain value Q_c, which represents either the maximum Q_c for which droplet breakup still occurs before the detection window (see Fig. 5.2), or the maximum Q_c reachable by the setup (see Sec. 3.4 for details). Production at other φ and Q_c are either not stable (low φ, Q_c) or are not investigated.

The transition to jetting is characterized by particular values ${Q_c}^*$ of the continuous flow rate which depend on φ. These are identified by analyzing the evolution of droplet breakup, at fixed φ and increasing Q_c, as shown in panel (F). The left and right snapshots refer, respectively, to the instant just before and just after breakup for a typical sequence. At low Q_c the breakup takes place at the corner of the T-junction and after the droplet detachment the tip of the dispersed phase returns back into the side channel (1). At higher Q_c the breakup starts to take place after the corner and the tip returns back stopping at the level of the corner of the T-Junction (3) and then oversteps it (4) persisting in the main channel. At even larger Q_c the dispersed phase starts to jet (6). As the transition is continuous over a range of Q_c, the delimiting value ${Q_c}^*$ is chosen to be the one at which, just after breakup, the tip of the dispersed phase oversteps the corner of the T-junction, as indicated in the figure.

The transition to jetting displays approximately a power-law behaviour with $\varphi \sim {Q_c}^{-1}$, corresponding to a constant value of Q_d, as reported in the literature [63]. Further, as other authors report [90], hysteresis has been observed in the transition to jetting, i.e. after reaching the full jetting regime (Fig. 5.2-E) by increasing Q_c, the jet persists even after decreasing Q_c. For the Newtonian systems (A-E), the breakup maps are observed to vary strongly between different combination of Newtonian liquids. Overall, as λ decreases the transition is shifted to higher Q_c. In particular, for the lowest $\lambda \sim 0.3$ (Fig. 5.6-E) the transition to jetting is observed at Q_c higher than the ones accessible by the acquisition system, and thus can not be measured accurately.

5.3.2 Droplet size

Figure 5.7 shows the dependence of the dimensionless average droplet length L/W as a function of the flow-rate Q_c and of the Capillary number Ca (for the Newtonian systems) of the continuous phase, at different flow-rate ratios $\varphi = Q_d/Q_c$, for the same systems analyzed in Fig. 5.6. The empty circles overlying the curves mark the flow-rate Q_c^* corresponding to the onset of the jetting regime, described in the previous section.

Newtonian droplets in a Newtonian continuous phase

For the Newtonian systems, the droplet size is observed to increase at increasing φ, and decrease at increasing Ca [25, 15]. This trend is consistent with previous studies performed in similar conditions [15, 87]. For instance, at small Ca, the droplet size is independent of the viscosity ratio (see, for instance, the data at $\varphi = 0.4$ in Fig. 5.7 B-E) and increases with the flow-rate ratio (compare, for instance, the data at $\varphi = 0.4$ and $\varphi = 0.6$ in Fig. 5.7 B-E), in agreement with the scaling argument valid for the squeezing regime [25]. Furthermore, the change in the slope found at Ca $\simeq 10^{-2}$ for the curve $\varphi = 0.2$ and $\lambda = 1$ in Fig. 5.7-D (see dashed line) is very close to the transition from squeezing to dripping calculated in phase-field numerical simulations of immiscible fluids at Ca ≈ 0.015 for $\varphi = 0.25$ and $\lambda = 1$ [78].

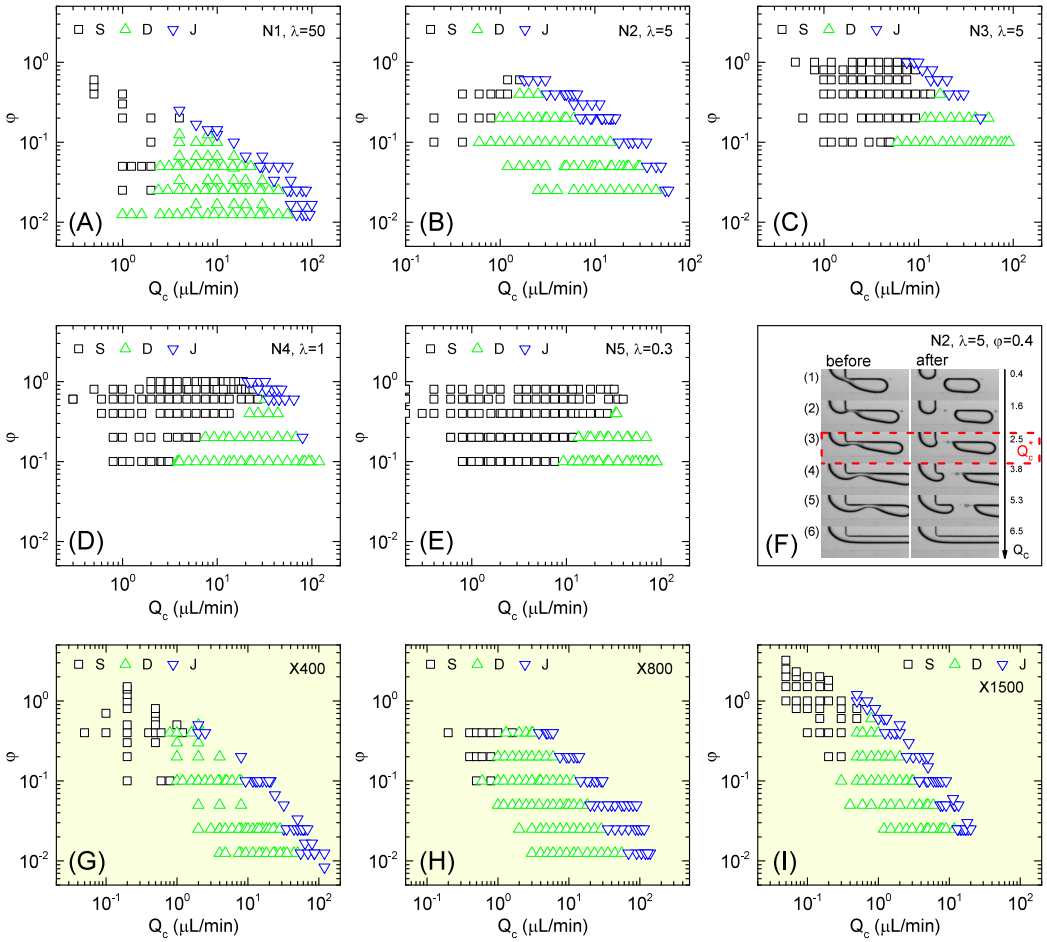

Figure 5.6: Panels (A)-(E) show the breakup maps of the Newtonian systems for all the combination of φ and Q_c investigated, reporting whether the breakup occurs in squeezing (S), dripping (D) or jetting (J). Similarly, panels (G)-(I) report the breakup maps for the non-Newtonian systems. Close to the transition to jetting, the data are marked as jetting when, at a fixed φ, the value of $Q_c \geq Q_c^*$. The value Q_c^* of the continuous flow rate corresponding to the transition to the jetting regime is described in the snapshots in panel (F). The left and right snapshots correspond to the time just before and just after breakup, respectively, at a fixed φ and increasing Q_c (from top to bottom) for a typical experiment (N2, $\varphi = 0.4$ is shown). The value of Q_c^* is chosen to be the minimum Q_c at which, just after breakup, the tip of the dispersed phase remains inside the main channel, as indicated in the snapshots. Panel (E) does not report the jetting, as the corresponding flow rates are out the reach of the experimental setup.

Figure 5.8 summarizes the data of the panels (C,D,E) concerning with only the squeezing and dripping regimes, showing the droplet size as a function of the capillary number.

In the squeezing regime, i.e. for Ca $\lesssim 0.01$, the length of the droplets can be conveniently expressed with the following scaling equation:

$$L = \alpha_1 + \alpha_2 \frac{Q_d}{Q_c} \tag{5.12}$$

where α_1 and α_2 are two constants of order one that depend on the junction geometry [25, 53, 91]. Accordingly, L should not depend on Ca if φ is constant. Instead, the measurements show no sign of approaching a constant value as the capillary number decreases, in the limits of the investigated range. It is found that the droplet length exhibits a power-law dependence on the capillary number $L \propto \mathrm{Ca}^{\beta}$, in good agreement

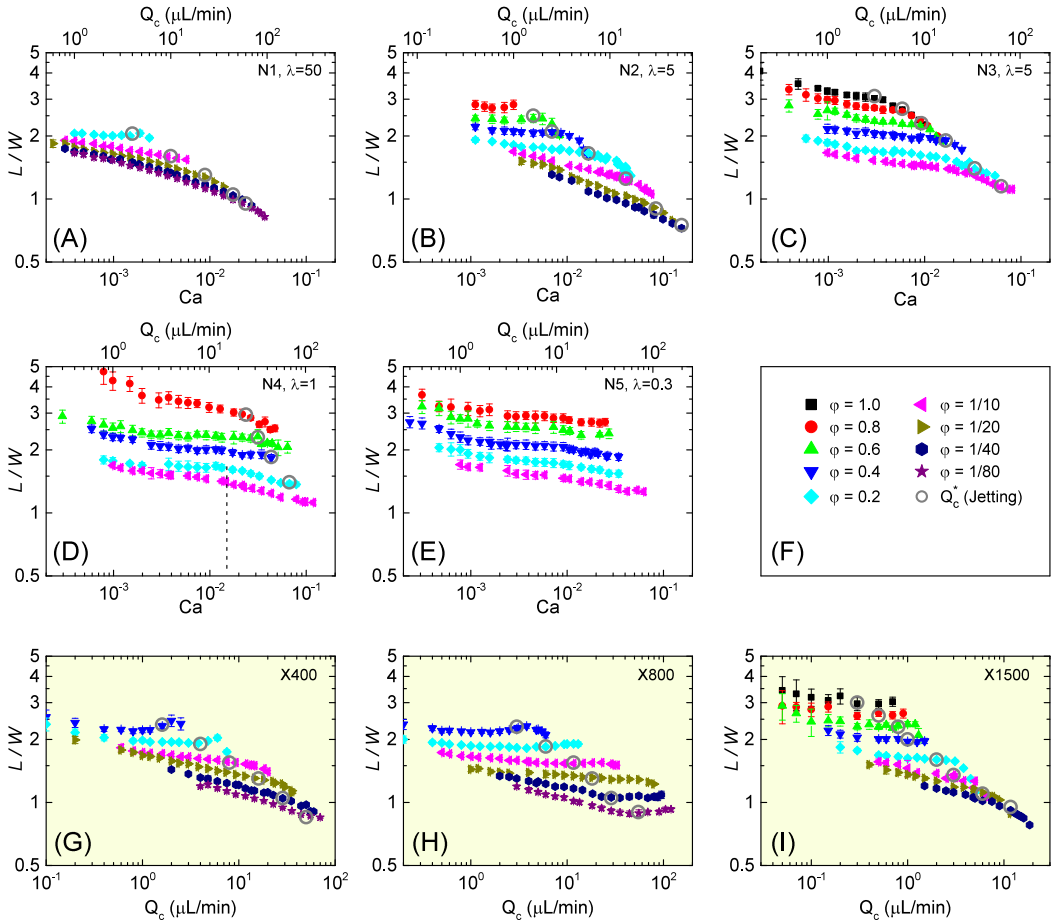

Figure 5.7: Normalized, dimensionless length L/W of the droplets formed at the microfluidic T-junction as a function of either the flow-rate of the continuous phase Q_c (top axis of panels (A-E), bottom axis of panels (G-I)) or the corresponding Capillary number Ca (bottom axis in panels (A)-(E)) for different values of the flow-rate ratio φ, indicated by different symbols according to the legend reported in Panel (F). Panels (A-E) refer to the Newtonian fluids listed in Table 5.5, while Panels (G-I) correspond to the polymers listed in Table 5.6. Open circles mark the flow-rate Q_c^* corresponding to the onset of the jetting regime.

with numerical results [78] and other experiments [15]. More interestingly, the data are found to scale according to the formula $L = k\varphi^{\alpha}\mathrm{Ca}^{\beta}$, where k is a constant whose value depends on the geometry of the T-junction [53]. The right plot of Figure 5.8 shows the dimensionless droplet length, L/W, normalized to $\varphi^{0.3}$ as a function of the capillary number of the continuous phase Ca. It is evident that the normalized droplet lengths nicely collapse on a straight line. The resulting scaling exponents are in good agreement with those originally found in similar conditions by Xu *et al.* in a narrower Ca range [53], who reported $\alpha = 1/3$ and $\beta = -0.2$.

Newtonian droplets in a shear-thinning continuous phase

For droplets carried by shear thinning liquids, the droplet size is observed to increase with φ and to decrease with increasing Q_c, just like the Newtonian counterparts. However, the size of the droplets produced in Xanthan solutions appears to increase at high Q_c. A more accurate analysis of the images reveals that droplets volume actually decreases with increasing Q_c and the increase of the droplet size at high Q_c (Fig. 5.7-A,B)

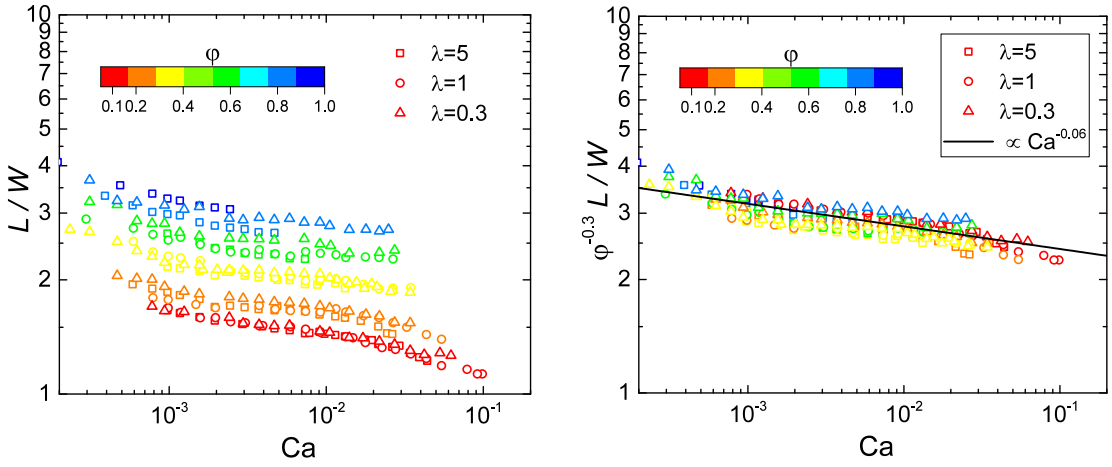

Figure 5.8: *Left*: Dimensionless droplet length as a function of the capillary number Ca, for the three Newtonian systems N3 (squares), N4 (circles), N5 (triangles), characterized by different viscosity ratios $\lambda = \eta_d/\eta_c$. The colors refer to different flow rate ratios $\varphi = Q_d/Q_c$. *Right*: The same data is normalized to $\varphi^{0.3}$. The line corresponds to the power law $\mathrm{Ca}^{-0.06}$

has to be ascribed to an elongation of the droplet as it is transported along the main channel (Fig.5.2-H). It is noteworthy that such elongation takes place when the shear forces appear to be quite consistent, and noticeably in the emergence of the jetting regime. Apart from this elongation, the droplet production in shear thinning continuous phases is qualitatively similar to that occurring in purely Newtonian systems. A quantitative comparison between Newtonian and non-Newtonian systems is then performed for selected values of the viscosity ratio λ, and of the flow-rate ratio φ.

In the left column of Fig.5.9 the average normalized droplet length L/W is reported as a function of the continuous flow-rate Q_c for selected φ, covering more than one decade, from $\varphi = 1/40$ to $\varphi = 0.4$. Data taken at $Q_c \lesssim 0.1\ \mu L/\mathrm{min}$ are discarded due to poor reproducibility of our syringe pumps in this range. Similarly, droplets formed in the jetting regime are not considered because of elongation effects. The graphs clearly show that the droplets formed in the shear thinning Xanthan solutions get smaller as the Xanthan concentration is increased, at a given φ. In addition, the size difference between droplets carried by Xanthan at 1500 ppm and the ones formed in water is about 30% for about one decade of φ. However, when plotted against the effective Capillary number $\overline{\mathrm{Ca}}$ defined in Sec. 5.1.3, a remarkable degree of collapse on the same curve is observed for all the data. With such rescaling, the droplets produced at a given φ display essentially the same size either they are formed in Newtonian or non-Newtonian, shear thinning, continuous phases. This provides a direct, experimental evidence of the validity of the $\overline{\mathrm{Ca}}$ number to capture the shear distribution inside the microfluidic channel when a shear thinning fluid is flowing at a given Q_c. To better understand the role played by the Xanthan solutions, the droplet breakup experiments are complemented with realistic numerical simulations.

5.4 Numerical Results

Initially, the LBM simulations are compared to experiments performed with pure Newtonian fluids. The results are reported in Fig. 5.10. Specifically, in panels (A-H) a representative case is reported, corresponding to $\mathrm{Ca} = 0.0085$, $\varphi = 0.4$ and $\lambda = 1.0$, where the system is transiting from the squeezing dominated regime to the dripping

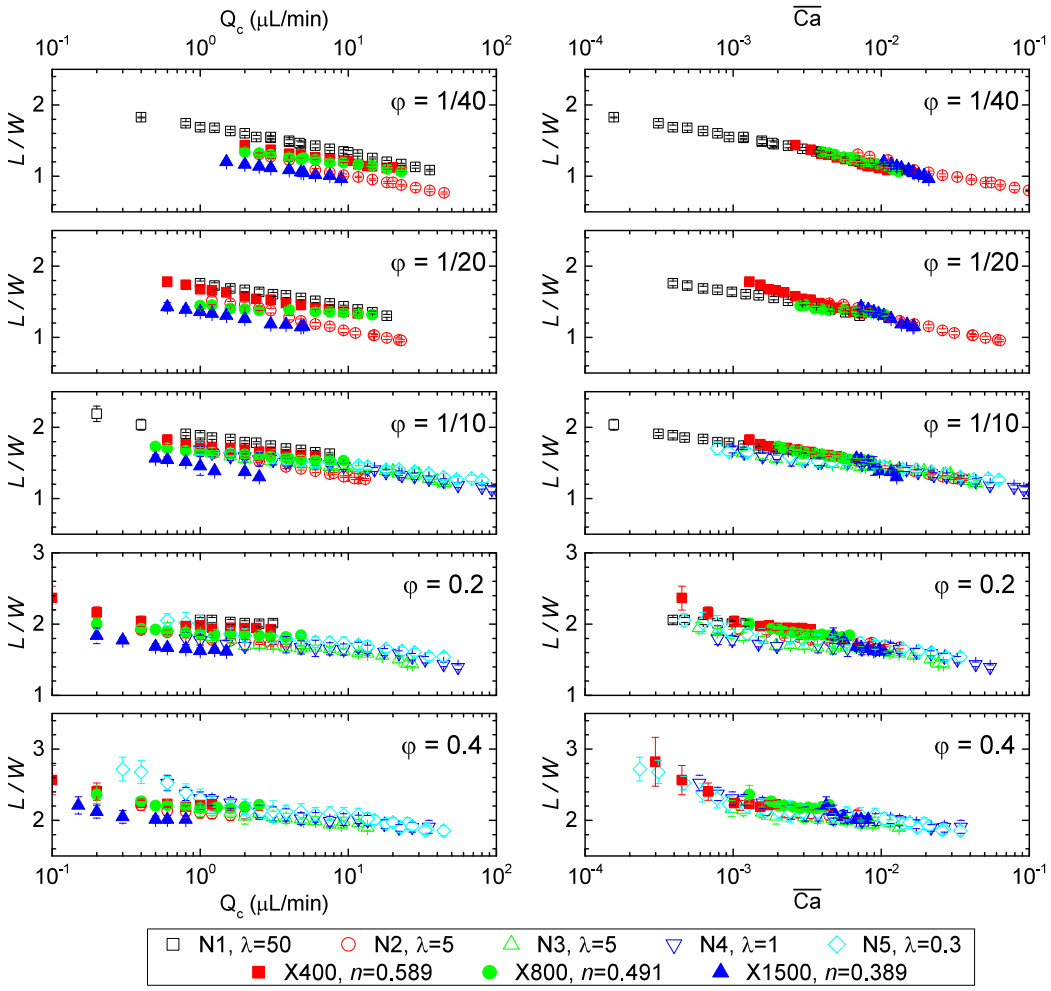

Figure 5.9: Experimental normalized droplet length L/W as a function of the flow-rate of the continuous phase Q_c (left column) and the effective Capillary number $\overline{\text{Ca}}$ defined in Eq. 5.4 (right column), for different values of the flow-rate ratio φ, which is increasing from top to bottom rows. Empty symbols refer to Newtonian fluids, full symbols to shear-thinning Xanthan solutions at different concentrations.

regime. The experiments and numerical simulations are compared using the characteristic shear time $\tau_{\text{shear}} = W/U_{av}$ as a unit of time.

More quantitatively, for a fixed φ, the droplet size is a decreasing function of Ca (see Panel (I)); moreover, for a fixed Ca, a linear scaling law for the droplet size as a function of φ is reproduced (see inset). For capillary numbers Ca $\approx (10^{-2})$ the droplet size is in good agreement with the experimental results, while a slight mismatch emerges at higher Ca [92, 93], in the jetting regime, which is however not of interest for the present study. Overall, the simulations of Newtonian fluids retain the key relevant outcomes of the experiments, in terms of droplet size behaviour as a function of Ca and φ. Hence, with respect to the reference Newtonian case, they are good candidates to explore quantitatively the effects induced by the non-Newtonian behaviour as well as the validity of the suggested rescaling in terms of Ca, n and φ.

Fig. 5.12 shows the effect of thinning phases on the droplet size for a fixed flow-rate Q_c. The simulations refer to a representative case with $Q_c = 1.23$ lbu (lattice

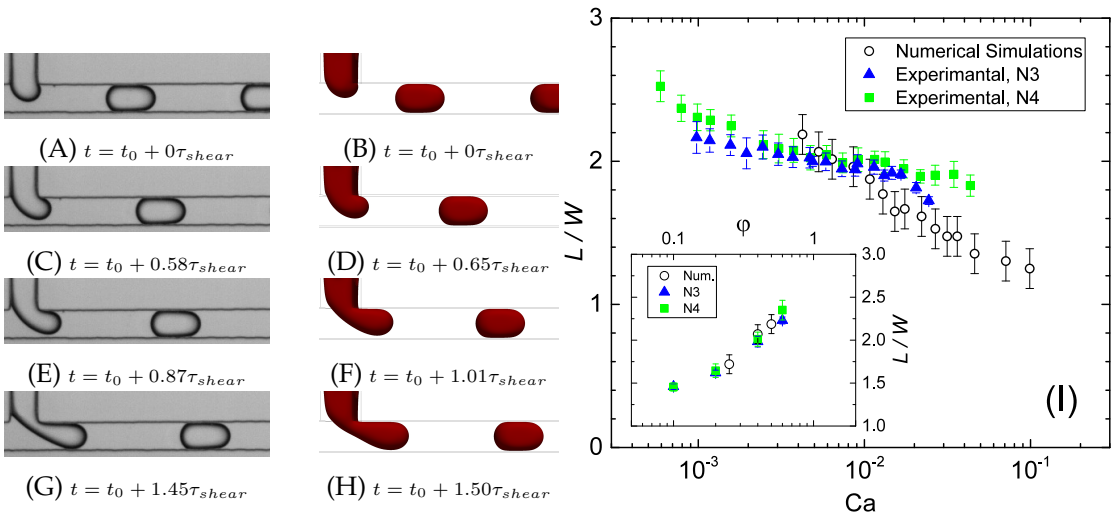

Figure 5.10: *Left*: panels (A-H) show the time dynamics for the droplet formation process close to the squeezing-to-dripping transition from experiments (left snapshots) and LBM simulations (right snapshots) for Ca $= 0.0085$, $\varphi = 0.4$ and $\lambda = 1.0$. Time is made dimensionless using the shear time $\tau_{shear} = W/U_{av}$. *Right*: quantitative comparison between the numerical simulations and the experiments (N3 and N4 are shown, see Table 5.5) of the normalized droplet size as a function of the Capillary number. The inset reports data for a fixed Capillary number Ca ≈ 0.008 as a function of the flow rate ratio φ.

Boltzmann units), viscosity ratio $\lambda = 1.0$ and flow-rate ratio $\varphi = 0.5$. Both Newtonian ($n = 1$, snapshots (A-B)) and non-Newtonian ($n = 0.9$ snapshots (C-D), $n = 0.7$ snapshots (E-F)) cases are considered. For the non-Newtonian fluids the droplet size is observed to be smaller in comparison to the Newtonian case, and the effect is more pronounced at decreasing thinning exponents. This is in the same trend as the experimental findings reported in the left panel of Fig. 5.9. At the microscales of the present experiments, the non-Newtonian LBM contain essentially the same information as the hydrodynamic NS equations supplemented with shear thinning bulk rheology Eq. 5.1 (see also Sec.5.1.4), hence they strongly corroborate the idea that the observed results originate from a combination of hydrodynamics and bulk thinning phases.

To further support this idea, the viscous stress in the continuous phases is computed along a slice located at half of the channel height. This is overlaid on the density contours in Fig. 5.12. Indeed the viscous stress is more intense close to the boundaries at decreasing n. This explains the observed discrepancies in droplet sizes, in that whenever a larger viscous stress is present close to the wall, this results in a smaller droplet size.

To complement the results reported in Fig. 5.9, numerical data for the normalized droplet length at changing Ca, φ and n are reported in Fig. 5.11. The overall picture emerging from Fig. 5.9 and Fig. 5.11 highlights that the proposed rescaling arguments work well for a wide range of thinning fluids ($n = 0.5 - 1.0$) and flow-rate ratios ($\varphi = 1/40 - 1.0$). Overall, whenever weak discrepancies emerge, they are of the same order of magnitude for both experiments and numerical simulations; since numerical simulations are performed with purely thinning fluids, it is unlikely to attribute such discrepancies to the weak normal stresses of Xanthan [71, 72].

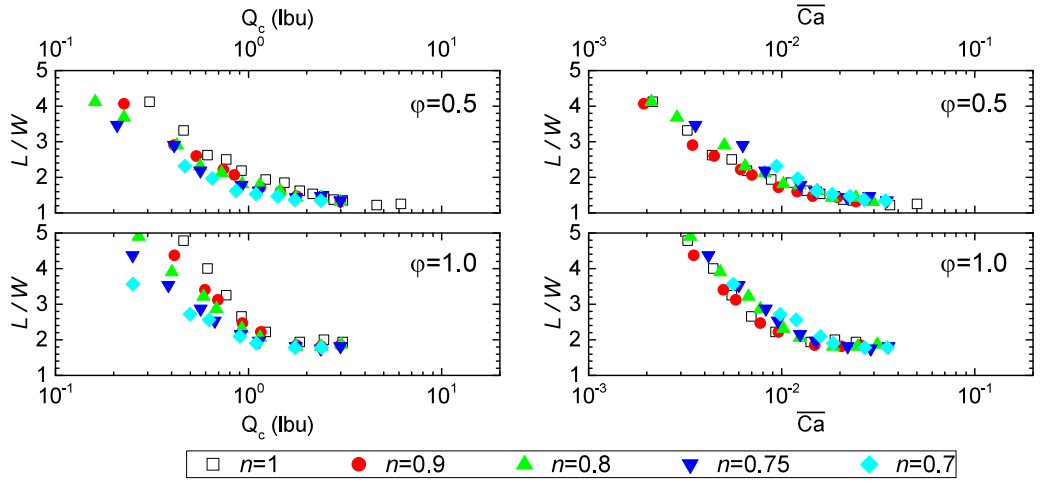

Figure 5.11: Numerical normalized droplet length L/W as a function of the flow-rate of the continuous phase Q_c (left column) and the effective Capillary number $\overline{\text{Ca}}$ defined in Eq. 5.4 (right column), for different values of the flow-rate ratio φ, which is increasing from top to bottom rows. Open symbols refer to Newtonian fluids, full symbols refer to power-law fluids with different flow behaviour indexes n.

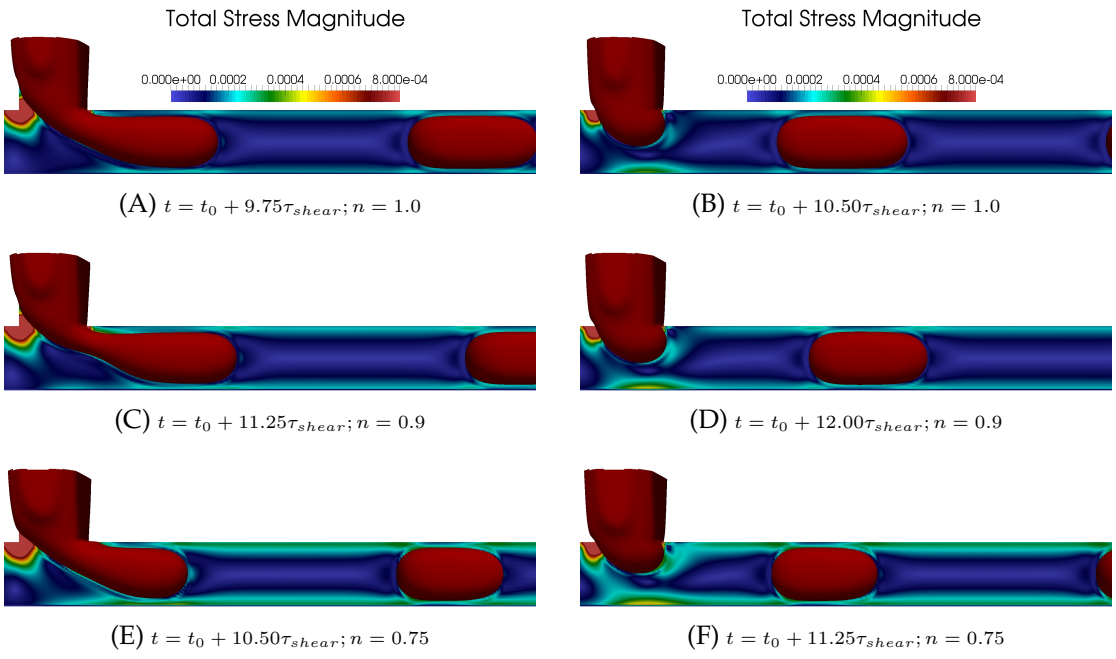

(A) $t = t_0 + 9.75\tau_{shear}; n = 1.0$ (B) $t = t_0 + 10.50\tau_{shear}; n = 1.0$

(C) $t = t_0 + 11.25\tau_{shear}; n = 0.9$ (D) $t = t_0 + 12.00\tau_{shear}; n = 0.9$

(E) $t = t_0 + 10.50\tau_{shear}; n = 0.75$ (F) $t = t_0 + 11.25\tau_{shear}; n = 0.75$

Figure 5.12: Snapshots of droplet formation process in numerical simulations with LBM, reporting two representative situations before (left column) and after (right column) the breakup process has occurred. 3D snapshots are overlaid on the viscous stress in the continuous phases computed along a slice located at half of the channel height. The flow-rate ratio is kept fixed to $\varphi = 0.5$ and the flow-rate in the continuous phase to $Q_c = 1.23$ lbu. Different power-law exponents are used: Newtonian fluid ($n = 1$, snapshots A-B), thinning fluid with thinning exponent $n = 0.9$ (snapshots C-D) and $n = 0.75$ (snapshots E-F).

5.5 Conclusion

The droplets breakup in a microfluidic T-junction driven by either Newtonian or non-Newtonian continuous phases has been extensively studied. The droplets size has been measured over a wide range of the viscosity ratio λ and flow-rate ratio φ still partly unexplored [78] [94] [15]. Squeezing, dripping and jetting regimes are identified for Newtonian and non-Newtonian continuous phases and the resulting breakup maps look quite similar.

The size of droplets produced in a Boger fluid is observed to be the same as the one of droplets produced in a Newtonian liquid with the same viscosity and at the same Capillary number Ca and flow rate ratio φ. Despite the droplets are considerably deformed as they are carried away by the Boger fluid, there is no strong evidence that the elasticity of the continuous phase affects the droplet size resulting after breakup.

The size of droplets produced in shear-thinning solutions in the squeezing and dripping regimes is found to nicely scale with an effective Capillary number, which reduces to the usual Capillary number when the fluid is Newtonian. The experiments are complemented with numerical simulations based on lattice Boltzmann models (LBM) with purely thinning fluids. The simulations show that for the same injection flow-rate, the viscous stress is more intense close to the microchannel walls for a shear-thinning fluid, thus yielding smaller droplets as observed in the experiments. The rescaling with the effective Capillary number is also verified in numerical simulations, thus confirming that the observed properties are solely ascribed to a combination of continuum hydrodynamics and purely thinning phases. These results provide new insights into the formation and the manipulation of droplets in the presence of non-Newtonian confined environments and show that LBM can be successfully employed for the simulation of such complex microfluidic systems.

Conclusions

The study of breakup dynamics of droplets formed in non-Newtonian fluids is important for the applicability of droplet microfluidic devices in many reseach fields, which often involve non-Newtonian fluids. Moreover, the development of microfabrication techniques which are simple and involve cheap materials is an important aspect for the widespread diffusion of microfluidics as a viable research tool.

This thesis describes how T-junction microfluidic devices can be constructed in polyester-toner technology, using common office equipment. These devices have been demostrated to be suitable for generating highly monodisperse water-in-oil and oil-in-water droplets in the same device without any specific surface treatment of the channels walls. This is mainly due to the partial hydrophilicity of the polyester surface together with the addition of suitable surfactants. The fabrication procedure is characterized by being very simple, fast and inexpensive, being possible to complete the whole fabrication in less than 10 min, with a cost of $\sim \$0.10$ per device.

It also presents the systematic results of droplets breakup in a microfluidic T-junction driven by either Newtonian or non-Newtonian continuous phases. The droplets size has been measured over a wide range of the viscosity ratio and flow-rate ratio. Squeezing, dripping and jetting regimes are identified for Newtonian and non-Newtonian continuous phases and the resulting breakup maps look quite similar.

The size of droplets produced in a Boger fluid is observed to be the same as the one of droplets produced in a Newtonian liquid with the same viscosity and at the same Capillary number and flow rate ratio. Despite the droplets are considerably deformed as they are carried away by the Boger fluid, there is no strong evidence that the elasticity of the continuous phase affects the droplet size resulting after breakup. However, further experiments may be done in the future using different viscoelastic fluids, which exhibit stronger elastic responses.

The size of droplets produced in shear-thinning solutions in the squeezing and dripping regimes is found to nicely scale with an effective Capillary number, which reduces to the usual Capillary number when the fluid is Newtonian. The experiments are complemented with numerical simulations based on lattice Boltzmann models (LBM) with purely thinning fluids. The simulations show that for the same injection flow-rate, the viscous stress is more intense close to the microchannel walls for a shear-thinning fluid, thus yielding smaller droplets as observed in the experiments. The rescaling with the effective Capillary number is also verified in numerical simulations, thus confirming that the observed properties are solely ascribed to a combination of continuum hydrodynamics and purely thinning phases. These results provide new insights into the formation and the manipulation of droplets in the presence of non-Newtonian confined environments and show that LBM can be successfully employed for the simulation of such complex microfluidic systems.

Appendix A

Lattice Boltzmann Method

In this chapter the main concepts underlying the Lattice Boltzman Method are introduced. The general structure of this chapter is adapted from[95]. In section A.1 the Boltzmann equation, which describes a fluid at the microscopic scale, is introduced. Starting from that, in section A.2, the well known Navier-Stokes equations are recovered, which describe the fluid at the macroscopic scale. The Lattice Boltzmann Method is presented in section A.3. Section A.4 shows how the interfacial tension can be implemented.

A.1 Boltzmann equation

The microscopic description of a dilute gas composed of particles of equal mass m[1] can be accomplished by a distribution function in the phase-space. $f \equiv f(\boldsymbol{x}, \boldsymbol{v}, t)$ denotes this distribution function, such that $f(\boldsymbol{x}, \boldsymbol{v}, t)\, d^3\boldsymbol{x}\, d^3\boldsymbol{v}$ is the number of particles in the position $\boldsymbol{x}$ within the volume element $d^3\boldsymbol{x}$, with velocity $\boldsymbol{v}$ within $d^3\boldsymbol{v}$ and at time t, which are under the effect of the (optional) external force $\boldsymbol{F} \equiv \boldsymbol{F}(\boldsymbol{x})$[2]. If collisions are neglected, the above-said particles at the time $t + \Delta t$ will have moved to the new position $\boldsymbol{x} + \boldsymbol{v}\Delta t$ with a velocity $\boldsymbol{v} + \boldsymbol{F}\Delta t$, within the same volume element $d^3\boldsymbol{x}\, d^3\boldsymbol{v}$ (due to Liouville's theorem), that is:

$$f(\boldsymbol{x} + \boldsymbol{v}\Delta t, \boldsymbol{v} + \boldsymbol{F}\Delta t, t + \Delta t)\, d^3\boldsymbol{x}\, d^3\boldsymbol{v} = f(\boldsymbol{x}, \boldsymbol{v}, t)\, d^3\boldsymbol{x}\, d^3\boldsymbol{v} \tag{A.1}$$

which for $\Delta t \to 0$, becomes:

$$\frac{D}{Dt} f = 0 \tag{A.2}$$

where D/Dt denotes the *total derivative* (also called *material derivative*), showing that f is conserved during time evolution. Since f is a distribution function, the integration of a quantity A weighted by f gives the average value of that quantity:

$$\frac{\int Af}{\int f} =< A >$$

[1] For simplicity of notation m will not be shown and assumed to be $m = 1$.

[2] Actually within the notation adopted in this section $\boldsymbol{F}$ is a force per unit mass $m = 1$, i.e. $\boldsymbol{F} = \boldsymbol{F}/m$.

In particular, from the first three *moments* of f with respect to the velocity $\boldsymbol{v}$ the following macroscopic quantities are obtained:

$$\begin{aligned} \int d^3\boldsymbol{v}\, f &= n \\ \frac{1}{n}\int d^3\boldsymbol{v}\, f v_\alpha &=< v_\alpha >= u_\alpha \\ \frac{1}{n}\int d^3\boldsymbol{v}\, f\frac{v^2}{2} &= K \end{aligned} \tag{A.3}$$

which are, respectively, the number of particles per unit volume or density $n \equiv n(\boldsymbol{x})$, the average velocity $\boldsymbol{u} \equiv \boldsymbol{u}(\boldsymbol{x})$ and the kinetic energy. These are macroscopic quantities that are transported by the gas. Equation A.2 can be rewritten equivalently:

$$\frac{\partial}{\partial t}f + (\boldsymbol{v}\cdot\nabla_{\boldsymbol{x}})f + (\boldsymbol{F}\cdot\nabla_{\boldsymbol{v}})f = 0 \tag{A.4}$$

to obtain what is called *collisionless Boltzmann equation* or *Vlasov equation* (commonly in plasma physics). This equation describes the microscopic time evolution of the distribution function for a collisionless gas. The fact that the collisions are absent in this equation means that this gas cannot ever reach any equilibrium state. It is well known that, in absence of an external force, the equilibrium distribution of a gas is the Maxwell-Boltzmann distribution:

$$f^0(\boldsymbol{v}) = \frac{n}{(2\pi kT)^{3/2}} e^{-\frac{(\boldsymbol{v}-\boldsymbol{u})^2}{2kT}} \tag{A.5}$$

Similarly to A.3 the moments of this distribution can be computed as follows:

$$\begin{aligned} &\int f^0 = n \\ &\int f^0\,(v_\alpha - u_\alpha) = 0 \\ &\int f^0\,(v_\alpha - u_\alpha)(v_\beta - u_\beta) = nkT\delta_{\alpha\beta} \\ &\int f^0\,(v_\alpha - u_\alpha)(v_\beta - u_\beta)(v_\gamma - u_\gamma) = 0 \\ &\int f^0\,(v_\alpha - u_\alpha)(v_\beta - u_\beta)|\boldsymbol{v}-\boldsymbol{u}|^2 = 5n(kT)^2\delta_{\alpha\beta} \end{aligned} \tag{A.6}$$

The collisions between particles have the effect of changing the value of f and can be accounted for by adding a term to the right-hand side of the equation A.4:

$$\frac{\partial}{\partial t}f + (\boldsymbol{v}\cdot\nabla_{\boldsymbol{x}})f + (\boldsymbol{F}\cdot\nabla_{\boldsymbol{v}})f = \left(\frac{\partial}{\partial t}f\right)_{collision} \tag{A.7}$$

The general expression for the collision term $(\partial_t f)_{collision}$ is very complicated and will not be reported here. Instead, the common BGK (Bhatnagar-Gross-Krook) approximation will be used, which is based on the observation that the effect of collisions over time is to lead the distribution f towards the equilibrium distribution f^0. Equation A.7 becomes:

$$\frac{\partial}{\partial t}f + (\boldsymbol{v}\cdot\nabla_{\boldsymbol{x}})f + (\boldsymbol{F}\cdot\nabla_{\boldsymbol{v}})f = -\frac{1}{\tau}(f - f^0) \tag{A.8}$$

where the approximated collision term is linear in f and f^0 is a local Maxwell-Boltzmann distribution (i.e. n, $\boldsymbol{u}$ and T depends on position $\boldsymbol{x}$). The constant τ, called *relaxation time*, is the characteristic time between collisions, and its inverse, $1/\tau$, is the *collision frequency*. It is simple to show that if f is uniform in space and $\boldsymbol{F} = 0$, i.e. $\partial t f = -(f - f^0)/\tau$, then f exponentially converges to f^0 with a time constant τ, i.e. equilibrium is rapidly reached after few collisions. Although this seems quite a drastic approximation, equation A.8 is enough to derive the full hydrodynamic equations.

The Boltzmann equation describes microscopically the evolution of the particles in a gas, however, fluid dynamics is more concerned with the evolution of *macroscopic* quantities like the fluid density ρ, the fluid velocity field u, the temperature T and so on. In analogy from the equations A.3, where the moments of the distribution function f are directly connnected to the macroscopic quantities, taking the *moments* of the Boltzmann equation A.8, i.e. integrating in some power of $\boldsymbol{v}$ both members of the equation, leads to conservation equations for the macroscopic quantities, as shown in the following section.

A.2 Hydrodynamics

The zero-order moment of the Boltzmann equation A.8 is obtained simply by integrating both members with respect to velocity $\boldsymbol{v}$

$$\partial_t \int d^3\boldsymbol{v} f + \partial_{x_\alpha} \int d^3\boldsymbol{v} f v_\alpha + F_\alpha \int d^3\boldsymbol{v} \partial_{v_\alpha} f = -\frac{1}{\tau} \int d^3\boldsymbol{v} (f - f^0)$$

The distribution function f can be approximated, from equation A.8, by the equilibrium distribution as $f = f^0 - \tau(\partial t + \boldsymbol{v} \cdot \nabla_{\boldsymbol{x}} + \boldsymbol{F} \cdot \nabla_{\boldsymbol{v}}) f$, and using the equations A.6 for the moments of the distribution f^0, last equation trivially[3] becomes (to first order in derivatives) the equation of the conservation of mass:

$$\partial_t n + \partial_\alpha (n u_\alpha) = 0 \tag{A.9}$$

Expliciting m and defining $\rho = nm$ the mass density, in vector notation this is the *continuity equation*:

$$\partial_t \rho + \nabla \cdot (\rho \boldsymbol{u}) = 0 \tag{A.10}$$

Similarly, the first order moment of the Boltzmann equation is obtained multiplying by v_α and integrating $\int d^3\boldsymbol{v} v_\alpha(\dots)$ both members of the equation. The computation in much more involved, but it ultimately leads to the equation for the conservation of momentum:

$$n\partial_t u_\alpha + n u_\beta \partial_\beta u_\alpha = -\partial_\alpha (nkT) + nF_\alpha + \partial_\beta [\eta(\partial_\beta u_\alpha + \partial_\alpha u_\beta - \frac{2}{3}\partial_\gamma u_\gamma \delta_{\alpha\beta})] \tag{A.11}$$

This equation can be rewritten in vector notation in the more familiar form, called *Navier-Stokes equation*:

$$\rho \partial_t \boldsymbol{u} + \rho(\boldsymbol{u} \cdot \nabla)\boldsymbol{u} = -\nabla P + \mathrm{F} + \nabla \cdot [\eta(\nabla \boldsymbol{u} + (\nabla \boldsymbol{u})^T)] - \frac{2}{3}\nabla(\eta(\nabla \cdot \boldsymbol{u})) \tag{A.12}$$

where $P = nkT$ and $\eta = nkT\tau$ are, respectively, the pressure and the viscosity of a gas, $\mathrm{F} = \rho \boldsymbol{F}/m$ is a force per unit volume, $\nabla \boldsymbol{u}$ denotes the Jacobian matrix of $\boldsymbol{u}$ and

[3] remembering that for the Gauss's theorem $F_\alpha \int d^3\boldsymbol{v} \partial_{v_\alpha} f = \int d^3\boldsymbol{v} \partial_{v_\alpha}(F_\alpha f) = 0$ since it is the integral of the divergence of the vector $\boldsymbol{F} f$, and f vanishes at infinite.

$(\nabla \boldsymbol{u})^T$ its transpose. Although this equation has been derived from the Boltzmann equation for a dilute gas, it is well known that this equation can accurately describe a general *Newtonian* fluid.With the additional assumptions of constant viscosity η (which in general may depend on the local temperature T) and incompressible fluid ($\nabla \cdot \boldsymbol{u} = 0$) this equation simplifies to

$$\rho \partial_t \boldsymbol{u} + \rho(\boldsymbol{u} \cdot \nabla)\boldsymbol{u} = -\nabla P + \mathrm{F} + \eta \nabla^2 \boldsymbol{u} \tag{A.13}$$

This last equation tells that the vector field $\boldsymbol{u}(\boldsymbol{x}, t)$ changes in time ($\partial_t \boldsymbol{u}$) due to different contributions. The term $(\boldsymbol{u} \cdot \nabla)A$ represents *advection* of some general quantity A along the field $\boldsymbol{u}$, i.e. the fluid carries the quantity A as it flows. In particular in $(\boldsymbol{u} \cdot \nabla)\boldsymbol{u}$ the same velocity $\boldsymbol{u}$ is advected by $\boldsymbol{u}$, and this is commonly called *inertial* term. The term $\eta \nabla^2 \boldsymbol{u}$ instead denotes *diffusion* of the velocity field $\boldsymbol{u}$. Diffusion $\nabla^2 A$ of some quantity A has the effect of "spreading" A in nearby regions until it becomes uniform in space. In particular, diffusion of momentum $\eta/\rho \nabla^2(\rho \boldsymbol{u})$ gives rise to the effects of *viscosity*, where the diffusion constant $\nu = \eta/\rho$ is called *kinematic viscosity*, η is called *dynamic viscosity*. Thus $\eta \nabla^2 \boldsymbol{u}$ is commonly called *viscous term*. The remaining two terms represent the force exterted on the fluid by *pressure* P and some general *external force* F, e.g. gravity.

The second order moment of the Boltzmann equation, again, leads to a conservation equation which is called *heat conduction equation*, and the conserved quantity is energy. It is omitted here because it is not of much use for the rest of this thesis, as the systems studied are usually isothermal.

Lastly, a very important point to stress is the connection between the microscopic nature of the fluid, described by the Boltzman equation, and its behaviour at the macroscopic scale, which is described by the *moments* of the equation and of the distribution function. The equations A.9 and A.11 have been derived from the Boltzmann equation A.8 without particular assumptions on the miscoscopic nature of the gas, but only assuming particular properties for the equilibrium distribution f^0. Actually, in order to derive the hydrodynamic equations, the miscoscopic system described by f is not even required to be a physical gas behaving "in the usual way", as long as its equilibrium distribution f^0 has the same *moments*. This fact is at the very fundation of the Lattice Boltzmann Method, described in the next section.

A.3 Lattice Boltzmann Method

Computational fluid dynamics techniques commonly involve the discretization of the hydrodynamic equations A.9 and A.11, in order to solve them by many possible numerical schemes, e.g. finite differences methods. Particular care has to be taken if mass, momentum and energy have to be accurately conserved.

In a Lattice Boltzmann Method the solution of the Boltzmann equation is attempted instead. Such solution will then automatically satisfy the hydrodynamic equations as a consequence.

The finite difference in equation A.1, together with the collision term, can be rearranged (for $\Delta t \to 0$) in the following way[4]:

$$f(\boldsymbol{x} + \boldsymbol{v}\Delta t, \boldsymbol{v}, t + \Delta t) - f(\boldsymbol{x}, \boldsymbol{v}, t) + (\boldsymbol{F} \cdot \nabla_{\boldsymbol{v}}) f \Delta t = -\frac{1}{\tau}(f - f^0)\Delta t \tag{A.14}$$

[4]by adding and subtracting the term $f(\boldsymbol{x} + \boldsymbol{v}\Delta t, \boldsymbol{v}, t + \Delta t)$

to obtain an equation which is equivalent to the Boltzmann equation A.8, except for the external force term being explicited out from the difference, which now represents only advection. This equation can be discretized with the constrains that time takes integer values ($\Delta t = 1$), and both $\boldsymbol{x}$ and $\boldsymbol{v}$ take values on a lattice (e.g. $\boldsymbol{x} \in \mathbb{Z}^3, \boldsymbol{v} \in \mathbb{Z}^3$) in such a way that, if $\boldsymbol{x}$ is a node in this lattice, then $\boldsymbol{x} + \boldsymbol{v}$ is again a node in the lattice. For every $\boldsymbol{x}$ there is a full set of possible velocities $\boldsymbol{v}$ (i.e. $(\boldsymbol{x}, \boldsymbol{v}) \in \mathbb{Z}^3 \times \mathbb{Z}^3$). Last equation then reads:

$$f(\boldsymbol{x} + \boldsymbol{v}, \boldsymbol{v}, t+1) - f(\boldsymbol{x}, \boldsymbol{v}, t) + \mathrm{F}(\boldsymbol{x}, \boldsymbol{v}) = -\frac{1}{\tau}\left(f(\boldsymbol{x}, \boldsymbol{v}, t) - f^0(\boldsymbol{v}, n, \boldsymbol{u}, T)\right) \qquad \text{(A.15)}$$

where $\mathrm{F}(\boldsymbol{x}, \boldsymbol{v})$ generalizes the force term $(\boldsymbol{F} \cdot \nabla_{\boldsymbol{v}})f$. Once an expression for F is chosen (or if it is just assumed to be zero) then, in principle, equation A.15 already defines a numerical scheme for solving the Boltzmann equation. In fact, once f and the macroscopic quantities $n(\boldsymbol{x}), \boldsymbol{u}(\boldsymbol{x}), T(\boldsymbol{x})$ are initialized at the time t, then equation A.15 tells how to compute the values of f for all the lattice nodes at time $t+1$. Once f is computed, the new macroscopic quantities for time $t+1$ can be computed from the moments of f with A.3[5]. The discrete equation A.15, expanded in Taylor series, returns to the original Boltzmann equation[6], therefore it simulates the time evolution of the macroscopic quantities as described by the Navier Stokes equations A.11.

Although in principle with this discretization scheme the Boltzmann equation could be integrated, it is evident that this would be impractical. If $L = N\Delta x$ denotes the lateral size of the lattice (i.e. $|\boldsymbol{x}| < L$), and if $|\boldsymbol{v}|$ also has some upper limit, say $L/\Delta t$, then the lattice size (for a tridimensional system) is of the order $\sim L^6$, which corresponds to $\sim N^6$ lattice nodes to be updated at every time step. For non-trivial problems, this can be impractical even in a modern cluster of supercomputers.

A.3.1 Lattice Boltzmann equation

The power of the Lattice Boltzmann Method relies on the fact that, in order for the hydrodynamic equations A.9 and A.11 to be derived from the Boltzman equation, the equilibrium distribution f^0 is not required to be the Maxwell-Boltzmann distribution A.5, which is defined in all $\mathbb{R}^3$. The distribution f^0 is only required to have the same *moments* as the Maxwell-Boltzmann. That is, any function $f^0(\boldsymbol{v})$ which have the properties expressed in equations A.6 will be enough. In particular, it is not required to be defined in all $\mathbb{R}^3$, but instead it can be defined only for a smaller set of velocities $\boldsymbol{v_i}$, such that $\boldsymbol{x}$ is connected by $\boldsymbol{v_i}$ only to it first neighbors (or up to some neighborhood order). This only fact reduces the number of computations per time step from $\sim N^6$ to $\sim kN^3$, where k is the number of first neighbors, which is of the order of tens for a tridimensional problem. Equation A.15 thus becomes:

$$f(\boldsymbol{x} + \boldsymbol{v_i}, \boldsymbol{v_i}, t+1) - f(\boldsymbol{x}, \boldsymbol{v_i}, t) + F(\boldsymbol{x}, \boldsymbol{v_i}) = -\frac{1}{\tau}\left(f(\boldsymbol{x}, \boldsymbol{v_i}, t) - f^0(\boldsymbol{v_i}, n, \boldsymbol{u}, T)\right) \quad \text{(A.16)}$$

The velocities $\boldsymbol{v_i}$ can be written as $\boldsymbol{v_i} = c\boldsymbol{e_i}$, where the adimensional vector $\boldsymbol{e_i}$ connects the lattice node $\boldsymbol{x}$ with its i-th nearest neighbor, and $c = \Delta x/\Delta t$, called *lattice speed of sound*, contains the spacing between lattice nodes Δx. Since the set of possible microscopic velocities $\boldsymbol{v_i}$ is small, it is convenient to write the distibution function in the following notation:

$$f_i(\boldsymbol{x}, t) \equiv f(\boldsymbol{x}, \boldsymbol{v_i}, t)$$

[5] at time $t+1$ the parameters of the equilibrium distribution f^0 are updated with the ones extracted from the out-of-equilibrium distribution f, as an approximation.

[6] with a difference in the collision time that is renormalized as $\tau \to \tau - 1/2$.

The macroscopic quantities associated to f_i can be computed by the analogous of A.3:

$$\begin{aligned} \sum_i f_i &= n \\ \frac{1}{n}\sum_i f_i c\boldsymbol{e_i} &= \boldsymbol{u} \end{aligned} \tag{A.17}$$

With the same notation for the force term $F_i \equiv F(\boldsymbol{x}, \boldsymbol{v_i})$, equation A.16 can be written in the more compact form

$$f_i(\boldsymbol{x} + c\boldsymbol{e_i}, t+1) - f_i(\boldsymbol{x}, t) + F_i(\boldsymbol{x}) = -\frac{1}{\tau}\left(f_i(\boldsymbol{x}, t) - f_i^0(n, \boldsymbol{u}, T)\right) \tag{A.18}$$

which is called *lattice Boltzmann equation*. The are many possible choices for the set of velocities $\boldsymbol{v_i}$, which can constrain the conservation properties of the equation. If the number of velocities is large enough it is possible for this equation to satisfy the conservation laws for mass (eq. A.9), momentum (eq. A.11) and energy. Instead, by using a reduced number of velocities, it is possible to limit the equation to satisfy the conservation laws of mass and momentum only, thus not conserving energy but instead keeping a constant temperature T. In this latter case the lattice Boltzmann is *isothermal*, and this is the most common situation.

Figure A.1 shows a 2-dimensional example of such an isothermal lattice, called *D2Q9* (2 dimensions and 9 velocities). In this lattice for every (spatial) node, represented by a dot in Fig. A.1a, there are 9 possible velocities $\boldsymbol{v_i} = c\boldsymbol{e_i}$ leading to the first neighboring nodes and to the node itself (with velocity $\boldsymbol{v_0} = 0$).

A.3.2 Equilibrium distribution

The equilibrium distribution function f_i^0 can be derived, with a polynomial expansion, from the Maxwell-Boltzmann distribution A.5 for $u \ll c$:

$$f_i^0 = n w_i \left(1 + \frac{3}{c^2}\boldsymbol{u}\cdot\boldsymbol{v_i} + \frac{9}{2c^4}(\boldsymbol{u}\cdot\boldsymbol{v_i})^2 - \frac{3}{c^2}\boldsymbol{u}\cdot\boldsymbol{u}\right) \tag{A.19}$$

where $c = \sqrt{3kT}$ and the weights w_i depend on the set of velocities. In particular, for the D2Q9 set $w_0 = 4/9, w_1 = w_2 = w_3 = w_4 = 1/9, w_5 = w_6 = w_7 = w_8 = 1/36$.

To this equilibrium distribution there correspond the same moments of the original Maxwell-Boltzmann distribution (A.6). Therefore the corresponding macroscopic quantities, like n and $\boldsymbol{u}$, evolve in time with the lattice Boltzmann equation A.18 in the same way as the original Boltzmann equation A.8, that is according to the hydrodynamic equations A.9 and A.11.

A.3.3 Time evolution

The time evolution of f, as directly stated by the lattice Boltzmann equation A.18, can be implemented with the following algorithm for each time step:

1. *Macroscopic quantities*: At the time step t, the macroscopic quantities n and $\boldsymbol{u}$, for the lattice node $\boldsymbol{x}$, are computed from the distribution f_i by A.17, or are initialized to some value if $t = 0$.

2. *Equilibrium distribution*: the values of the equilibrium distribution f_i^0 are computed with A.19 from the macroscopic quantities

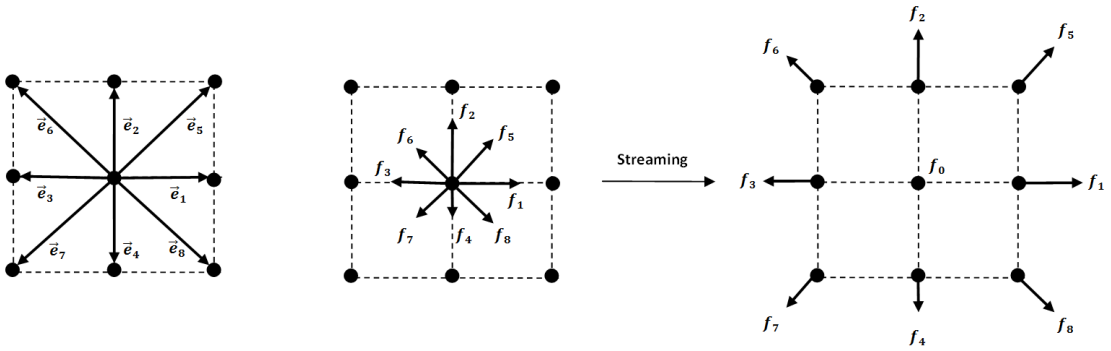

(a) Lattice Node (b) Streaming

Figure A.1: (a) Representation of a node (central dot) and its 8 neighbours in a two-dimensional (D2Q9) lattice. The node has a generic position $\boldsymbol{x}$ and is connected to its neighbouring nodes at positions $\boldsymbol{x} + \boldsymbol{v_i}\Delta t = \boldsymbol{x} + \Delta x \boldsymbol{e_i}$ for $i = 0, ..., 8$ with $\boldsymbol{e_0}$ connecting the node to itself. In the figure $\Delta x = \Delta t = c = 1$. (b) Streaming step in the time evolution from t to $t + \Delta t$. The post-collision values of the distribution function $f_0, ..., f_8$ in the node $\boldsymbol{x}$ (central dot) are transferred to the corresponding neighbouring nodes, with f_0 remaining in place. That is, the fraction of particles with velocity $\boldsymbol{v_i}$, $f_i = f(\boldsymbol{x}, \boldsymbol{v_i})$, is moved to the position $\boldsymbol{x} + \boldsymbol{v_i}\Delta t$. This operation is performed simultaneously for all the nodes in the lattice therefore, e.g, the value f_1 in the central node after the streaming step will be the value f_1 that was previously in the left node at position $\boldsymbol{x} - \boldsymbol{v_1}\Delta t = \boldsymbol{x} + \Delta x \boldsymbol{e_3}$. Source of the pictures:[96].

3. *Collision*: the values of the distribution function after collision are computed from A.18 as $f_i^*(t) = f_i(t) - (f_i(t) - f_i^0)/\tau - F_i$

4. *Streaming*: the post-collision values f_i^*, at the node $\boldsymbol{x}$, are transferred to the corresponding neighbouring nodes for time $t+1$, i.e. $f_i(\boldsymbol{x} + c\boldsymbol{e_i}, t+1) = f_i^*(\boldsymbol{x}, t)$, as in Fig. A.1b

If the above operations are applied simultaneously to all the nodes in the lattice, the microscopic gas described by the distribution function f_i will have evolved by one time step. Such microscopic gas, of course, is not realistic, since its particles can only jump from one node to the surrounding ones, with fixed velocities. What is important, however, is that the fraction of particles that move in each direction, i.e. f_i, are such that the macroscopic quantities computed by A.17 evolve according to the Navier-Stokes equation. Therefore this gas, macroscopically, can describe a realistic fluid.

A.3.4 Boundary conditions

The boundary conditions can be imposed in a number of different ways. The simplest one is the no-slip boundary condition, which states that at a solid wall the macroscopic velocity field is $\boldsymbol{u} = 0$. This can be implemented in the lattice Boltzmann with the so called *bounce-back* rule. The solid wall lies at halfway between two nodes, as shown in Fig.A.2. The bounce-back rule applies only to the components f_i that have velocities directed to the wall. After these are streamed to the nodes past the wall, they are inverted and then streamed back to the origin node. This way the macroscopic velocity $\boldsymbol{u}$ at the wall, computed from f_i by A.17, is forced to be zero.

Other kind of boundary conditions, like velocity or pressure boundary conditions, can be implemented as well by imposing particular properties to the values f_i at the boundary, in order to force some value of the velocity $\boldsymbol{u}$ or the density n, the latter being proportional to the pressure by $P = nkT$.

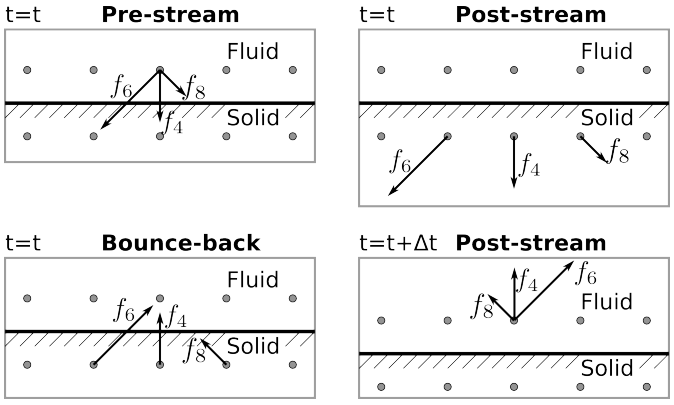

Figure A.2: Representation of the bounce-back rule boundary condition. The time evolution of the solid nodes is treated differently from the others, and the solid-fluid interface (the wall) virtually lies in the middle between two neighbouring solid and fluid nodes. *Top*: the streaming step of the post-collision values f_i is performed as usual, as described in Fig. A.1b, only for the nodes which lie in the fluid. *Bottom*: after streaming, the values f_i which have crossed the wall are returned back to their original position and with inverted velocities. This way, the macroscopic velocity at the wall is approximately zero.

A.4 Lattice Boltzmann methods with surface tension

There are many approaches to the implementation of interfacial phenomena in lattice Boltzmann simulations. In the case of droplet microfluidics, the two-phase flow can be either described as a single component fluid, in which there is a separation between a liquid phase and a vapor phase, using the same lattice Boltzmann equation A.18, or as a multiple component fluid, i.e. with a mixture of two or more different species of particles. In the latter case, the lattice Boltzman equation is extended to include a distribution function f^α for each component $\alpha = a, b, \ldots$ of the fluid. For example, a binary fluid is described by f^a and f^b. The two components are usually treated independently, that is they relax toward equilibrium each with its own relaxation time τ_α. The equation then becomes the following:

$$f_i^\alpha(\boldsymbol{x} + c\boldsymbol{e_i}, t+1) - f_i^\alpha(\boldsymbol{x}, t) = -\frac{1}{\tau_\alpha}\left(f_i^\alpha(\boldsymbol{x}, t) - f_i^{\alpha,0}(n, \boldsymbol{u}, T)\right) \tag{A.20}$$

the main difference in the various methods is the way in which the interaction between the components is included.

A.4.1 Free Energy models

Since the lattice Boltzman method comes from a microscopic description of a fluid, the natural approach is to define a free energy, in a similar way as in Sec. 1.5.1, which is the sum of a bulk term and of some function of the gradients of the densities n^a and n^b of the two components. Briefly, once the free energy is defined, a non-ideal pressure tensor $P_{\alpha\beta}$ is computed, which contains the equation of state of the non-ideal fluid. The equilibrium distribution function $f^{\alpha,0}$ is then modified from A.19 to include $P_{\alpha\beta}$, in such a way as to recover the Navier-Stokes equations where a non ideal pressure appears. Although this approach is quite involved, it ultimately leads to a thermodinamically consistent description of phase separation[97, 98].

A.4.2 Shan-Chen model

Another, much simpler approach is the so-called Shan-Chen method[99]. Although it proves not to be thermodinamically consistent, it still exhibits phase separation and is effective in implementing interfacial phenomena in lattice Boltzmann simulations. Thus, due to its simplicity, is widely adopted. The interaction between the particles is introduced with a potential V of the form:

$$V(\boldsymbol{x}, \boldsymbol{x'}) = \sum_{\alpha} \sum_{\beta} G_{\alpha\beta}(\boldsymbol{x}, \boldsymbol{x'})\, \psi^{\alpha}(n^{\alpha}(\boldsymbol{x}))\, \psi^{\beta}(n^{\beta}(\boldsymbol{x'}))$$

where the value $G_{\alpha\beta}(\boldsymbol{x}, \boldsymbol{x'})$ is the strenght of the interaction between the components α and β and its sign determines wheter the interaction is attractive or repulsive. It is different from zero only when $\boldsymbol{x}$ and $\boldsymbol{x'}$ are first neighbours. The function $\psi(n)$ is an "effective density" and is usually assumed to be of the form $\psi(n) = n_0(1 - \mathrm{e}^{-n/n_0})$ or even just $\psi(n) = n$. With this interaction potential, the force, or rate of change of momentum for the particles α in the node $\boldsymbol{x}$ is:

$$\frac{d\boldsymbol{p}^{\alpha}}{dt}(\boldsymbol{x}) = -\psi^{\alpha}(\boldsymbol{x}) \sum_{\beta} G_{\alpha\beta} \sum_{i} \psi^{\beta}(\boldsymbol{x} + c\boldsymbol{e_i}) c\boldsymbol{e_i}$$

This force can then be included as a bulk force (specifying a suitable expression for F_i) in the collision step of time evolution (Sec. A.3.3) or, alternatively, the momentum increment $\tau_{\alpha} d\boldsymbol{p}^{\alpha}/dt$ can be added to the one used to compute the equilibrium distribution function before the collision step.

Bibliography

[1] G. M. Whitesides, "The origins and the future of microfluidics," *Nature*, vol. 442, no. 7101, pp. 368–373, 2006.

[2] Y. Xia and G. M. Whitesides, "Soft lithography," *Annual review of materials science*, vol. 28, no. 1, pp. 153–184, 1998.

[3] P. Tabeling, *Introduction to microfluidics*. Oxford University Press on Demand, 2005.

[4] M. J. Jebrail and A. R. Wheeler, "Let's get digital: digitizing chemical biology with microfluidics," *Current opinion in chemical biology*, vol. 14, no. 5, pp. 574–581, 2010.

[5] P. Marguet, F. Balagadde, C. Tan, and L. You, "Biology by design: reduction and synthesis of cellular components and behaviour," *Journal of The Royal Society Interface*, vol. 4, no. 15, pp. 607–623, 2007.

[6] M. R. Bringer, C. J. Gerdts, H. Song, J. D. Tice, and R. F. Ismagilov, "Microfluidic systems for chemical kinetics that rely on chaotic mixing in droplets," *Philosophical Transactions of the Royal Society of London A: Mathematical, Physical and Engineering Sciences*, vol. 362, no. 1818, pp. 1087–1104, 2004.

[7] C. N. Baroud, F. Gallaire, and R. Dangla, "Dynamics of microfluidic droplets," *Lab on a Chip*, vol. 10, no. 16, pp. 2032–2045, 2010.

[8] K.-W. Song, Y.-S. Kim, and G.-S. Chang, "Rheology of concentrated xanthan gum solutions: steady shear flow behavior," *Fibers and Polymers*, vol. 7, no. 2, pp. 129–138, 2006.

[9] M. Milas, M. Rinaudo, and B. Tinland, "The viscosity dependence on concentration, molecular weight and shear rate of xanthan solutions," *Polymer Bulletin*, vol. 14, no. 2, pp. 157–164, 1985.

[10] S. E. Spagnolie, "Complex fluids in biological systems," *Biological and Medical Physics, Biomedical Engineering. Springer, New York*, 2015.

[11] J. R. Stokes, L. J. Graham, N. J. Lawson, and D. V. Boger, "Swirling flow of viscoelastic fluids. part 2. elastic effects," *Journal of Fluid Mechanics*, vol. 429, pp. 117–153, 2001.

[12] I. B. Bekard, P. Asimakis, J. Bertolini, and D. E. Dunstan, "The effects of shear flow on protein structure and function," *Biopolymers*, vol. 95, no. 11, pp. 733–745, 2011.

[13] J. W. Cahn and J. E. Hilliard, "Free energy of a nonuniform system. i. interfacial free energy," *The Journal of chemical physics*, vol. 28, no. 2, pp. 258–267, 1958.

[14] T. Thorsen, R. W. Roberts, F. H. Arnold, and S. R. Quake, "Dynamic Pattern Formation in a Vesicle-Generating Microfluidic Device," *Physical Review Letters*, vol. 86, no. 18, pp. 4163–4166, 2001.

[15] G. F. Christopher, N. N. Noharuddin, J. A. Taylor, and S. L. Anna, "Experimental observations of the squeezing-to-dripping transition in T-shaped microfluidic junctions," *Physical Review E*, vol. 78, no. 3, p. 036317, 2008.

[16] S. L. Anna, N. Bontoux, and H. A. Stone, "Formation of dispersions using âĂIJflow focusingâĂİ in microchannels," *Applied physics letters*, vol. 82, no. 3, pp. 364–366, 2003.

[17] A. Marin, F. Campo-Cortés, and J. Gordillo, "Generation of micron-sized drops and bubbles through viscous coflows," *Colloids and Surfaces A: Physicochemical and Engineering Aspects*, vol. 344, no. 1, pp. 2–7, 2009.

[18] G. F. Christopher and S. L. Anna, "Microfluidic methods for generating continuous droplet streams," *Journal of Physics D: Applied Physics*, vol. 40, no. 19, p. R319, 2007.

[19] A. S. Utada, A. Fernandez-Nieves, H. A. Stone, and D. A. Weitz, "Dripping to jetting transitions in coflowing liquid streams," *Physical review letters*, vol. 99, no. 9, p. 094502, 2007.

[20] P. Umbanhowar, V. Prasad, and D. Weitz, "Monodisperse emulsion generation via drop break off in a coflowing stream," *Langmuir*, vol. 16, no. 2, pp. 347–351, 2000.

[21] E. Castro-Hernández, F. Campo-Cortés, and J. M. Gordillo, "Slender-body theory for the generation of micrometre-sized emulsions through tip streaming," *Journal of Fluid Mechanics*, vol. 698, pp. 423–445, 2012.

[22] A. S. Utada, A. Fernandez-Nieves, J. M. Gordillo, and D. A. Weitz, "Absolute instability of a liquid jet in a coflowing stream," *Physical review letters*, vol. 100, no. 1, p. 014502, 2008.

[23] J. M. Gordillo, A. Sevilla, and F. Campo-Cortés, "Global stability of stretched jets: conditions for the generation of monodisperse micro-emulsions using coflows," *Journal of Fluid Mechanics*, vol. 738, pp. 335–357, 2014.

[24] K. J. Humphry, A. Ajdari, A. Fernández-Nieves, H. A. Stone, and D. A. Weitz, "Suppression of instabilities in multiphase flow by geometric confinement," *Physical Review E*, vol. 79, no. 5, p. 056310, 2009.

[25] P. Garstecki, M. J. Fuerstman, H. A. Stone, and G. M. Whitesides, "Formation of droplets and bubbles in a microfluidic T-junction—scaling and mechanism of break-up," *Lab on a Chip*, vol. 6, no. 3, pp. 437–446, 2006.

[26] M. Hoorfar and A. W. Neumann, "Recent progress in axisymmetric drop shape analysis (adsa)," *Advances in Colloid and Interface Science*, vol. 121, no. 1–3, pp. 25 – 49, 2006.

[27] J. C. McDonald, , and G. M. Whitesides*, "Poly(dimethylsiloxane) as a material for fabricating microfluidic devices," *Accounts of Chemical Research*, vol. 35, no. 7, pp. 491–499, 2002. PMID: 12118988.

[28] T. Tóth, D. Ferraro, E. Chiarello, M. Pierno, G. Mistura, G. Bissacco, and C. Semprebon, "Suspension of water droplets on individual pillars," *Langmuir*, vol. 27, no. 8, pp. 4742–4748, 2011.

[29] J. Xu, S. Li, J. Tan, Y. Wang, and G. Luo, "Controllable preparation of monodisperse o/w and w/o emulsions in the same microfluidic device," *Langmuir*, vol. 22, no. 19, pp. 7943–7946, 2006.

[30] W.-A. C. Bauer, M. Fischlechner, C. Abell, and W. T. S. Huck, "Hydrophilic pdms microchannels for high-throughput formation of oil-in-water microdroplets and water-in-oil-in-water double emulsions," *LAB ON A CHIP*, vol. 10, pp. 1814–1819, 2010 2010.

[31] L. Derzsi, P. Jankowski, W. Lisowski, and P. Garstecki, "Hydrophilic polycarbonate for generation of oil in water emulsions in microfluidic devices," *LAB ON A CHIP*, vol. 11, pp. 1151–1156, 2011 2011.

[32] S. Begolo, G. Colas, J.-L. Viovy, and L. Malaquin, "New family of fluorinated polymer chips for droplet and organic solvent microfluidics," *LAB ON A CHIP*, vol. 11, pp. 508–512, 2011 2011.

[33] C. Holtze, A. C. Rowat, J. J. Agresti, J. B. Hutchison, F. E. Angile, C. H. J. Schmitz, S. Koster, H. Duan, K. J. Humphry, R. A. Scanga, J. S. Johnson, D. Pisignano, and D. A. Weitz, "Biocompatible surfactants for water-in-fluorocarbon emulsions," *LAB ON A CHIP*, vol. 8, pp. 1632–1639, OCT 2008 2008.

[34] M. Zagnoni and J. M. Cooper, "A microdroplet-based shift register," *Lab Chip*, vol. 10, pp. 3069–3073, 2010.

[35] T. Nisisako, T. Torii, and T. Higuchi, "Droplet formation in a microchannel network," *LAB ON A CHIP*, vol. 2, pp. 24–26, 2002 2002.

[36] N. Wu, Y. Zhu, S. Brown, J. Oakeshott, T. S. Peat, R. Surjadi, C. Easton, P. W. Leech, and B. A. Sexton, "A pmma microfluidic droplet platform for in vitro protein expression using crude e. coli s30 extract," *LAB ON A CHIP*, vol. 9, pp. 3391–3398, 2009 2009.

[37] V. Barbier, M. Tatoulian, H. Li, F. Arefi-Khonsari, A. Ajdari, and P. Tabeling, "Stable modification of pdms surface properties by plasma polymerization: Application to the formation of double emulsions in microfluidic systems," *LANGMUIR*, vol. 22, pp. 5230–5232, JUN 6 2006 2006.

[38] P. Jankowski, D. Ogonczyk, W. Lisowski, and P. Garstecki, "Polyethyleneimine coating renders polycarbonate resistant to organic solvents," *LAB ON A CHIP*, vol. 12, pp. 2580–2584, 2012 2012.

[39] S. Silvestrini, D. Ferraro, T. Toth, M. Pierno, T. Carofiglio, G. Mistura, and M. Maggini, "Tailoring the wetting properties of thiolene microfluidic materials," *LAB ON A CHIP*, vol. 12, pp. 4041–4043, 2012 2012.

[40] J.-C. Baret, "Surfactants in droplet-based microfluidics," *LAB ON A CHIP*, vol. 12, pp. 422–433, 2012 2012.

[41] C. L. do Lago, H. D. T. da Silva, C. A. Neves, J. G. A. Brito-Neto, and J. A. F. da Silva, "A dry process for production of microfluidic devices based on the lamination of laser-printed polyester films," *ANALYTICAL CHEMISTRY*, vol. 75, pp. 3853–3858, AUG 1 2003 2003.

[42] G. R. M. Duarte, C. W. Price, B. H. Augustine, E. Carrilho, and J. P. Landers, "Dynamic solid phase dna extraction and pcr amplification in polyester-toner based microchip," *ANALYTICAL CHEMISTRY*, vol. 83, pp. 5182–5189, JUL 1 2011 2011.

[43] F. R. de Souza, G. L. Alves, and W. K. Tomazelli Coltro, "Capillary-driven toner-based microfluidic devices for clinical diagnostics with colorimetric detection," *ANALYTICAL CHEMISTRY*, vol. 84, pp. 9002–9007, NOV 6 2012 2012.

[44] E. F. Moreira Gabriel, G. F. Duarte Junior, P. d. T. Garcia, D. P. de Jesus, and W. K. T. Coltro, "Polyester-toner electrophoresis microchips with improved analytical performance and extended lifetime," *ELECTROPHORESIS*, vol. 33, pp. 2660–2667, SEP 2012 2012.

[45] G. R. M. Duarte, W. K. T. Coltro, J. C. Borba, C. W. Price, J. P. Landers, and E. Carrilho, "Disposable polyester-toner electrophoresis microchips for dna analysis," *ANALYST*, vol. 137, pp. 2692–2698, 2012 2012.

[46] S.-Y. Teh, R. Lin, L.-H. Hung, and A. P. Lee, "Droplet microfluidics," *Lab on a Chip*, vol. 8, no. 2, pp. 198–220, 2008.

[47] A. B. Theberge, F. Courtois, Y. Schaerli, M. Fischlechner, C. Abell, F. Hollfelder, and W. T. S. Huck, "Microdroplets in microfluidics: An evolving platform for discoveries in chemistry and biology," *Angewandte Chemie-International Edition*, vol. 49, no. 34, pp. 5846–5868, 2010.

[48] C. N. Baroud, F. Gallaire, and R. Dangla, "Dynamics of microfluidic droplets," *LAB ON A CHIP*, vol. 10, pp. 2032–2045, 2010 2010.

[49] R. Seemann, M. Brinkmann, T. Pfohl, and S. Herminghaus, "Droplet based microfluidics," *REPORTS ON PROGRESS IN PHYSICS*, vol. 75, p. 016601, JAN 2012 2012.

[50] Y. Ouyang, S. Wang, J. Li, P. S. Riehl, M. Begley, and J. P. Landers, "Rapid patterning of 'tunable' hydrophobic valves on disposable microchips by laser printer lithography," *LAB ON A CHIP*, vol. 13, pp. 1762–1771, 2013 2013.

[51] M. Natali, S. Begolo, T. Carofiglio, and G. Mistura, "Rapid prototyping of multilayer thiolene microfluidic chips by photopolymerization and transfer lamination," *LAB ON A CHIP*, vol. 8, pp. 492–494, 2008 2008.

[52] F. O. Opawale and D. J. Burgess, "Influence of interfacial properties of lipophilic surfactants on water-in-oil emulsion stability," *JOURNAL OF COLLOID AND INTERFACE SCIENCE*, vol. 197, pp. 142–150, JAN 1 1998 1998.

[53] J. Xu, S. Li, J. Tan, and G. Luo, "Correlations of droplet formation in t-junction microfluidic devices: from squeezing to dripping," *Microfluidics and Nanofluidics*, vol. 5, no. 6, pp. 711–717, 2008.

[54] H. Bruus, *Theoretical Microfluidics*. Oxford University Press, New York, 2008.

[55] T. Ward, M. Faivre, M. Abkarian, and H. A. Stone, "Microfluidic flow focusing: Drop size and scaling in pressure versus flow-rate-driven pumping," *ELECTROPHORESIS*, vol. 26, pp. 3716–3724, OCT 2005 2005.

[56] C. Cramer, P. Fischer, and E. J. Windhab, "Drop formation in a co-flowing ambient fluid," *Chemical Engineering Science*, vol. 59, no. 15, pp. 3045–3058, 2004.

[57] P. Yager, T. Edwards, E. Fu, K. Helton, K. Nelson, M. R. Tam, and B. H. Weigl, "Microfluidic diagnostic technologies for global public health," *Nature*, vol. 442, no. 7101, pp. 412–418, 2006.

[58] G. S. Retzinger, A. P. DeAnglis, and S. J. Patuto, "Adsorption of fibrinogen to droplets of liquid hydrophobic phases functionality of the bound protein and biological implications," *Arteriosclerosis, thrombosis, and vascular biology*, vol. 18, no. 12, pp. 1948–1957, 1998.

[59] P. Wägli, Y.-C. Chang, A. Homsy, L. Hvozdara, H. P. Herzig, and N. F. de Rooij, "Microfluidic droplet-based liquid–liquid extraction and on-chip ir spectroscopy detection of cocaine in human saliva," *Analytical chemistry*, vol. 85, no. 15, pp. 7558–7565, 2013.

[60] M. Bienia, M. Lejeune, M. Chambon, V. Baco-Carles, C. Dossou-Yovo, R. Noguera, and F. Rossignol, "Inkjet printing of ceramic colloidal suspensions: Filament growth and breakup," *Chemical Engineering Science*, vol. 149, pp. 1–13, 2016.

[61] G. H. Mckinley, "Visco-elasto-capillary thinning and break-up of complex fluids," *Annual Rheology Reviews*, pp. 1–49, 2005.

[62] K. Muijlwijk, C. Berton-Carabin, and K. Schroën, "Cross-flow microfluidic emulsification from a food perspective," *Trends in Food Science & Technology*, vol. 49, pp. 51–63, 2016.

[63] T. Fu, L. Wei, C. Zhu, and Y. Ma, "Flow patterns of liquid–liquid two-phase flow in non-newtonian fluids in rectangular microchannels," *Chemical Engineering and Processing: Process Intensification*, vol. 91, pp. 114 – 120, 2015.

[64] B. Steinhaus, A. Q. Shen, and R. Sureshkumar *Phys. Fluids*, vol. 19, p. 073103, 2007.

[65] G. F. Christopher and S. L. Anna, "Passive breakup of viscoelastic droplets and filament self-thinning at a microfluidic T-junction," *Journal of Rheology (1978-present)*, vol. 53, no. 3, pp. 663–683, 2009.

[66] P. E. Arratia, J. P. Gollub, and D. J. Durian *Phys. Rev. E*, vol. 77, p. 036309, 2008.

[67] P. E. Arratia, L.-A. Cramer, J. P. Gollub, and D. J. Durian, "The effects of polymer molecular weight on filament thinning and drop breakup in microchannels," *New J. Phys.*, vol. 11, p. 115006, 2009.

[68] L. Derzsi, M. Kasprzyk, J.-P. Plog, and P. Garstecki, "Flow focusing with viscoelastic liquids," *Phys. Fluids*, vol. 25, p. 092001, 2013.

[69] Y. Ren, Z. Liu, and H. C. Shum, "Breakup dynamics and dripping-to-jetting transition in a newtonian/shear-thinning multiphase microsystem," *Lab on a Chip*, vol. 15, no. 1, pp. 121–134, 2015.

[70] T. Fu and Y. Ma, "Bubble formation and breakup dynamics in microfluidic devices: A review," *Chemical Engineering Science*, vol. 135, pp. 343–372, 2015.

[71] S. Varagnolo, M. Pierno, G. Mistura, and M. Sbragaglia, "Sliding droplets of xanthan solutions: a joint experimental and numerical study," *The European Physical Journal E*, vol. 38, p. 126, 2015.

[72] P. J. Whitcomb and C. W. Macosko, "Rheology of xanthan gum," *Journal of Rheology (1978-present)*, vol. 22, no. 5, pp. 493–505, 1978.

[73] G. P. Association *et al.*, *Physical properties of glycerine and its solutions*. Glycerine Producers' Association, 1963.

[74] S. Mirabedini, I. Dutil, and R. Farnood, "Preparation and characterization of ethyl cellulose-based core-shell microcapsules containing plant oils," *Colloids and Surfaces A: Physicochemical and Engineering Aspects*, vol. 394, pp. 74–84, 2012.

[75] Y. Doi, F. M. Gray, F. L. Buchholz, A. T. Graham, A. Striegel, W. W. Yau, J. J. Kirkland, D. D. Bly, M. J. Gordon Jr, and R. D. Archer, *Rheology: principles, measurements, and applications*. Wiley-VCH, 1994.

[76] S. Rafaï, D. Bonn, and A. Boudaoud, "Spreading of non-newtonian fluids on hydrophilic surfaces," *Journal of Fluid Mechanics*, vol. 513, pp. 77–85, 2004.

[77] A. Pommella, V. Preziosi, S. Caserta, J. M. Cooper, S. Guido, and M. Tassieri, "Using optical tweezers for the characterization of polyelectrolyte solutions with very low viscoelasticity," *Langmuir*, vol. 29, no. 29, pp. 9224–9230, 2013.

[78] M. D. Menech, P. Garstecki, F. Jousse, and H. A. Stone, "Transition from squeezing to dripping in a microfluidic t-shaped junction," *Jour. Fluid. Mech.*, vol. 595, p. 141, 2008.

[79] A. Gupta and M. Sbragaglia, "Effects of viscoelasticity on droplet dynamics and break-up in microfluidic t-junctions: a lattice boltzmann study," *The European Physical Journal E*, vol. 39, no. 6, pp. 1–16, 2016.

[80] A. Gupta and M. Sbragaglia, "A lattice boltzmann study of the effects of viscoelasticity on droplet formation in microfluidic cross-junctions," *The European Physical Journal E*, vol. 39, no. 2, pp. 1–15, 2016.

[81] A. Gupta, M. Sbragaglia, and A. Scagliarini, "Hybrid lattice boltzmann/finite difference simulations of viscoelastic multicomponent flows in confined geometries," *J. Compu. Phys.*, vol. 291, pp. 177–197, 2015.

[82] A. Gupta and M. Sbragaglia, "Deformation and breakup of viscoelastic droplets in confined shear flow," *Phys. Rev. E*, vol. 90, no. 2, p. 023305, 2014.

[83] A. Gupta, M. Sbragaglia, E. Foard, and F. Bonaccorso, "Viscoelastic multicomponent fluids in confined flow-focusing devices," *AIP Conference Proceedings*, vol. 1648, p. 850060, 2014.

[84] S. Gabbanelli, G. Drazer, and J. Koplik, "Lattice boltzmann method for non-newtonian (power-law) fluids," *Physical Review E*, vol. 72, p. 046312, 2005.

[85] R. Seemann, M. Brinkmann, T. Pfohl, and S. Herminghaus, "Droplet based microfluidics," *Rep. Prog. Phys.*, vol. 75, p. 016601, 2012.

[86] C. N. Baroud, F. Gallaire, and R. Dangla, "Dynamics of microfluidic droplets," *Lab on a Chip*, vol. 10, no. 16, pp. 2032–2045, 2010.

[87] H. Liu and Y. Zhang, "Droplet formation in a t-shaped microfluidic junction," *J. Appl. Phys.*, vol. 106, p. 034906, 2009.

[88] E. Chiarello, L. Derzsi, M. Pierno, G. Mistura, and E. Piccin, "Generation of oil droplets in a non-newtonian liquid using a microfluidic t-junction," *Micromachines*, vol. 6, no. 12, pp. 1825–1835, 2015.

[89] J. Xu, S. Li, J. Tan, Y. Wang, and G. Luo, "Preparation of highly monodisperse droplet in a t-junction microfluidic device," *AIChE journal*, vol. 52, no. 9, pp. 3005–3010, 2006.

[90] M. Zagnoni, J. Anderson, and J. M. Cooper, "Hysteresis in multiphase microfluidics at a t-junction," *Langmuir*, vol. 26, no. 12, pp. 9416–9422, 2010. PMID: 20465264.

[91] A. Gupta and R. Kumar, "Effect of geometry on droplet formation in the squeezing regime in a microfluidic t-junction," *Microfluid. Nanofluid.*, vol. 8, pp. 799–812, 2010.

[92] M. Sbragaglia, L. Biferale, G. Amati, S. Varagnolo, D. Ferraro, G. Mistura, and M. Pierno *Phys. Rev. E*, vol. 89, p. 012406, 2014.

[93] H. Kusumaatmaja, J. Leopoldes, A. Dupuis, and J. Yeomans *Europhys. Lett.*, vol. 73, p. 740, 2006.

[94] H. Liu and Y. Zhang, "Droplet formation in microfluidic cross-junctions," *Phys. Fluids*, vol. 23, no. 8, p. 082101, 2011.

[95] A. J. Wagner, "A practical introduction to the lattice boltzmann method," *Adt. notes for Statistical Mechanics*, vol. 463, p. 663, 2008.

[96] Y. B. Bao and J. Meskas, "Lattice boltzmann method for fluid simulations," *Department of Mathematics, Courant Institute of Mathematical Sciences, New York University*, 2011.

[97] M. R. Swift, W. R. Osborn, and J. M. Yeomans, "Lattice boltzmann simulation of nonideal fluids," *Phys. Rev. Lett.*, vol. 75, pp. 830–833, Jul 1995.

[98] M. R. Swift, E. Orlandini, W. R. Osborn, and J. M. Yeomans, "Lattice boltzmann simulations of liquid-gas and binary fluid systems," *Phys. Rev. E*, vol. 54, pp. 5041–5052, Nov 1996.

[99] X. Shan and H. Chen, "Lattice boltzmann model for simulating flows with multiple phases and components," *Physical Review E*, vol. 47, no. 3, p. 1815, 1993.